Dissertation

submitted to the

Combined Faculties of the Natural Sciences and Mathematics

of the Ruperto-Carola-University of Heidelberg. Germany

for the degree of

Doctor of Natural Sciences

Put forward by

Eva Lefa

born in Athens, Greece

Oral examination: 21th November 2012

Non-thermal Radiation processes in relativistic outflows from AGN

Referees: Prof. Dr. Felix A. Aharonian

Prof. Dr. Werner Hofmann

ABSTRACT

Non-thermal, leptonic radiation processes have been extensively studied for the interpretation of the observed radiation from jets of Active Galactic Nuclei (AGN). This work addresses the synchrotron and Inverse Compton scattering (ICS) mechanisms, and investigates the potential of a self-consistent, time-dependent approach to currently unsolved problems. Furthermore, it examines how deviations from standard, one-zone models can modify the radiated spectrum. A detailed analysis of the shape of the ICS spectrum is also performed.

In the first part a possible interpretation of the hard γ-ray blazar spectra in the framework of leptonic models is investigated. It is demonstrated that hard γ-ray spectra can be generated and maintained in the presence of energy losses, under the basic assumption of a narrow electron energy distribution (EED). Broader spectra can also be modeled if multiple zones contribute to the emission. In such a scheme, hard flaring events, like the one in Mkn 501 in 2009, can be successfully interpreted within a "leading blob" scenario, when one or few zones of emission become dominant.

In the second part the shape of the Compton spectrum close to the maximum cutoff is investigated. Analytical approximations for the spectral shape in the cutoff region are derived for various soft photon fields, providing a direct link between the parent EED and the upscattered spectrum. Additionally, a generalization of the beaming pattern for various processes is derived, which accounts for non-stationary, anisotropic and non-homogeneous EEDs. It is shown that anisotropic EEDs may lead to radiated spectra substantially different from the isotropic case. Finally, a self-consistent, non-homogeneous model describing the synchrotron emission from stratified jets is developed. It is found that transverse jet stratification leads to characteristic features in the emitted spectrum different to expectations in homogeneous models.

ZUSAMMENFASSUNG

Bezüglich der Herkunft der beobachteten Strahlung von Jets in Aktiven Galaktischen Kernen (AGN) wurden nicht-thermische, leptonische Strahlungsprozesse intensiv untersucht. In der vorliegenden Arbeit wird die Strahlungserzeugung durch Synchrotron-Emission und inverse Compton-Streuung (ICS) diskutiert und das Potential eines selbstkonsistenten, zeitabhängigen Models zur Erklärung aktuell noch ungelöster Probleme analysiert. Des Weiteren werden die Auswirkungen von Abweichungen von Standardmodellen auf das emittierte Spektrum untersucht. Die Form der ICS-Spektren wird im Detail diskutiert.

Im ersten Teil dieser Arbeit wird eine mögliche Erklärung der harten Gammastrahlen-Spektren von Blasaren im Rahmen eines leptonischen Models untersucht. Dabei wird gezeigt, dass sich harte Gammastrahlenspektren bei Annahme einer schmalen Elektronen-Energieverteilung (EED) auch angesichts von Energieverlusten erzeugen und erhalten lassen. Breitere Emissionsspektren können durch Überlagerung von Beiträgen verschiedener Zonen generiert werden. In diesem Zusammenhang können harte Emissionsereignisse, wie z.B. das in 2009 für Mkn 501 beobachtete, durch ein "leading-blob" Szenario, bei dem eine oder mehrere Zonen dominieren, erfolgreich erklärt werden.

Im zweiten Teil wird das Compton-Spektrum nahe der maximalen Energie der EED untersucht. Die in dieser Arbeit hergeleiteten, analytischen Näherungen für die Form des Compton-Spektrums erlauben eine direkte Verbindung des gestreuten Emissionsspektrums mit der erzeugenden EED für verschiedene (soft photon) Felder. Außerdem wird eine Verallgemeinerung des relativistischen "beaming patterns" für den Fall nicht-stationärer, anisotroper und inhomogener EEDs hergeleitet. Anisotrope EEDs können dabei zu Spektren führen, die sich erheblich vom isotropen Fall unterscheiden. Zuletzt wird, motiviert durch neuere Simulations- und Beobachtungsergebnisse, ein selbstkonsistentes (Synchrotron) Emissionsmodel entwickelt, bei dem der zugrundeliegende Jet eine transversale Abhängigkeit (parallele Scherströmung) aufweist. Dabei zeigt sich, dass eine transversale Abhängigkeit zu charakteristischen Eigenschaften des emittierten Spektrums führt, die sich signifikant von den Erwartungen homogener Modelle unterscheiden und damit Einblick in die Jetstruktur geben.

Contents

Chapter 1

Introduction

1.1 Basic properties and the physics of AGN

Relativistic jets are common in astrophysical environment. Active Galactic Nuclei (AGN), Gamma Ray Bursts (GRBs) and microquasars have been proven to exhibit highly collimated outflows in which particles are accelerated to relativistic energies and radiate. Among these sources, AGN are of particular interest. They provide an excellent environment for investigating several aspects of modern astrophysics; accretion, formation and collimation of jets, magnetohydrodynamics, particle acceleration theories and radiation mechanisms, all come into play. Additionally, AGN are directly related to the question of galaxy evolution. Since the discovery of Quasars (Schmidt 1963), these object have been the most prominent emitters among the most luminous and distant objects in the universe and have rightfully attracted particular astrophysical interest.

1.1.1 The general picture of AGN

In general, AGN are galaxies with energetic phenomena in their nuclei (central region) which can not be directly attributed to stellar processes. AGN produce very high luminosities, of the order of $10^{46} - 10^{48} erg/sec$, (four orders of magnitude higher than the luminosity of a typical galaxy) in a centered, compact volume (within parsec scales). Their continuum spectra is attributed to radiation from non-thermal processes and can emerge over a wide range of the electromagnetic spectrum, from very low radio frequencies up to TeV γ-rays. Strong variability (increase in luminosity by a factor of ~ 2 or more) is present on various timescales, from years down to less than a day, even on minute-timescales (Aharonian et al. 2007). The Spectral Energy Distribution (SED) of these objects often exhibit emission (and occasionally absorption) lines indicating excitation by the continuum emission. Roughly speaking, a galaxy can be defined as AGN if it exhibits some of the aforementioned characteristic features (not necessarily all of them at the same time) and around $1 - 3\%$ of the whole galaxy population can be accounted as AGN.

Nowadays, the generally accepted picture for the fueling and the observed properties of AGN is based on the existence of a rotating, supermassive black hole at the center of the galaxy. The supermassive black hole (SMBH) is surrounded by a thin disk which accretes gas with angular momentum onto the SMBH (Salpeter, 1964; Zeldovich & Novikov, 1964). The release of the gravitational energy of the infalling matter is ultimately responsible for the large radiative output of those objects. Accretion onto a compact object is thus regarded to be the principal source of energy for AGN.

In the simplified picture of stationary, spherical accretion there exists an upper limit for the luminosity of a source of mass M. This is achieved when the (outward) radiation pressure (due to Thomson scattering) on a proton-electron pair is balanced by the (inward) gravitational force and is called Eddington luminosity

$$L_{edd} = \frac{4\pi G M m_p c}{\sigma_T} \approx 1.2 \times 10^{46} \left(\frac{M}{10^8 M_\odot} \right) erg/sec. \tag{1.1}$$

Here σ_T denotes the Thomson cross section, m_p the proton mass, G the gravitational constant and c the speed of light. Obviously accretion is not spherical in the case of AGN, however the above formula represents a usefull characteristic limit for the produced luminosity. The minimum mass of a central object that emits at the Eddington limit is then

$$M = 8 \times 10^5 \frac{L_{edd}}{10^{44} erg\ sec^{-1}} M_\odot. \tag{1.2}$$

For AGN luminosities of $10^{46} - 10^{48} erg/sec$, a central mass of the order of $10^8 - 10^{10} M_\odot$ is required. On the other hand the rapid variability occasionally observed on extremely small timescales suggests that the tremendous luminosity observed originates in a very compact volume. This is due to causality arguments that restrict the size of the emitting region. If Δt is the variability timescale, then the source can not extend to larger scales than the light crossing time, i.e. the radius of the source must obey $R < c\Delta t$[1]. The relatively small sizes that the short variability implies in combination with the large masses imposed by the Eddington limit suggest that a SMBH is the best candidate for the central engine of AGN. Apart from this argument, there is increasing evidence that favors the existence of SMBHs at the nucleus of these galaxies (see e.g. Madejski 1999).

Our current picture of accretion disks is based largely on the work of Shakura & Sunyaev (1973) (see e.g. King 2012 for a very brief review). In this classical approach, the accretion disk is thin, steady, panchromatic (it has different temperatures at different radius R) and radiates locally as a black body. The effective temperature profile scales as $T(R) \propto R^{-3/4}$. In some AGN the overall continuum (stretched-out black body-like) spectrum can account for the observed UV/optival emission, the so called "big blue bump". The in-detail description of the flow of the accreting matter has been however a major part of astrophysical studies (see e.g. the textbook of Frank et al. (1995) and references therein).

The accretion onto a black hole is often associated with the launching of a jet of plasma that produces the observed radiation. The formation and collimation of

---

[1] Note that for a relativistically moving source, as is often the case, Doppler boosting has to be taken into account, see paragraph 1.1.6

jets has been intensively studied in the hydrodynamical (HD) and magnetohydrodynamical (MHD) formulation by applying both analytical and numerical techniques. One can distinguish three main types of models (see e.g. Celotti & Blandford, 2001; Sauty et al., 2002 for reviews).

(a) ***Hydrodynamical acceleration:*** An adiabatic flow that propagates in the external medium of decreasing pressure can get accelerated and collimated as in a de Laval nozzle, as proposed in the so called "twin-exhaust" model of Blandford & Rees (1974). The "weak point" of such a model is that the required gas pressure needed from the external medium implies a large X-ray flux which is not observed.

(b) ***Radiative acceleration:*** Acceleration by radiation pressure could in principle explain the relativistic jets observed in AGN. This mechanisms is based on radiation beams that are produced and collimated in funnels (vortices) along the rotational axis of the accretion disk (see e.g. Lynden-Bell, 1978; Piran, 1982). However, intense radiation fields are required and even if they exist Compton drag limits severely the velocity of the flow.

(c) ***Magnetohydrodynamical acceleration:*** Perhaps the most promising mechanism for the production of jets involve magnetic fields. Extraction of energy may occur from the accretion disk as an MHD wind is launched due to centrifugal force if the angle between the poloidal component of the magnetic field and and the disk surface is 60^o. Alternatively, the relativistic jet can be powered by the rotating black hole itself (Ruffini & Wilson, 1975; Lovelace, 1976; Blandford & Znajek, 1977).

Independent of the formation mechanism, relativistic jets do occur in AGN and can range from sub-parsec scales out to Mpc scales. Perhaps, the most direct evidence for high speeds is superluminal motion. VLBI (Very Long Baseline Interferometry) observations of some sources have detected radio components that show transverse (apparent) velocities that exceed the speed of light even up to $\sim 40c$. This discrepancy with special relatively can be solved only if the outflow moves at relativistic speeds close to the line of sight (Rees 1966). The transverse apparent velocity β_{app} with respect to the "real" velocity β is

$$\beta_{app} = \frac{\beta \sin\theta}{1 - \beta\cos\theta}. \tag{1.3}$$

Thus for relativistically moving sources, $\beta > 1/\sqrt{2} \sim 0.7$, there exist some values of the orientation angle θ at which superluminal motion is observed. The maximum apparent velocity occurs at $\sin\theta = 1/\Gamma$, where $\Gamma = (1-\beta^2)^{-1/2}$ is the Lorentz factor, and takes the value $\beta_{app}^{max} = \sqrt{(\Gamma^2 - 1)}$. This means that if an apparent velocity of e.g. $\beta_{app} = 5$ is detected, then the source has to move relativistically as it can not have Lorentz factor less than $\Gamma_{min} = \sqrt{\beta_{app}^2 + 1}$, providing strong evidence for the existence of relativistic jets.

The observed, non-thermal, continuum spectrum is commonly attributed to the radiation of particles that accelerate to highly relativistic energies in the jets. Apart from the continuum, broad emission lines are often detected. These are considered to originate from rapidly moving clouds of gas above the accretion disk that may extend up to $10^3 R_g$, where R_g the Schwarzschild radius. The area where these clouds are located is commonly abbreviated as Broad Line Region (BLR). Above the BLR there are slower-moving clouds that can extend as far as $10^{20} cm$ and are responsible for the narrow lines that may exist in the SED of some AGN. The main picture of AGN is completed with the existence of a dusty torus around the central object that obscures the radiation from the inner parts if the line of sight passes through this torus.

In summary, the commonly accepted picture for AGN (on a very first approach) has been formulated as following:

- A supermassive, rotating black hole in the center of the galaxy of mass $10^8 - 10^{10} M_\odot$;
- A thin disk accreting onto the SMBH, from about 2 to beyond 100 gravitational radii that emits mainly at UV and soft X-rays (though it is sometimes responsible for the hard X-rays as well);
- The BLR which extends up to $\sim 10^3 R_g$ and scatters away the radiation from the inner parts;
- The NLR which extends from 10^4-$10^6 R_g$;
- A dusty torus (with an inner radius of $\sim 10^3 R_g$) which obscures the central parts of the AGN emission.

1.1.2 Unification schemes and classification of AGN

The numerous sources identified as AGN exhibit different observational characteristics and their classification according to phenomenological properties is rather complex. In a very simplified picture, AGN can be divided to sub-classes by two main parameters; the radio-loudness and the width of the emission lines (see e.g. Padovani 1999). Approximately 10% of the AGN population is radio-loud, i.e. their radio luminosity exceed the optical luminosity by a factor of ten, $L_{rad}/L_{opt} \sim 10$. According to the width of their emission lines, AGN can be further divided into type I (broad line emission galaxies; they exhibit lines that correspond to velocities of the clouds of the order of $2,000 - 10,000 km/sec$) and type II (narrow line emission galaxies with corresponding velocities of $\sim 500 km/sec$). For example, Seyfert I and Seyfert II/radio-quiet Quasars (QSOs) are radio-quiet AGN of type II and I respectively. Radio-loud type II AGN are called narrow-line radio galaxies (NLRG). Radio-loud type I AGN are referred as broad-line radio galaxies (BLRGs). According to their radio morphology radiogalaxies of both types are also classified as Fanaroff-Riley (FR) I and II . Some objects have very weak emission lines, like the so called BL Lacs which are radio-loud.

Although AGN appear different, unification schemes support the idea that they are not truly different objects. On the contrary, they share the same intrinsic properties but they are viewed under different angles (see the reviews of Antonucci, 1993; Urry & Padovani, 1995). The observed radiation might e.g. be strongly enhanced due to Doppler boosting if the jet is pointing towards the observer or it can be obscured by the torus if the viewing angle is large (see fig. 1.1) so that only the NLR can be seen. For example, Seyfert I galaxies have been "unified" with Seyfert II galaxies with the former be seen edge-on (large viewing angles) and the latter face-on (small viewing angles). In a similar way low-luminosity FR I sources and high luminosity FR II radio galaxies correspond to BL Lacs and radio Quasars respectively.

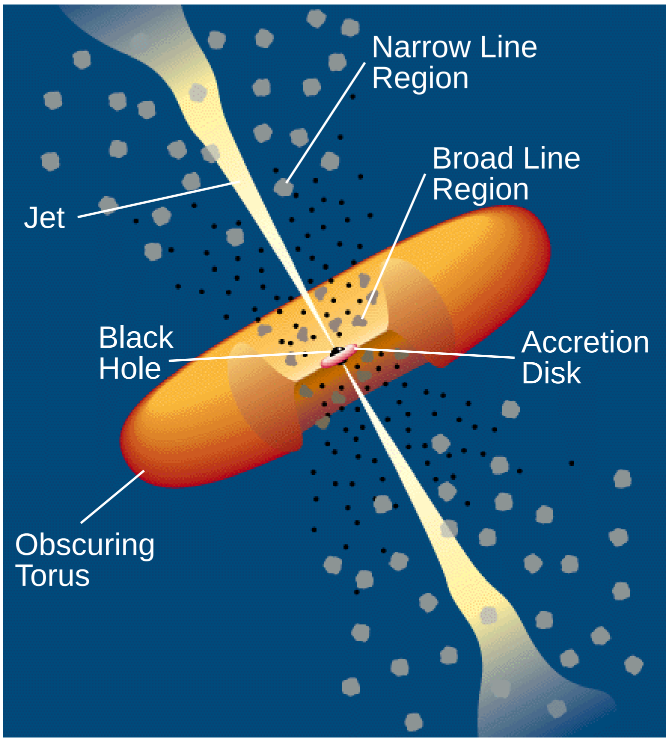

Figure 1.1: Sketch illustrating the unified picture of AGN (not to scale). Figure from Urry & Padovani (1995)

1.1.3 Blazars: properties and observed spectrum

A sub-class of AGN of particular interest are the so called Blazars. Blazars are radio sources that apparently exhibit the most extreme characteristics; rapid variability (at all wavelengths and on all timescales), high polarization (both in optical and radio frequencies) and in some cases a lack of any strong emission lines. Blazars are characterized by broadband (from radio to VHE γ-rays), non-thermal emission produced in relativistic jets pointing close to the line of sight to the observer and thus their observed radiation is strongly boosted. This group of AGN includes the Optically Violent Variable Quasars (OVVs) which are characterized by rapid variability, highly polarized Quasars (HPQs) that exhibit high percentage of linear polarization, the aforementioned BL Lacs and the Flat Spectrum Radio Quasars (FSRQs) that tend to have flat radio spectra, i.e. $F_\nu \propto \nu^{-\alpha}$ with $\alpha > -0.5$. The name "Blazars" originates from the astronomer Ed Spiegel, likely as an attempt to combine the names of BL Lacs and Quasars.

Blazars rightfully hold a special place among all AGN. Their broad band emission covers almost 20 orders of magnitude along the electromagnetic spectrum, and thus they are ideal sources for multiwavelength studies. They are very often strong γ-ray emitters (up to TeV energies), implying that very energetic phenomena take place. The relativistic beaming of the radiation amplifies the brightness of these sources so that they are prominent for detection even at low luminosities, or equivalently at large distances. Due to this strong enhancement, the spectrum of Blazars is highly dominated by the jet emission. The "noise" that originates from other parts of the galaxy (accretion disk, BLR, torus etc..) is likely suppressed. For this reason Blazars serve to define the properties of the jet and to study the associated physics that takes place in relativistic outflows.

The continuum Spectral Energy Distribution (SED) of Blazars extends from the low frequency radio band up to TeV γ-rays. It is dominated by non-thermal emission and often shows two distinct components. A low-energy component from radio up to UV and X-rays and a high energy component from X-rays to γ-rays (see e.g. the SED of the Blazar Mkn 421 in fig. 1.2). Variability characterizes all emission wavelengths and particularly at high energies very short timescales (down to minutes) have been reported (e.g. Aharonian et al., 2007; Albert et al., 2007). Due to Lorentz transformations the observed variability timescales Δt_{obs} are connected to the intrinsic (comoving) timescale Δt_{int} as

$$\Delta t_{obs} = \Delta t_{int}(1+z)/D \tag{1.4}$$

where D is the Doppler factor and z the cosmological redshift. Causality arguments then limit the source size to

$$R \lesssim c\Delta t_{obs} D/(1+z), \tag{1.5}$$

implying that the emission originates in a very compact region.

Theoretical radiation models that attempt to interpret the observed Blazar spectra can be divided into two main categories, hadronic and leptonic models (see e.g. a recent review from Boettcher 2012). Hadronic models propose that the main carriers of dissipated energy in the jet are energetic protons, whereas in leptonic models the energy available for radiation is in electrons or $e^{\pm}$ pairs.

Hadronic models: Energetic photons can emit γ-rays via pp interaction with surrounding gas or via pγ interaction with a photon field. π^0-decay γ-rays can be produced in *pp* interactions, but very high densities of thermal plasma are required to explain the observed high luminosities (see e.g. Morrison et al. 1984). Alternatively, if protons are affectively accelerated to the threshold for $p\gamma$ pion production, then synchrotron supported cascades will initiate (Mannheim, 1993; Mannheim & Biermann, 1992), i.e. protons will interact with the synchrotron photons produced by electrons that are co-accelerated with the protons (external photon fields may also be a possibility, e.g. thermal photons from the disk, Protheroe 1997). Electromagnetic cascades can be initiated by π^0-decay, electrons from the $\pi^{\pm} \rightarrow \mu^{\pm} \rightarrow e^{\pm}$ decay, p-synchrotron photons and μ, π and K synchrotron photons. Proton acceleration to such high energies requires large magnetic fields (of the order of tens of

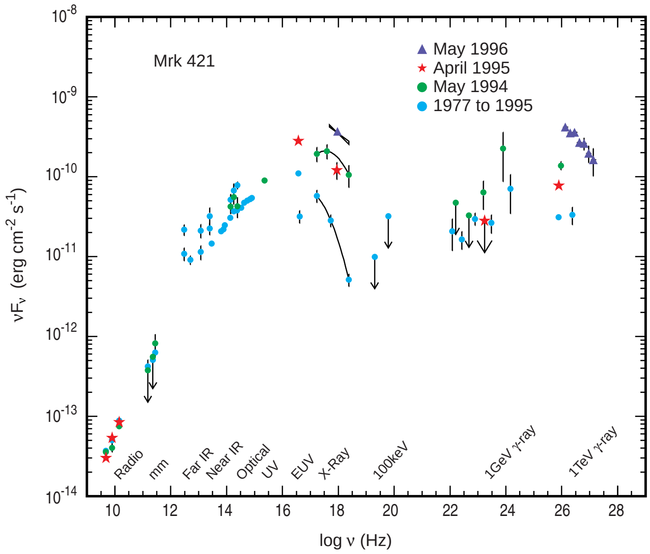

Figure 1.2: SED of the Blazar Mkn 421 (Credit: J.H. Buckley, Washington U.)

Gauss) and in such an environment primary proton synchrotron radiation also offers an effective channel for production of high energy γ-rays (Aharonian 2000).

Leptonic models: In leptonic models electrons (or/and positrons) are the main emitters. Once electrons are accelerated to relativistic energies, they interact with the magnetic field and produce synchrotron radiation, which commonly accounts for the low energy component of the Blazar spectra. The strength of the magnetic field required is sufficiently smaller (of the order of $\sim 1G$) than in the case of hadronic models. The high energy component of the spectrum is attributed to Inverse Compton Scattering (ICS) due to upscattering of low energy photons by the same electron population, as originally discussed in Jones et al. (1974). Depending on the nature of the target photon field, the leptonic models can be referred to as synchrotron self-Compton (SSC) or external Compton (EC) models. In the SSC model, the synchrotron photons serve as the target photon field. Their up-scattering by the same electron population produces the high energy γ-ray radiation (e.g., Maraschi et al., 1992; Bloom & Marcher, 1996). In EC models the target photons come from a zone external to the jet. In Blazars the main sources for external photon are

- UV/soft X-ray radiation from the accretion disk either reaching the jet directly (Dermer et al., 1992; Dermer & Schlickeiser, 1993) or after re-processing in the BLR (Sikora et al. 1994) or other material (e.g. Blandford & Levinson 1995)

- IR radiation from the dusty torus (Sikora et al. 1997).

Which of these mechanisms is responsible for the high energy emission of Blazars (or if both contribute to the observed spectrum) is still unclear. Throughout this thesis, the issues examined are associated to (or approached within) leptonic processes.

The main radiation mechanisms involved (synchrotron and ICS) are presented in the next paragraph, and they are embedded in a self-consistent approach.

Perhaps the two most triggering features in Blazar physics that have attracted special attention are the variability detected at very short timescales and the origin of very hard, intrinsic γ-ray source spectra after correcting for the absorption due to the Extragalactic Background Light (EBL). Although the observed TeV spectra of these sources are steep, their de-absorbed (EBL-corrected) spectra appear intrinsically hard (see section 1.4). In chapter 2 we deal with this problem, proving a self-consistent solution with leptonic models. Furthermore, in chapter 3 we examine the possibility to account for hard spectra in a flaring state that normally (in a low state) are softer.

1.2 Radiation processes in leptonic models

Radiation mechanisms hold an outstanding place in astrophysics, as they are our "eyes" to the astrophysical objects of the universe. Emission processes are the first step to explore the physical mechanisms that take place in a variety of sources and thus, a deep understanding and in-detail investigation is unavoidably necessary. In this thesis we focus on leptonic models and the main processes involved are synchrotron radiation and ICS. These radiation mechanisms have been intensively studied and remain two of the basic emission mechanisms that account for observations not only in Blazars and AGN in general, but also for a series of astrophysical objects, e.g. pulsars, microquasars, GRBs etc.

1.2.1 Synchrotron radiation

Classically, a charged particle which moves on a curved path or is accelerated on a straight-line path will emit electromagnetic radiation. When the reason of acceleration is a magnetic field then the radiation is called synchrotron radiation (for relativistic particle velocities). Synchrotron radiation was first suggested by Alfvén & Herlofson (1950) to be the radiation mechanism responsible for the newly (back then) discovered cosmic radio sources (such as supernova remnants and AGN). Since then it has been investigated extensively in several textbooks and in the context of astrophysical applications (Jackson, 1975; Rybicki & Lightmann, 1979; Longair, 2010).

In the presence of a (uniform) magnetic field of strength B, a charged particle will gyrate around the field lines at helical trajectory. From the equations of motion we can find the frequency of rotation

$$\omega_B = \frac{qB}{\gamma mc}. \tag{1.6}$$

If we denote by α the pitch angle (the angle between the field and the particle velocity) then in the limit of relativistic velocities ($u \approx c$) the total emitted power is

$$-\left(\frac{dE}{dt}\right) = 2\sigma_T c U_B \gamma^2 \sin\alpha^2, \tag{1.7}$$

where $U_B = B^2/8\pi$ is the magnetic field energy density and σ_T the Thomson cross section. For an isotropic particle distribution, averaging over pitch angles leads to the formula

$$-\left(\frac{dE}{dt}\right) = \frac{4}{3}\sigma_T c U_B \gamma^2. \tag{1.8}$$

The derivation of the synchrotron spectrum from the Lienard-Wiechert potentials is well established and can be found in the aforementioned textbooks. Some main points are the following: Due to light abberation effects the radiation of a relativistic particle (in the frame of the observer) is beamed within a cone of opening angle $\sim 1/\gamma$. A distant observer will thus receive pulses of radiation and the spectrum is the Fourier transform of these pulses once time delay effects are taken into account. The duration of the pulse is $\Delta t \approx (\gamma^3 \omega_B \sin\alpha)^{-1}$ and thus the spectrum extends roughly up to the critical frequency

$$\omega_c = \frac{3\gamma^2 qB\sin\alpha}{2mc}. \tag{1.9}$$

The full expression for the emitted spectrum for monoenergetic electrons of energy E_e is

$$\frac{d\dot{N}_\gamma}{d\epsilon_\gamma} = \frac{\sqrt{3}q^3 B\sin\alpha}{mc^2 h\epsilon_\gamma} F\left(\frac{\epsilon_\gamma}{E_c}\right), \tag{1.10}$$

where

$$E_c = \hbar\omega_c = \frac{3qBh\sin\alpha}{4\pi mc}\frac{E_e^2}{(mc^2)^2}, \tag{1.11}$$

and the function $F(x)$ is given in terms of the modified Bessel function $K_{5/3}(\xi)$

$$F(x) \equiv x\int_x^\infty K_{5/3}(\xi)d\xi. \tag{1.12}$$

The synchrotron spectrum peaks at $\sim 0.29E_c$. The function $F(x)$ for small and large values of x has the asymptotic form

$$F(x) \sim \begin{cases} \frac{4\pi}{\sqrt{3}\Gamma(1/3)}\left(\frac{x}{2}\right)^{1/3}, & x \ll 1 \\ \\ \left(\frac{\pi}{2}\right)^{1/2} x^{1/2}e^{-x}, & x \gg 1 \end{cases} \tag{1.13}$$

where $\Gamma(x)$ the Gamma function. Already from the above formula we expect the synchrotron spectrum at low energies to exhibit a dependance on energy as $\epsilon_\gamma^{1/3}$ and at high energies to have a (simple) exponential cutoff. For randomly oriented magnetic fields, one needs to integrate over the pitch angles, i.e. define the function

$$G(x) = \int \sin\alpha F(x) d\Omega/4\pi = \frac{1}{2}\int_0^\pi F(x)\sin^2\alpha d\alpha = x\int_x^\infty K_{5/3}(\xi)\sqrt{1-\frac{x^2}{\xi^2}}d\xi. \tag{1.14}$$

The function $G(x)$ can be expressed analytically in terms of modified Bessel functions (or alternatively in terms of Whittaker's functions, Crusius & Schlickeiser

1986), but there are also approximation formulas in terms of simple polynomials (see e.g. Melrose, 1980; Zirakashvili & Aharonian, 2007). Throughout this thesis, we have used the approximations derived in Aharonian et al. (2010), which provide an accuracy better than 0.2% over the entire range of variable x

$$G(x) = \frac{1.808x^{1/3}}{\sqrt{1+3.4x^{2/3}}} \frac{1+2.21x^{2/3}+0.347x^{4/3}}{1+1.353x^{2/3}+0.217x^{4/3}} \, e^{-x}. \tag{1.15}$$

These functions correspond to relativistic and monoenergetic electrons interacting with tangled magnetic fields. There are, however, some interesting deviations from these standard formulas. For example, an exception may occur if the magnetic field in the source would be fully turbulent with zero mean component. In such a case, the low-frequency part of the synchrotron spectrum could be harder than $F_{\epsilon_\gamma} \propto \epsilon_\gamma^{1/3}$ (Medvedev, 2006; Derishev et al., 2007; Reville & Kirk, 2010). Furthermore, if the pitch angles of the particles are very small (less than $1/\gamma$) then the emission differs qualitatively from the usual synchrotron emission in the sense that it peaks at lower energies and it falls off linearly at small frequencies, ϵ_γ (Epstein, 1973; Epstein & Petrosian, 1973).

In astrophysical problems we often encounter power-law electron distributions (see also paragraph 1.2.2) of the form

$$dN_e/dE_e \propto E_e^{-p}\Theta\left(E_e - E_{min}\right)\Theta\left(E_{max} - E_e\right), \tag{1.16}$$

between a minimum and maximum energy, E_{min} and E_{max}, respectively. Here $\Theta(x - x_0)$ is the step function. The synchrotron radiation spectrum is then a power-law, the index of which is related to the electron distribution index,

$$\epsilon_\gamma d\dot{N}_\gamma/d\epsilon_\gamma \propto \epsilon_\gamma^{-\frac{p-1}{2}} \tag{1.17}$$

and it spreads roughly from $E_\gamma^{min} \propto BE_{min}^2$ to $E_\gamma^{max} \propto BE_{max}^2$, where B is the magnetic field. Below the low energy cutoff E_γ^{min} the functional dependance of the spectrum on the radiated photon energy is the same as the synchrotron kernel function, i.e. $\epsilon_\gamma d\dot{N}_\gamma/d\epsilon_\gamma \propto \epsilon_\gamma^{1/3}$. This feature is discussed in chapter 2 where we investigate the assumption of a large value for the minimum cutoff of the electron distribution for the interpretation of the hard spectrum sources, i.e. we examine how both synchrotron and ICS appear in this case. In chapter 4 we also refer to the shape of the synchrotron spectrum close to the maximum cutoff not only in the case of a sharp, abrupt cutoff for the electron distribution, but under the more general assumption of an exponential cutoff shape.

1.2.2 Inverse Compton Scattering

The interaction of relativistic electrons with low energy radiation through Inverse Compton Scattering (ICS) provides one of the principal γ-ray production processes in astrophysics. In a variety of astrophysical environments, from very compact objects like pulsars and Active Galactic Nuclei (AGN) to extended sources like supernova remnants and clusters of galaxies, low energy photons are effectively boosted to high energies through this mechanism.

In the ICS process low energy photons of energy ϵ_γ are up-scattered by relativistic electrons to higher energies E_γ. The basic features of the ICS have been analyzed by Jones (1968), Blumenthal & Gould (1970). An extensive analysis can be found in the aforementioned textbooks (Jackson, 1975; Rybicki & Lightmann, 1979; Longair, 2010). The total cross section of ICS is derived in quantum electrodynamics. In the case of isotropic photons and electrons it can be shown that the spectrum of high energy photons generated per unit time due to ICS from monoenergetic electrons is (see e.g. Blumenthal & Gould (1970))

$$d\dot{N}_\gamma/dE_\gamma = \int_0^\infty W(E_e, \epsilon_\gamma, E_\gamma) n_{ph}(\epsilon_\gamma) d\epsilon_\gamma, \tag{1.18}$$

where

$$E_{e\,\min} = \frac{1}{2} E_\gamma \left(1 + \sqrt{1 + \frac{m^2c^4}{\epsilon_\gamma E_\gamma}}\right), \tag{1.19}$$

$$W(E_e, \epsilon_\gamma, E_\gamma) = \frac{8\pi r_e^2 c}{E_e\,\eta} \left[2q\,\ln q + (1-q)\left(1 + 2q + \frac{\eta^2 q^2}{2\,(1+\eta q)}\right)\right], \tag{1.20}$$

and

$$\eta = \frac{4\,\epsilon_\gamma E_e}{m^2c^4}, \quad q = \frac{E_\gamma}{\eta\,(E_e - E_\gamma)}\ . \tag{1.21}$$

Here the function $W(E_e, \epsilon_\gamma, E_\gamma)$ in eq. (1.20) describes the total scattering probability. E_e comes from kinematic effects; it is the minimum energy that an electron can have when it upscatters a soft photon of ϵ_γ to energy E_γ.

Two domains of scattering exist, depending on the energy of the ingoing photons in the rest frame of the electrons. In the classical Thomson regime (coherent or elastic scattering) the photons in the electron rest frame have energy much smaller than the electron rest mass energy, $\eta \ll 1$. The cross section in that case is approximately constant, $\sigma \approx \sigma_T$ and the maximum energy of the upscattered photons is

$$E_\gamma^{max} = 4\gamma^2\epsilon_\gamma, \tag{1.22}$$

while their average energy is

$$\langle E_\gamma \rangle = \frac{4}{3}\gamma^2\epsilon_\gamma. \tag{1.23}$$

In the opposite case, ($\eta \gg 1$, incoherent scattering), quantum effects become important and electrons lose a substantial part of their energy in each scattering. The maximum outgoing photon energy is then

$$E_\gamma^{max} = \gamma mc^2 \tag{1.24}$$

as it obviously can not exceed the electron energy. Klein-Nishina effects lead to a suppress of the cross section and this in turn has interesting effects on the electron distribution and the emitted spectrum, as discussed in section 1.3.

The ICS spectrum of relativistic electrons has been intensively studied in the literature. We know e.g. that the upscattering of soft photons by power-law electron distributions produces power-law Compton spectra. The power-law index is different in the Thomson and Klein-Nishina regimes. In the classical regime, it resembles the synchrotron spectrum, i.e.

$$E_\gamma d\dot{N}_\gamma/dE_\gamma \propto E_\gamma^{-\frac{p-1}{2}}, \tag{1.25}$$

whereas in the Klein-Nishina limit it is steeper,

$$E_\gamma d\dot{N}_\gamma/dE_\gamma \propto E_\gamma^{-p}, \tag{1.26}$$

(see e.g. Blumenthal & Gould, 1970; Aharonian & Atoyan, 1981c). In chapter 2 we examine the form of the spectrum below the low energy cutoff. This question is related to how hard the ICS spectrum can be in either SSC or EC models. In chapter 4 we examine a major issue of the radiated Compton spectrum that has not been addressed in the literature, although the properties of the ICS spectrum have been extensively investigated. We derive analytical approximations for the shape of the high energy cutoff (for various target photons fields), which provide as with information for the acceleration processes that take place in the astrophysical source.

1.3 A self-consistent approach: kinetic equation of electrons

We have discussed the spectrum that arises from a power-law electron distribution, an assumption very often made in astrophysical application. However, for a self-consistent approach, one needs to take into account the acceleration of particles as well as the energy losses or/and the possible escape from the radiation source.

In a microscopical description the distribution function $f(\mathbf{x}, \mathbf{p}, t)$ is defined by the requirement that the number of particles in the volume element d^3xd^3p of phase space is given by

$$dN = f(\mathbf{x}, \mathbf{p}, t)d^3xd^3p, \tag{1.27}$$

where $\mathbf{x}$ the is space vector and $\mathbf{p}$ the momentum vector. The phase space volume element as well as the distribution function are invariant under Lorentz transformation and thus, as naturally expected, the number of particles is also invariant. The evolution of the distribution function is described by the Boltzmann equation

$$\frac{\partial f}{\partial t} + \dot{\mathbf{x}}\frac{\partial f}{\partial \mathbf{x}} + \dot{\mathbf{p}}\frac{\partial f}{\partial \mathbf{p}} = \left[\frac{\partial f}{\partial t}\right]_c . \tag{1.28}$$

The collision term on the right-hand side may account for various processes, such as particle injection, acceleration, scattering, energy losses etc. If this term is zero then the above equation is also referred to as Liouville equation. The reason is that the left hand side represents the derivative of f along a trajectory and thus eq. 1.28 follows from the Liouville theorem which states that the distribution function is constant along trajectories.

In some astrophysical applications we often treat only injection/cooling problems. In that case the above equation 1.28 can be significantly simplified under the continue loss approximation (also referred to as kinetic equation) according to which

$$\frac{\partial F}{\partial t} + \frac{\partial(\dot{E}_e F)}{E_e} = Q(E_e, t). \tag{1.29}$$

Here, the function F is defined as $F = dN_e/dE_e$, under the assumption of isotropic and spatially homogeneous distribution functions. In that case $F = p^2 f dp d^3 x$ ($E_e = p$ for relativistic particles after setting $c = 1$). $Q(E_e, t)$ is the source of particles and $\dot{E}_e$ represents the energy losses. Energy losses can be radiative (synchrotron, Compton, bremsstrahlung, due to pp or $p\gamma$ interactions etc.) or non-radiative (e.g. adiabatic losses). However, in this scheme particles are assumed to lose energy in small fractions, which is not true e.g. for ICS losses in the Klein-Nishina regime. The second assumption made here is that acceleration and energy losses of the particles are treated independently. The acceleration (for some cases) can be represented phenomenologically by the injection term, implying that particles are accelerated in a different zone.

Fermi type acceleration

Particle acceleration can occur e.g. due to turbulence or plasma waves and in this case it is commonly referred to as Stochastic Acceleration. Fermi 1949 first proposed stochastic acceleration as a model for the production of cosmic rays (see e.g. Petrosian 2012 for a recent review). Charged particles of velocity $v \sim c$ scatter randomly at moving magnetized clouds of velocity u and they gain energy at a rate $\propto (u/c)^2$ mainly because the (energy gaining) head on collisions are more frequent than the (energy losing) follow-up collisions. Because the energy gain is second order in (u/c), this acceleration mechanism is also called 2nd order Fermi acceleration. The scattering centers can be plasma waves or MHD turbulence (e.g. Sturrock 1966). Later, Fermi (1954) suggested that particles can be accelerated by scattering back and forth between the edges of a "magnetic bottle". This is the case of acceleration at a shock front (Krymskii, 1977; Axford et al., 1978; Bell, 1978; Blandford & Ostriker, 1978). Energetic particles pass the shock and scatter off magnetic field irregularities (Alfven waves) in analogy to the magnetic bottle. This process is called Diffusive Shock Acceleration (DSA) and because the gain in energy is proportional to v_s/c, where v_s the shock velocity, is also known as 1st order Fermi acceleration[2].

DSA normally produces power-law particle distributions, with a power-law index of $p \sim 2$ for strong shocks with compression ratio $\rho = 4$. Thus, a common assumption is that the injection term has the form

$$Q(E_e, t) \propto E_e^{-p} \Theta(E_e - E_{min}) \Theta(E_{max} - E_e), \tag{1.30}$$

---

[2] There are of course other types of particle acceleration mechanisms used in astrophysical applications, such as acceleration in an electric field (e.g. Bednarek et al. 1996) or due to magnetic reconnection (e.g. Lazarian et al. 2012). The Fermi-type acceleration processes are however among the most popular and prominent theories.

where E_{min} and E_{max} the minimum and maximum particle energy. If one additionally assumes escape from the radiation zone at an "escape time" τ, then eq. 1.29 becomes

$$\frac{\partial F}{\partial t} + \frac{\partial(\dot{E}_e F)}{E} + \frac{F}{\tau} = Q(E_e, t). \tag{1.31}$$

The Green's function solution to this equation in the case of time-independent energy losses and constant escape time was found by Syrovatskii (1959). Full analytical solutions can be found for several types of injection and energy losses (Kardashev 1962). For example, for synchrotron type losses and constant power-law injection, the resulting particle distribution has again a power-law form. In the fast cooling regime (cooling timescale t_{cool} smaller than escape timescale τ) this is a power-law distribution steeper by a factor of 1,

$$F(E_e) = \frac{1}{\dot{E}_e} \int_{E_e}^{\infty} dE'_e Q(E_e) \propto E_e^{-p-1}. \tag{1.32}$$

In the slow cooling regime ($t_{cool} \gg \tau$), the power-law index remains the same

$$F(E_e) = \tau Q(E_e) \propto E_e^{-p}. \tag{1.33}$$

On the other hand, if Compton losses in the Klein-Nishina regime dominate, then the particle distribution will be harder due to the nature of the Klein-Nishina losses, as was first realized by Blumenthal (1971). This effect is evident in the synchrotron part of the spectrum which is as well harder, but not in the high energy Klein-Nishina component because there, the suppression of the cross section compensates the hardening of the particle distribution. Its importance in astrophysics has been discussed in the context of different non thermal phenomena, in particular by Aharonian & Ambartsumyan (1985), Zdziarski et al. (1989), Dermer & Atoyan (2002), Moderski et al. (2005), Khangulyan & Aharonian (2005), Kusunose & Takahara (2005), Stawarz et al. (2006) and Stawarz et al. (2010).

Atoyan & Aharonian (1999) have derived a generalized solution of eq. 1.31 in which both energy losses and escape can depend on time. These are interesting cases that are actually expected to take place in astrophysical environments. A time-dependent escape of the particles from the source of radiation is a natural consideration, whereas the case of time-dependent energy losses allows to examine some promising models, e.g. the evolution of particles in an expanding source. In chapter 2 we develop a full solution based on Atoyan & Aharonian (1999) for the case of adiabatic losses along the total energy range (and below the low-energy cutoff of the electron distribution). This approach offers a reasonable interpretation to the hard spectra. A solution of the particle' s kinetic equation is used also in chapter 6, where we demonstrate that in a (stratified) jet a self-consistent approach is equivalent with solving the kinetic equation in which, the time variable is replaced by the spatial coordinate along the motion of the flow. In that case, we show that some special features may appear in the synchrotron spectrum, which are related to the cooling break of the electrons, i.e. the energy at which we pass from the slow cooling to the fast cooling regime.

Power-law distributions are predicted as well in the stochastic acceleration scenario (with different power-law index) and also in acceleration at a gradual velocity shear (see e.g. Rieger et al. 2007). However these two cases can not be treated with eq. 1.31, as diffusion in momentum space has to be taken into account. The appropriate description of the problem e.g. in the case of stochastic acceleration is via a Fokker-Planck type momentum diffusion equation (which is also derived from the Boltzmann equation), that includes diffusion in momentum (see Skilling, 1975; Melrose, 1980). Then, the isotropic phase space distribution (averaged over all momentum directions) evolves according to

$$\frac{\partial f}{\partial t} - \frac{1}{p^2}\frac{\partial}{\partial p}\left(p^2 D_p \frac{\partial f(p)}{\partial p}\right) + \frac{f(p)}{\tau} + \frac{1}{p^2}\frac{\partial}{\partial p}\left(p^2 \dot{p} f(p)\right) = Q(p,t). \tag{1.34}$$

Here, the second term represents the stochastic acceleration process and D_p is the momentum-diffusion coefficient. The third and fourth term are, as before, the escape and energy loss terms. For a monoenergetic source term, i.e. $Q(p,t) \propto \delta(p-p_0)$ and if the escape of the particles controls the evolution of the system, then the resulting particle distribution in the steady state is a power-law, harder than in the case of DSA (see e.g. Rieger et al. 2007),

$$dN_e/dE_e \propto E_e^{-1}. \tag{1.35}$$

On the other hand, if (synchrotron-type) energy losses dominate, the steady state solution of the Fokker-Planck equation is a relativistic, Maxwell-type electron distribution,

$$dN_e/dE_e \propto E_e^2 e^{-(\frac{E_e}{E_c})^b}, \tag{1.36}$$

where, E_c denotes the cutoff energy and the index b is the shape of the exponential cutoff. These distributions are extensively discussed in Chapter 2 where we show that they offer an attractive solution to the hard spectrum problem. Furthermore, in chapter 3 we develop a multi-zone scenario according to which the combination of relativistic Maxwell-type distribution can lead to the formation of broad spectra with hard flaring events.

Doppler Boosting

After discussing the acceleration and radiation of the particles as well as the need for a self-consistent approach, the last point for calculating the observed spectrum concerns the Doppler boosting of the emitted luminosity. When the source moves relativistically (as is proven to be the case for AGN jets), its radiation is beamed and the radiated flux enhanced (see e.g. Rybicki & Lightmann 1979). Thanks to special relativity, we can find the relation of the various parameters between the comoving and observed frame that arise from Lorentz transformations. Furthermore, we know that due to light aberration an isotropic spherical source is seen to emit radiation within a small cone of opening angle $\sim 1/\Gamma$, where Γ is the Lorentz factor.

There are however several complications that take place in astrophysical sources. For example, the radiation from a blob and a stationary jet are boosted differently.

Different beaming patterns hold also for the cases of EC and synchrotron/SSC radiation. These questions are addressed in detail in chapter 5. We derive (based on a solution of the photon transfer equation) the beaming patterns in the aforementioned cases for generalized (non-homogeneous, anisotropic, non-stationary) electron distributions.

1.4 Interaction with the EBL

The EBL is the diffuse light between the galaxies that comes from the stars. Its origin is extragalactic and so is expected to be isotropic on large scales. Its spectrum consists of two bumps spreading from UV to far infrared (see fig. 1.3). The first component peaks at wavelengths around $\sim 1\mu m$ and consists of emitted photons from stars. Part of this light is absorbed by dust in the universe and is re-emitted in the infrared energy range, forming the second bump of the EBL which peaks at $\sim 100\mu m$.

Direct measurements of the EBL are very difficult because of strong foreground emissions from the Milky Way and the Sun, especially the zodiacal light (Hauser & Dwek 2001). The exact flux level and shape are still a matter of debate as several authors have attempted to estimate the EBL with different techniques (for a recent review see Domínguez et al. 2011 and references therein). There are basically three approaches to calculate the EBL: (a) *Backward evolution* which starts with the local galaxy population and scales it back in time, as a power-law in the redshift (e.g. Stecker & Scully 2008). Complementary to the aforementioned approach is the attempt to correct for the changing luminosity functions and SEDs with redshift and galaxy type (e.g. Kneiske et al., 2004; Franceschini et al., 2008). (b) *Evolution directly observed and extrapolated* based on a large set of multiwavelength observations (e.g. Domínguez et al. 2011) and (c) *Forward evolution* which begins with initial cosmological conditions and evolves taking into account gas cooling in dark matter halos, formation of galaxies including stars and AGN, feedback for these phenomena, stellar evolution, emission, absorption and re-emission of light from dust (e.g. Gilmore et al. 2012).

Among other, the EBL flux level and shape is highly relevant for understanding the TeV emission from Blazars. The reason is that the TeV photons interact with the EBL photons, through the pair productions process, $\gamma\gamma \rightarrow e^{+}e^{-}$ (see e.g. Gould & Schréder 1967). This mechanism results in the deformation of the intrinsic spectrum because the optical depth depends on the energy of the emitted photons. The deformation usually manifests as a softening, i.e. the observed photon index is larger than the one characterizing the intrinsic spectrum. This effect is more evident for more distant sources as the optical depth depends also on redshift (see fig.1.4). Vice versa, when a soft photon TeV spectrum is observed, then the EBL corrected intrinsic spectrum may be harder. In principle this should not be a problem as we don't know in detail the intrinsic Blazar spectra. However, in some cases the resulting spectra are very hard and can not be simply interpreted within standard leptonic models.

Obviously different models for estimating the EBL lead to different hardness of the intrinsic spectrum, however, there is not a single EBL model for which all sources are soft enough so that standard models can account for the emitted spectra (for an extensive discussion on the hard spectrum sources and the problems arising see Costamante 2012). On the other hand, evaluating the current EBL models only by assuming the non-existence of very hard spectra does not appear to be a valid criterium. As we show in chapter 2, under certain assumptions hard spectra can be formed with leptonic models.

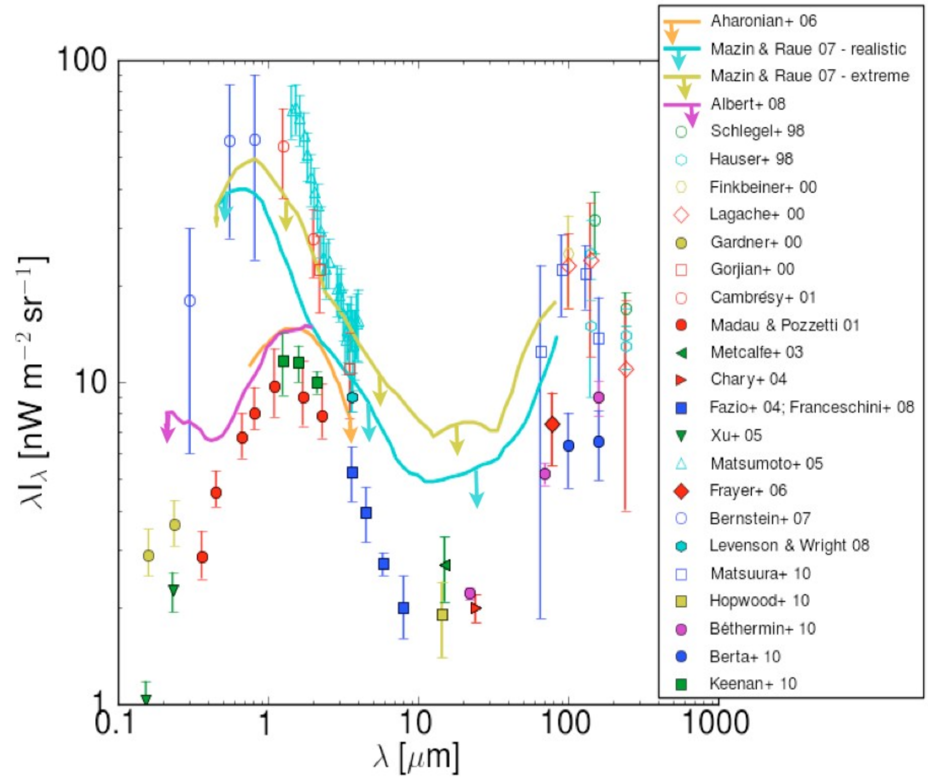

Figure 1.3: The EBL flux level and shape according to different models. The figure is taken from Domínguez et al. 2011

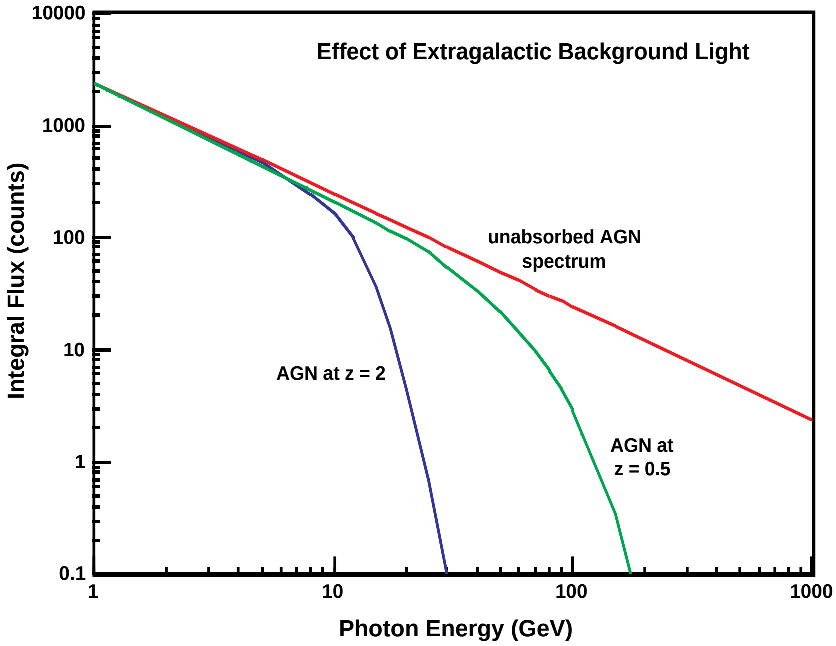

Figure 1.4: Schematic sketch for the deformation of the emitted spectrum due to the interaction of TeV photons with the EBL. Credit: E.D. Bloom (SLAC)

1.5 Aim of this thesis

The main objective of this thesis concerns an in-detail investigation of radiation processes in AGN, embedded in a self consistent treatment, i.e. taking into account the time evolution of the emitting particles, including radiative and non-radiative (e.g. adiabatic) losses. In leptonic models the two basic radiation mechanisms are synchrotron radiation and ICS. Synchrotron-Compton models have been both popular and very often successful in the interpretation of the observed spectra of Blazars. However, there are still unsolved problems and open issues that need to be investigated in the context of leptonic models before alternative solutions are adopted. The most common assumptions concern one-zone modeling and no time evolution. However, in such complex systems like Blazars, these are likely to be oversimplifications. Blazars are often observed in flaring states and furthermore non-homogeneous outflows are expected.

Related issues are addressed in ***chapter 2*** and ***chapter 3***, particularly associated with the "puzzle" of the hard spectrum sources. As far as the AGN physics is concerned, one main open issue is the unusually hard intrinsic Blazar spectra that are revealed after correcting for the EBL. Leptonic models face strong difficulties in interpreting these observations within the standard one-zone models, as they normally predict much steeper spectra in the TeV regime. In ***chapter 2*** we show that such spectra can be self-consistently explained within classical leptonic models once adiabatic losses or stochastic acceleration is taken into account. The basic assumption needed is a narrow electron energy distribution, which can be formed and maintained quite naturally within the aforementioned scheme.

Apart from such self-consistent solutions we can also consider multi-zones for the emitting region. A suitable combination of narrow distributions (as Maxwellian-type electron distributions) may then allow to interpret broader spectra too. Such a scheme is capable of interpreting the broad spectrum of Mkn 501, equally or even better than one smooth function which that is often examined. Furthermore, it allows to explain hard flares, like the one seen in Mkn 501 in 2009, once one (or few) of the components become more energetic, either due to energy enhancement or change of orientation. This consideration is developed within a "leading" blob model which is explored in ***chapter 3***.

Obviously, though for so long and often studied, the leptonic models have more to reveal concerning either one-zone models or more complex and possibly realistic configurations. Even in on more basic level, namely regarding the radiation processes themselves not embedded in a physical model that takes into account the evolution of the particles, there are still unexplored issues proved to be important regarding the information they offer for the physics of the source. One of these issues is the shape of the ICS spectrum close to the high energy cutoff. This is analyzed in ***chapter 4***. By developing analytical approximations we directly link the exponential index as well as the cutoff energy of the emitted spectrum to the corresponding parameters of the parent electron distribution. These formulas allow us to extract crucial information for the electrons and their acceleration process in the source. Additionally, they shed light onto other matters like a possible dependance on the magnetic field from the spatial coordinates, or a more accurate extraction of the source parameters by the comparison of the two peaks of the SED.

Apart from the emission mechanisms themselves, the observed spectrum is affected by the Doppler boosting due to the relativistic motion of the source. This is an essential ingredient for linking the observed flux in respect to the intrinsic flux. In ***chapter* 5** we develop a solution of the photon transfer equation that allows us to derive the different beaming patterns for various processes, i.e. synchrotron radiation, EC and SSC, in a concise way. In these calculation we extend the beaming pattern formulas to include generalized particle distributions, non-stationary, non-homogeneous and non-isotropic. This allows us to examine the interesting case in which the particles exhibit an energy-dependent anisotropy. Interestingly, the observed spectrum does not only exhibit differences as far as the total luminosity is concerned but it also appears harder depending on the angle of observation. In principle, dropping some basic assumptions, like isotropy or homogeneity, can reveal interesting characteristics of the spectrum in respect to one-zone models. To some extend, the "leading" blob model is also a non-homogeneous model, that successfully explains spectral features that the standard models fail to interpret.

Concerning more realistic source configurations, it is particularly interesting to examine non-homogeneous models where the relevant parameters vary in a continuous way. In ***chapter 6*** we investigate an outflow with transverse stratification assuming that particles are injected at the base of the jet, e.g. by DSA at a standing shock. The bulk Lorentz factor, the magnetic field, the particle number density as well as the maximum energy are then assumed to vary across the jet. In a first step we deal only with synchrotron radiation and we show that a variety of stratification consequences arise. For example, the spectrum appears different for different angles of observations. Furthermore special characteristics appear, like additional spectral breaks, which are a direct evidence for non-homogeneous models. In total, even in this first step, the observed (synchrotron) spectrum appears in some cases substantially different from the spectra that corresponds to one-zone models.

Chapter 2

Formation of hard VHE γ-ray Blazar spectra

The very high energy γ-ray spectra of some TeV Blazars, after being corrected for absorption by the extragalactic background light (EBL), appear unusually hard. The interpretation of these hard intrinsic spectra poses challenges to conventional acceleration and emission models. A time-dependent, self-consistent consideration is crucial, because even extremely hard initial electron distributions can be significantly deformed due to radiative energy losses.

The main goal of this chapter is to examine whether very hard γ-ray spectra can be realized in time-dependent leptonic models. We investigate the parameter space that allows for such a consideration both for synchrotron self-Compton (SSC) and external Compton (EC) scenarios. We demonstrate that very steep spectra can be avoided if adiabatic losses are taken into account. Another way to keep extremely hard electron distributions in the presence of losses is to assume stochastic acceleration models that naturally lead to steady-state relativistic, maxwellian-type distributions.

We show that in either case leptonic models can reproduce TeV spectra as hard as $E_\gamma \, dN/dE_\gamma \propto E_\gamma$ for SSC models and $E_\gamma \, dN/dE_\gamma \propto E_\gamma^{1/3}$ in an EC scenario. Unfortunately this limits, to a large extend, the potential of extracting EBL from gamma-ray observations of Blazars[1].

2.1 The puzzle of hard γ-ray Blazar spectra

Though the standard one-zone SSC model, as well as the EC model, have been the bread and butter for interpreting the high energy spectrum of Blazars, some recent detections of VHE (Very High Energy) γ-rays from Blazars at redshift $z \geq 0.1$ (in particular, 1ES 1101-232 at $z = 0.186$ and 1ES 0229+200 at $z = 0.139$), pose challenges to the conventional leptonic interpretation. As discussed in detail in the introduction, VHE γ-rays emitted by such distant objects arrive after significant absorption caused by their interactions with extragalactic background light

---

[1] The results discussed in this chapter are based on Lefa et al. 2011

(EBL) via the process $\gamma\gamma \rightarrow e^+e^-$ (e.g., Gould & Schréder 1967). Reconstruction of the absorption-corrected intrinsic VHE γ-ray spectra based on state-of-the-art EBL models then yields unusually hard VHE source spectra, that are difficult to account for with the standard inverse Compton assumption.

The difficulty lies in the effect that the radiation losses have on the emitting electron distribution. Even if we (continuously) inject in the source the hardest possible distribution, monoenergetic electrons, i.e. $Q(\gamma) \propto \gamma\delta(\gamma - \gamma_*)$, then synchrotron-type losses will result in the development of a power-law distribution of the form $n_e(\gamma) \propto \gamma^{-2}$, as one can directly see from solution of the kinetic equation in the steady-state case

$$n_e(\gamma) \propto \frac{1}{\dot{\gamma}} \int_{\gamma}^{\infty} \gamma\delta(\gamma - \gamma_*) d\gamma \propto \gamma^{-2}\Theta(\gamma_* - \gamma). \tag{2.1}$$

Note that hard VHE emission spectra can not be achieved even if one assumes that particles cool due to ICS in the Klein-Nishina regime, in which case the steady state particle distribution would indeed be harder due to the different energy dependance of the radiative losses (roughly speaking $\dot{\gamma}_{KN} \propto \ln 4\gamma\epsilon/mc^2$, see e.g. Blumenthal & Gould 1970). Nevertheless, this modification would have a strong impact only on the synchrotron component of the spectrum, but not in the TeV energy band, because the particle distribution hardening is compensated by the reduction of the scattering efficiency (Moderski et al. 2005). The characteristic γ^{-2} behavior of the electron distribution results in a photon spectrum of the form $dN_\gamma/dE_\gamma \propto E_\gamma^{-\Gamma}$, with a photon index of $\Gamma = 1.5$. Sources with smaller photon indices have been reported. Even the 1.5 photon index is difficult to achieve, as these sources peak at very high energies where Klein-Nishina effects make the spectrum even steeper.

Current uncertainties on the EBL flux level and spectrum (cf. Primack et al. 2011 for a recent review) introduce difficulties in defining how hard the absorption-corrected source spectra are. However, for some sources the emitted spectra still tend to be very hard, with an intrinsic photon index $\Gamma \leq 1.5$, even when corrected for low EBL flux levels (Aharonian et al., 2006, 2007a). One characteristic case concerns the distant (at $z = 0.186$) Blazar 1ES 1101-232, detected at VHE γ-ray energies by the H.E.S.S. (High Energy Stereoscopic System) array of Cherenkov telescopes (Aharonian et al., 2006, 2007a). When corrected for absorption by the EBL, the VHE γ-ray data result in very hard intrinsic spectra, with a peak in the SED above 3 TeV and a photon index $\Gamma \leq 1.5$ (see e.g. fig. 2.1). A similar behavior has also been detected in the BL Lacertae 1ES 0347-121 at $z = 0.188$ (Aharonian et al. 2007) whereas even more extreme values for the de-absorbed photon index were reported for the TeV Blazar 1ES 0229+200 at z=0.139 (Aharonian et al. 2007b). Though there is a non-negligible uncertainty in the EBL flux, the intrinsic spectra are unusually hard even when one considers the lowest levels of the EBL (Franceschini et al. 2008). Other models predicting higher EBL flux lead to even harder photon index close to 1 (e.g., Stecker & Scully 2008).

Interestingly, a recent analysis of Fermi LAT data for the nearby TeV Blazar Mkn 501 indicates a hard γ-ray spectrum (Γ close to 1) at lower (10-200 GeV) energies (Neronov et al. 2011). Already in the original paper by the FERMI collaboration

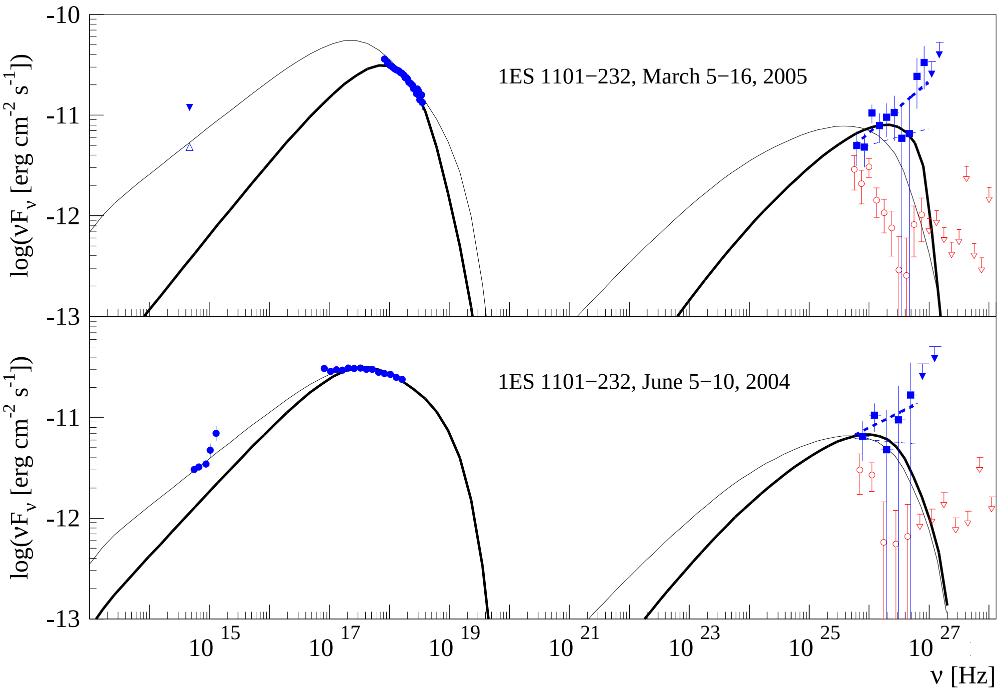

Figure 2.1: Spectral energy distribution of 1ES1101-232 for two different epochs (figure taken from Aharonian et al. 2007). Open red circles denote the H.E.S.S. data whereas the blue data at the TeV range represent the de-absorbed spectrum. With black lines a homogeneous SSC model is presented, which fails to fit the ICS part of the spectrum in both periods.

(Abdo et al. 2011), a strong spectral hardening is indicated during the ∼ 30 days flare. This is strong evidence for unusually hard γ-ray spectra independent of the question related to the level of EBL. Another (extreme) example for the existence of hard spectra regards the MAGIC observations of the Quasar 3C279 at z=0.536 (Aleksić et al. 2011) during 2007 and 2009. In January 2007 a very short flare was detected (on timescales of a day) for which an extremely hard intrinsic spectrum, $\Gamma = -0.32 \pm 1.01$ was inferred. Though the error bars are large, even the lower limit for the photon index implies a hard flare.

Apart from the challenges arising for inverse Compton interpretations, hard VHE spectra obviously carry important information about the level of the EBL, and thus a deep understanding of the mechanisms acting within these sources becomes now even more critical.

2.2 Suggested solutions

The "simplest" way to overcome the problem is to assume that there is no absorption. In fact, this is possible in Lorentz invariance violation scenarios (Kifune 1999). The break of Lorentz invariance above a certain energy will be imprinted at the mass shell condition with an additional term $\Phi(p, M, \mu)$ that depends on the mass, the momentum and an arbitrary constant μ related to the model which is assumed for the symmetry breaking

$$\eta_{ij} p^i p^j = m^2 + \Phi(p, M, \mu). \tag{2.2}$$

The parameter M is a constant related to the scale at which the threshold anomaly becomes important. Here, $\eta_{ij} = (+, -, -, -)$ is the Minkowski metric and $p^i = (E, -\vec{p})$ the four-momentum. For the pair production process the above modified relation in combination with energy and momentum conservation alter the threshold of the interaction, since

$$2\epsilon E_\gamma (1 - \cos\theta) - 2E_\gamma^2 \Phi(p, M, \mu) > 4m^2, \tag{2.3}$$

preventing the TeV photons to interact with the infrared photons of the EBL. We should note however that this effect is likely to be true only above 2 TeV (Stecker & Glashow 2001), whereas the hard spectra problem that we face in the case of distant Blazars is relevant to sub-TeV energies as well.

Another non standard mechanism to avoid severe absorption in the EBL has been suggested by De Angelis et al. (2009) (see also Hooper & Serpico 2007) who proposed that the γ-ray photon is mixing with a very light axion-like particle (ALP). These ALPs propagate unaffected by the EBL, reducing in this way the mean free path of the photons and thus allowing softer intrinsic spectra. However, this scenario requires the existence of exotic particles. To some extend a similar idea was suggested by Essey et al. (2011) who assumed that the γ-rays from Blazars may be dominated by secondary γ-rays produced along the line of sight by the interactions of cosmic-ray protons with background photons. While primary γ-rays emitted by the Blazar are attenuated in their interactions with the EBL, cosmic rays with energies 10^{16} - 10^{19} eV can cross cosmological distances and produce secondary γ-rays in their interactions with the background photons. Protons are deflected by magnetic fields and thus this mechanism leads to upper bounds of the intergalactic magnetic field (see also Essey & Kusenko, 2010; Essey et al., 2010; Essey & Kusenko, 2012; Prosekin et al., 2012), which have not yet been confirmed by an alternative method of magnetic field estimation.

In more standard astrophysical scenarios, formation of hard γ-ray spectra could be related to production and absorption processes. Photon-photon absorption can result in arbitrarily hard spectra provided that the γ-rays pass through a hot photon gas with a narrow distribution such that $E_\gamma \epsilon_o \gg mc^2$. In this case, due to the reduction of the cross-section the source becomes optically thick at lower energies and thin to higher energies leading to formation of hard intrinsic spectra (Aharonian et al., 2008; Zacharopoulou et al., 2011). In such a scheme the primary TeV spectrum could be due to synchrotron radiation of protons, whereas the low energy part is attributed to synchrotron radiation of secondary electrons.

Finally, if we relate the hard γ-ray spectra to the production process then this implies hard parent particle distribution. Outside standard leptonic models, a number of alternative explanations have been explored in the literature. In analogy to pulsar winds, Aharonian et al. (2002) have analyzed the implications of a cold ultra-relativistic outflow that initially (close to the black hole) propagates at very high velocities. In this case, upscattering of ambient photons can yield sharp pile-up features in the intrinsic source spectra. However, very high bulk Lorentz factors would be required ($\Gamma_b \sim 10^7$) and it seems not clear whether such a scenario can be applied to Blazars. On the other hand, if Blazar jets would remain highly relativistic out to kpc-scales ($\Gamma_b \sim 10$) and able to accelerate particles, a hard (slowly variable) VHE emission component could perhaps be produced by Compton up-scattering of CMB (Cosmic Microwave Background) photons (Böttcher et al. 2008).

Hard spectra can occur in standard leptonic scenarios as well. In order to produce hard γ-ray spectra, hard electron energy distributions are required. Although standard shock acceleration theories, both in the non-relativistic and relativistic regime, predict quite broad, $n(E_e) \propto E_e^{-2}$-type, electron energy distributions, there are non-conventional realizations which could give rise to very hard spectra (Derishev et al., 2003; Stecker et al., 2007). On a more phenomenological level, Katarzyński et al. (2006) have shown that the presence of an energetic power-law electron distribution with a high value of the minimum cutoff energy can lead to a hard TeV spectrum. In general, however, injection of a hard electron distribution is not a sufficient condition as electrons are expected to quickly lose their energy due to radiative cooling and thereby develop a standard $n(E_e) \propto E_e^{-2}$ form below the initial cutoff energy. In order to avoid synchrotron cooling, one needs to assume unrealistically small values for the magnetic field (Tavecchio et al. 2009).

In this chapter we explore the conditions under which a narrow, energetic particle distribution is able to successfully account for the hard VHE source spectra in time-dependent leptonic models. To this end, we examine different electron distributions within the context of standard leptonic models, i.e. the one-zone SSC and the external Compton scenario. We show that time-dependent generalization including adiabatic losses can self-consistently allow for hard TeV spectra to be maintained, without the need to avoid energy losses. As a second alternative, we discuss pile-up (Maxwellian-type) electron distributions that are formed in stochastic acceleration scenarios. These distributions are steady state solutions for which radiative (synchrotron or Thomson) losses are already included. They provide an interesting explanation for very hard TeV components as their radiation spectra share many characteristics with the (hardest possible) mono-energetic distributions.

2.3 Stationary SSC with an energetic electron distribution

Within a stationary SSC approach, the hardest possible (extended) VHE spectrum is approximately $F_\nu \propto \nu^{1/3}$, where $F_\nu = dF/d\nu$ is the spectral flux (differential flux per frequency band). This has a simple explanation: As discussed in the introduction, the emitted synchrotron spectrum of a single electron with Lorentz factor γ in a magnetic field B, averaged over the particle's orbit, obeys $j(\nu, \gamma) \propto G(x)$, where $G(x)$ is a dimensionless function with $x = \nu/\nu_c$ and $\nu_c \equiv 3\gamma^2 eB \sin\alpha/(4\pi m_e c)$. For $x \ll 1$, the functional dependence of $G(x)$ is well approximated by $G(x) \propto x^{1/3}$, while for $x \gg 1$ one has $G(x) \propto x^{1/2} e^{-x}$ (e.g., Rybicki & Lightmann 1979). Hence, at low frequencies $\nu \ll \nu_c$, the synchrotron spectrum follows $j(\nu) \propto \nu^{1/3}$. Compton upscattering of such a photon spectrum in the Thomson regime by a very energetic, narrow electron distribution will preserve this dependence and therefore yield a VHE spectral wing as hard as $F_\nu \propto \nu^{1/3}$ as shown below.

2.3.1 Power-law electron distribution with high value of low-energy cutoff

A homogeneous SSC scenario with a high value for the low-energy cutoff of the non-thermal electron distribution has consequently been proposed by Katarzyński et al. (2006) in order to overcome the problem of the Klein-Nishina suppression of the cross-section at high energies and reproduce VHE spectra as hard as 1/3. Let us assume that the electron population follows a power-law distribution of index p between the low- and high-energy cutoffs

$$N'_e(\gamma') = K'_e \gamma'^{-p}, \quad \gamma'_{\min} < \gamma' < \gamma'_{\max}\,, \tag{2.4}$$

as often used in modeling the Blazar spectra. Here, prime quantities refer to the blob rest frame and unprimed to the observer's frame. Taking relativistic Doppler boosting (D) into account, the observed synchrotron flux from an optically thin source at distance d_L is given by the integral of $N'_e(\gamma')d\gamma'$ times the single particle emissivity $j'(\nu', \gamma')$ over the volume element and all energies γ' (e.g., Begelman et al. 1984), i.e.

$$F_\nu^{\rm syn} = \frac{D^3}{d_L^2} \int_{V'} \int_{\gamma'} j'(\nu', \gamma') N'_e(\gamma') d\gamma' dV'\,. \tag{2.5}$$

The above expression yields the common power-law of index $\alpha = (p-1)/2$ between the frequency limits $\nu_{\min} \propto D(B\gamma_{\min}^2)$ and $\nu_{\max} \propto D(B\gamma_{\max}^2)$. Below and above those limits, the electrons with energy around the minimum and maximum cutoff dominates and thus the spectrum approximately exhibits a slope $F_\nu \propto \nu^{1/3}$ for $\nu < \nu_{\min}$, and an exponential cutoff for $\nu > \nu_{max}$, i.e.

$$F_\nu^{\rm syn} \propto \begin{cases} \nu^{1/3}, & \nu \ll \nu_{min} \\ \nu^{-\frac{p-1}{2}}, & \nu_{min} \le \nu \le \nu_{max} \\ \nu^{1/2} e^{-\nu}, & \nu \gg \nu_{max} \end{cases} \tag{2.6}$$

The hard 1/3-slope appears in the VHE range of EC γ-rays when the synchrotron photons are up-scattered to higher energies by the electron population given by equation (2.4) with a high $\gamma_{\min}$ and provided that the Thomson regime applies. Obviously, in the Klein-Nishina regime it will be significantly steeper. In any case, however, there exists a characteristic energy below which the Compton spectrum mimics the behavior of the synchrotron spectrum $F_\nu \propto \nu^{1/3}$.

Note that the ICS spectrum of a monochromatic photon field by monoenergetic electrons approximately follows $F_\nu \propto \nu$ at low energies (cf. Blumenthal & Gould 1970). Thus, any photon field which is softer (flatter) than $F_\nu \propto \nu$ will dominate the lower-energy part of the up-scattered emission and thus, in the standard SSC scenario the 1/3-VHE slope (the 4/3-slope in the νF_ν representation) is the hardest that can be achieved.

An exception to this may occur if the magnetic field in the source would be fully turbulent with zero mean component. In such a case, the low-frequency part of the synchrotron spectrum could be harder than $F_\nu \propto \nu^{1/3}$ (Medvedev, 2006; Derishev et al., 2007; Reville & Kirk, 2010), which will be reflected to low energy part of the Compton component.

The "critical Compton energy" is usually $\epsilon_{\rm min} \simeq D\gamma_{\rm min}^2(b\gamma_{\rm min}^2)$, where $b \equiv (B/B_{cr})m_e c^2$, $B_{cr} = m_e^2 c^3/(e\hbar)$, except for the case of deep Klein-Nishina (KN) regime, i.e., when up-scattering of the minimum synchrotron photons by the minimum energy electrons occurs in the KN regime so that $\frac{4}{3}b\gamma_{\rm min}^3 > 1$. If the latter applies, then the corresponding energy below which one can see the hard 1/3-slope is, as expected, $\gamma_{\rm min} m_e c^2$, and it approximately corresponds to the peak of the emitted luminosity for any power-law electron index (see Fig. 2.2). In total

$$F_\nu^{\rm SSC} \propto \nu^{1/3}, \quad \nu < \nu_{min}^c \propto \begin{cases} B\gamma_{min}^3 & if \;\; \frac{4}{3}b\gamma_{min}^3 < 1 \\ \gamma_{min} & if \;\; \frac{4}{3}b\gamma_{min}^3 > 1 \end{cases} \tag{2.7}$$

In the KN regime, the peak appears especially sharp (e.g., Tavecchio et al. 1998), and the Compton flux has a strong inverse dependence on the value of $\gamma_{\rm min}$. For example, for the realization presented in Fig. (2.2), the emissivity in this regime roughly scales as $j^C \propto \gamma_{\rm min}^{-2.5}$, so that slight changes in $\gamma_{\rm min}$ can lead to significant variations in amplitude of the Compton peak flux. On the other hand, as long as $p < 3$ (positive synchrotron slope in a νF_ν representation) the synchrotron peak luminosity would remain approximately constant.

A power-law electron distribution with a large low-energy cutoff has been used in Tavecchio et al. (2009) in order to reproduce the SED of the Blazar 1ES 0229+200 within a stationary SSC approach. The high value of $\gamma_{\rm min} \sim 10^5$ then ensures that the hard Compton part of the spectrum with 1/3-slope is in the TeV range. The generic difficulty for such an approach is that an energetic electron distribution is expected to quickly develop a γ^{-2}-tail below $\gamma_{\rm min}$ due to synchrotron cooling, thereby making the Compton VHE spectrum softer (see Fig. 2.3). To overcome this problem, Tavecchio et al. (2009) suggested an unusually low value for the magnetic field, $B \sim (10^{-4} - 10^{-3})$ G, that would allow the electron distribution to remain essentially unchanged on timescales of up to a few years. Obviously, one would then not expect to observe significant variability on shorter timescales. We should note however that this requirement can be relaxed if one assumes that the detected γ-ray signal is a superposition of short flares which can not be individually detected.

Arguments based on magnetic flux conservation naively suggest that the magnetic field value, when scaled from the black hole region to the emission site, should be at least one or two orders of magnitude larger so that one would need to destroy magnetic flux for such a scenario to work. On the other hand, a narrow but very energetic electron distribution in combination with such low magnetic field strengths implies a strong deviation from equipartition, thereby obviously facilitating an expansion of the source.

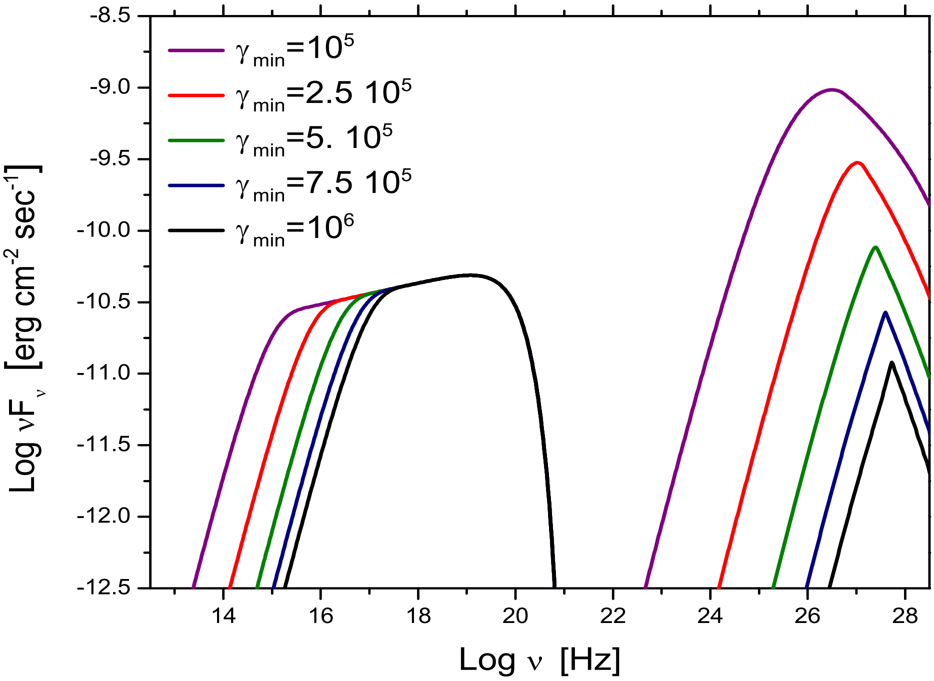

Figure 2.2: Stationary SSC spectra for different values of the low-energy cutoff. Above $\gamma_{\rm min} \sim 3 \times 10^5$ we are very deep in the Klein-Nishina regime and the peak of the Compton emission appears very sharp. As one reduces $\gamma_{\rm min}$, the suppression of the cross-section decreases and the minimum Compton energy drops to lower energies. Thus, the peak of the Compton flux raises significantly, whereas the synchrotron peak remains constant. A Doppler factor $D = 50$ has been used.

2.3.2 Relativistic Maxwellian electron distribution

As far as a narrow energetic particle distribution is concerned, a relativistic Maxwellian distribution may come as a more natural representation. Such an electron distribution can be the outcome of a stochastic acceleration process (e.g., 2nd order Fermi) that is balanced by synchrotron (and/or Compton) energy losses, or in general any energy loss mechanism that exhibits a quadratic dependence on the particle energy (see e.g., Schlickeiser, 1985; Aharonian et al., 1986; Henri & Pelletier, 1991; Stawarz & Petrosian, 2008).

Consider for illustration the Fokker-Planck diffusion equation which describes the stationary distribution function $f(p)$ of electrons that are being accelerated by, e.g., scattering off randomly moving Alfvén waves in an isotropic turbulent medium,

$$\frac{1}{p^2}\frac{\partial}{\partial p}\left(p^2 D_p \frac{\partial f(p)}{\partial p}\right) + \frac{1}{p^2}\frac{\partial}{\partial p}\left(\beta_s p^4 f(p)\right) = 0\,, \tag{2.8}$$

where D_p is the momentum-space diffusion coefficient. Particle escape is neglected in eq. (2.8), as the timescale for synchrotron cooling is expected to be much smaller

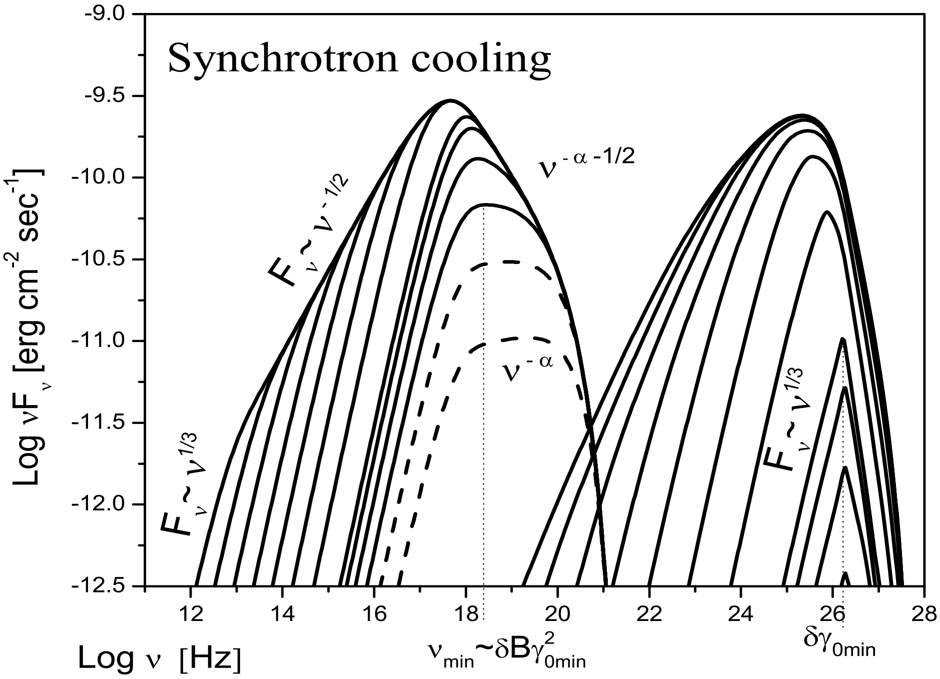

Figure 2.3: Evolution of the observed SSC spectrum for constant injection of a narrow power-law electron distribution, with modifications due to synchrotron cooling taken into account. The magnetic field is $B = 1G$. The hard (1/3) synchrotron and Compton spectral wings are observed for timescales shorter than the cooling timescale of the γ_0-particles, i.e., in the present application for timescales ≤ 0.1 days. The figure shows the expected spectral evolution for a total (observed) time $t \sim 1$ day. Parameters used are $R_0 = 7.5 \times 10^{14}$ cm, $\gamma_{\rm min} = 7 \times 10^4$, $\gamma_{\rm max} = 2 \times 10^6$, power law index $p = 2.85$ and Doppler factor $D = 25$. The total injected power is $Q \sim 10^{41}$ erg/sec.

than the one for electron escape.

For scattering off Alfvén waves, one has $D_p = \frac{p^2}{3\tau}(\frac{V_A}{c})^2 \equiv D_0 p^{2-\alpha_p}$, with $V_A = \frac{B}{\sqrt{4\pi\rho}}$ the Alfvén speed and $\tau = \lambda/c \propto p^{\alpha_p}$, $\alpha_p \geq 0$, the mean scattering time (e.g., Rieger et al. 2007). If the turbulent wave spectrum $W(k) \propto k^{-q}$ is assumed to be Kolmogorov-type ($q \simeq 5/3$) or Kraichnan-type($q = 3/2$), the momentum-dependence becomes $\alpha_p = 1/3$ and $\alpha_p = 1/2$, respectively. Bohm-type diffusion, on the other hand, would imply $\alpha_p = 1$, while hard-sphere scattering is described by $\alpha_p = 0$. Note, however, that if one considers electron acceleration by resonant Langmuir waves, even $D_p = $ const ($\alpha_p = 2$) may become possible (Aharonian et al. 1986).

The synchrotron energy losses that appear in the second term of Eq. (2.8) are

$$\frac{dp}{dt} = -\beta_s p^2 = -\frac{4}{3}(\sigma_T/m_e^2c^2)U_B p^2 \tag{2.9}$$

In the γ-parameter space, the solution of Eq. (2.8) yields a relativistic Maxwell-like energy distribution,

$$dN_e(\gamma)/d\gamma = f(\gamma) = A\gamma^2 e^{-\left(\frac{\gamma}{\gamma_c}\right)^{1+\alpha_p}}\,, \tag{2.10}$$

($\alpha_p \neq -1$) with

$$\gamma_c = \left(\frac{[1+\alpha_p]D_0}{\beta_s}\right)^{1/(1+\alpha_p)} (m_e c^2)^{-1}\,, \tag{2.11}$$

and constant A to be defined by the initial conditions. Note that this is a steady-state solution including radiative losses and there is no need to invoke extreme values for the magnetic field. The critical Lorentz factor γ_c approximately corresponds to the energy at which acceleration on timescale

$$t_{\rm acc} = \frac{3}{4-\alpha_p}\left(\frac{c}{V_A}\right)^2 \tau \tag{2.12}$$

is balanced by (synchrotron) cooling on timescale $t_{\rm cool} = 1/[\beta_s p]$. Depending on the choice of parameters, a relatively large range of values for γ_c is possible and thus, cutoff energies of the order of $\gamma_c \sim 10^5$ may well be achieved. Consider, for example, Bohm-type diffusion with $\tau = \eta r_g/c$, $r_g = \gamma m_e c^2/(eB)$ the electron gyro-radius and $\eta \geq 1$. Using $t_{\rm acc} = t_{\rm cool}$, the maximum electron Lorentz factor becomes $\gamma_c \simeq 10^6\ (v_A/0.01c)\ (1\ {\rm G}/B)^{1/2}\eta^{-1/2}$.

The synchrotron spectrum that arises from a Maxwell-like electron distribution is dominated by the emission of electrons with γ_c (Fig. 2.4). It exhibits the characteristic 1/3-slope up to the corresponding "synchrotron cutoff frequency" $h\nu_c^{\rm syn} \sim Db\gamma_c^2$ where $b = B/B_{cr}$ and $B_{cr} = m^2c^3/e\hbar$. Thus the Compton spectrum is very similar to the one resulting from a narrow power-law if one chooses a value for the cutoff energy close to the minimum electron energy of the power-law distribution. The peak of the Compton flux then contains information for the cutoff energy as $\nu^c_{\rm peak} \propto \gamma_c$.

Note that for an electron distribution of the form of eq. (3.1) that exhibits an exponential cutoff $\propto \exp[-(\gamma/\gamma_c)^\beta]$, the corresponding cutoff in the synchrotron spectrum appears much smoother, $\propto \exp[-(\nu/\nu_*)^{\beta/(\beta+2)}]$ (Fritz, 1989; Zirakashvili & Aharonian, 2007). The position of the synchrotron peak flux, ν_p, is then also dependent on β, and one can show that for $\beta = 1$ (or $\alpha_p = 0$ in the previous notation) an important factor ~ 10 arises, so that $\nu_p = 9.5\nu_c$, whereas for $\beta = 3$ the synchrotron peak corresponds approximately to the electron cutoff as $\nu_p = 1.2\nu_c$ (e.g., Fig. 2.4). For an extended discussion on the cutoff energies for the synchrotron and ICS spectrum see chapter 4.

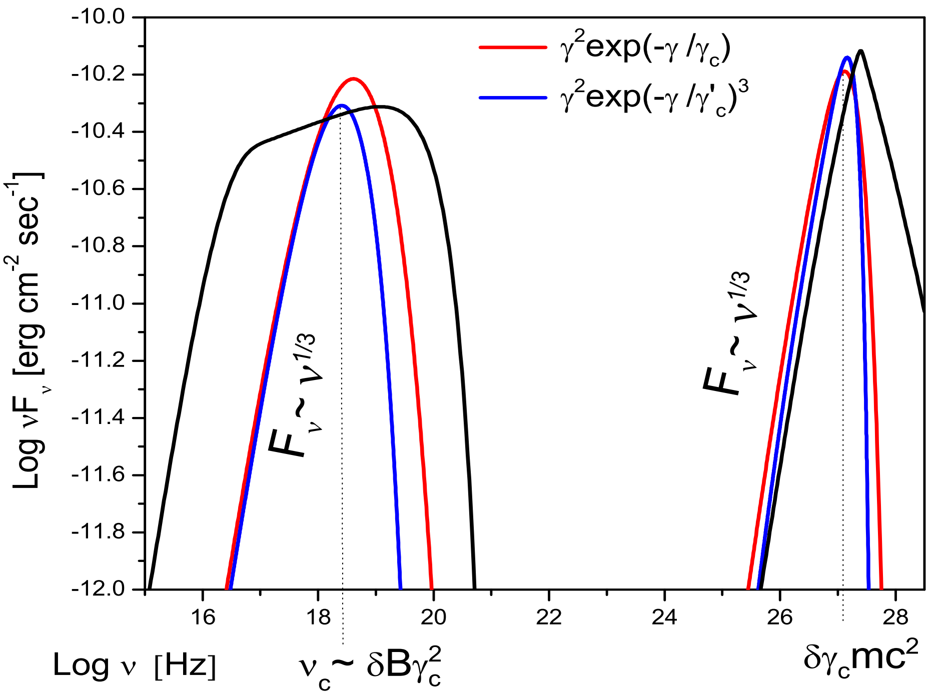

Figure 2.4: SSC modeling with different electron distributions. **Black line:** *Power-law* with large value of the minimum energy (as in Tavecchio et al. 2009). The parameters used are $\gamma_{\rm min} = 5 \times 10^5$, $\gamma_{\rm max} = 4 \times 10^7$, power law index $p = 2.85$, $B = 4 \times 10^{-4}$ G, $k_e = 6.7 \times 10^8$ cm^{-3}, $R = 5.4 \times 10^{16}$ cm and Doppler factor $D = 50$. **Red line:** Relativistic *Maxwellian* distribution $N_e = K_e \gamma^2 \exp(-\frac{\gamma}{\gamma_c})$ with parameters $\gamma_c = 1.5 \times 10^5$, $B = 0.07$ G, $K_e = 3 \times 10^{-14}$cm^{-3}, $R = 2 \times 10^{14}$cm and $D = 33$. The peak of Compton flux occurs in the KN regime as $(B/B_{cr})\gamma_c^3 \simeq 160 \gg 1$. **Blue line:** Relativistic *Maxwellian* distribution $N_e = K_e \gamma^2 \exp(-\frac{\gamma}{\gamma_c})^3$ with parameters $\gamma_c = 5.3 \times 10^5$, $B = 0.06$ G, $K_e = 4 \times 10^{-15}$ cm^{-3}, $R = 2 \times 10^{14}$ cm and $D = 33$.

2.4 Time dependent case - expansion of the source

Expansion of the source could change the conclusions drawn above. In particular, if one assumes a very low magnetic field such that synchrotron losses are negligible, then adiabatic losses may become important and alter the electron distribution. In this section, we examine the behavior of the system for a power-law electron distribution with a high value of the low-energy cutoff discussed above. For simplicity, we consider a spherical source that expands with a constant velocity u,

$$R(t) = R_0 + u(t - t_0)\,. \tag{2.13}$$

The relativistic electron population will be affected by synchrotron losses,

$$P_{\rm syn} = -\frac{d\gamma}{dt} = \frac{\sigma_T B(t)^2 \gamma^2}{6\pi m_e c}\,, \tag{2.14}$$

and by adiabatic losses (e.g., Longair 1982),

$$P_{\rm ad} = -\frac{d\gamma}{dt} \simeq \frac{1}{3}\frac{\dot{V}}{V}\gamma = \frac{\dot{R}(t)}{R(t)}\,\gamma = \frac{u}{R(t)}\,\gamma\,. \tag{2.15}$$

As the emission region expands, the magnetic field decreases. We consider a scaling $B \propto (1/R)^m \propto (1/t)^m$ with $1 \leq m \leq 2$ to study the evolution of the system. The limiting value $m = 2$ corresponds to conservation of magnetic flux for the longitudinal component, whereas $m = 1$ holds for the perpendicular component. (Note that for $m = 1$ the ratio of the electrons' energy density to the magnetic field energy density remains constant). Which energy loss process then determines the electron behavior depends mainly on the magnetic field strength and the size of the source. A simple comparison of the above relations shows that when $P_{\rm ad} > P_{\rm syn}$, i.e.,

$$B(t)^2 R(t) < \frac{6\pi m_e c^2}{\sigma_T}\left(\frac{u}{c}\right)\frac{1}{\gamma} = 2.3\times 10^{19}\left(\frac{u}{c}\right)\frac{1}{\gamma} \tag{2.16}$$

adiabatic losses dominate over radiative losses. For example, if one considers expansion at speed $u \sim c$ and an initial source dimension $R_0 \sim 10^{14}$ cm, then for energies below $\gamma \sim 10^7$ the magnetic field can be as large as $B \sim 0.1$ G and for energies less than $\gamma \sim 10^5$ the adiabatic losses are still dominant for a value of $B \sim 1$ G. If the expansion of the source would not affect the hard slope at TeV energies, this could thus allow for a relaxation of the values used for SSC modeling of the source. In order to investigate this scenario in more detail, one needs to solve the electrons' kinetic equation

$$\frac{\partial N_e(\gamma,t)}{\partial t} = \frac{\partial}{\partial \gamma}\left(P_{\rm ad} N_e(\gamma,t)\right) - \frac{N_e(\gamma,t)}{\tau_e} + Q(\gamma,t)\,, \tag{2.17}$$

where τ_e is the characteristic escape time and N_e the differential electron number. For simplicity, we neglect the escape term ($\tau_e \to \infty$), assuming that the sources expands with relativistic speeds $u \sim (0.1-1)$c. For a constant expansion rate and continuous injection with rate $Q(\gamma, t) \rightarrow Q(\gamma, R)$, we can replace the time variable t by the source dimension R. Then, the general solution of the kinetic equation (eq. (30) from Atoyan & Aharonian 1999) for the case of dominance of adiabatic losses is reduced to

$$N_e(\gamma, R) = \frac{R}{R_0}\, N_0\left(\frac{R}{R_0}\gamma\right) + \frac{1}{u}\int_{R_0}^{R} \frac{R}{r}\, Q\left(\frac{R}{r}\gamma, r\right) dr\,, \tag{2.18}$$

where the first term corresponds to the initial conditions, the contributions of which quickly disappears, and the second term relates to the continuous injection of relativistic electrons. R_0 is the source dimension at the initial time t_0.

We consider zero initial conditions ($N_0 = 0$) and power-law injection of relativistic particles at constant rate

$$Q(\gamma, R) = Q_0\gamma^{-p_1}\ \Theta(\gamma - \gamma_{0,\mathrm{min}})\Theta(\gamma_{0,\mathrm{max}} - \gamma)\Theta(R - R_0)\,, \tag{2.19}$$

where Θ denotes the unit step function

$$\Theta(x - x_0) = \begin{cases} 1, & x > x_0 \\ 0, & x < x_0\,, \end{cases} \tag{2.20}$$

$p_1 > 0$ is the momentum index and R_0 the radius at which injection starts. At radius R, electrons with initial cutoff energies $\gamma_{0,\mathrm{min}}$ and $\gamma_{0,\mathrm{max}}$ will have energies $\gamma_{R,\mathrm{min}}$ and $\gamma_{R,\mathrm{max}}$, respectively, as they evolve according to Eq. (2.15), i.e. we have

$$\gamma_R = \gamma_0\frac{R_0}{R(t)} \propto \frac{1}{t}\,. \tag{2.21}$$

From the properties of the step-function, the integral can be written as

$$\begin{aligned} N_e(\gamma, R) &= \frac{Q_0\gamma^{-p_1}}{u}\int_{R_0}^{R}\left(\frac{R}{r}\right)^{1-p_1}\Theta\left(r - \frac{R\gamma}{\gamma_{0,max}}\right)\Theta\left(\frac{R\gamma}{\gamma_{0,min}} - r\right) dr \\ &= \frac{Q_0\gamma^{-p_1}}{u}\int_{max[R_0,\frac{R\gamma}{\gamma_{0,max}}]}^{min[R,\frac{R\gamma}{\gamma_{0,min}}]}\left(\frac{R}{r}\right)^{1-p_1} dr \end{aligned} \tag{2.22}$$

The comparison of the values for the lower and maximum limits of integration will result in the different branches of the solution, whereas ensuring that the two limits do not overlap reveals a critical radius $R_* = R_0\gamma_{0,\mathrm{max}}/\gamma_{0,\mathrm{min}}$ at which $\gamma_{R,\mathrm{max}}$, i.e. the energy of an electron with initial injected energy $\gamma_{0,\mathrm{max}}$ at R, becomes less than the initial $\gamma_{0,\mathrm{min}}$. The following two cases can be distinguished:

For $R < R_*$, or equivalently as long as $\gamma_{\mathrm{R,max}} > \gamma_{0,\mathrm{min}}$, we have

$$N(\gamma, R) = \frac{Q_0}{p_1 u}R\begin{cases} \gamma^{-p_1}\left[1 - \left(\frac{\gamma}{\gamma_{0,\mathrm{max}}}\right)^{p_1}\right], & \gamma_{\mathrm{R,max}} < \gamma < \gamma_{0,\mathrm{max}} \\ \gamma^{-p_1}\left[1 - \left(\frac{R_0}{R}\right)^{p_1}\right], & \gamma_{0,\mathrm{min}} < \gamma < \gamma_{\mathrm{R,max}} \\ \gamma_{0,\mathrm{min}}^{-p_1} - \left(\frac{R\gamma}{R_0}\right)^{-p_1}, & \gamma_{\mathrm{R,min}} < \gamma < \gamma_{0,\mathrm{min}} \end{cases} \tag{2.23}$$

For $R > R_*$, or equivalently as long as $\gamma_{\rm R,max} < \gamma_{\rm 0,min}$, the solution is

$$N(\gamma, R) = \frac{Q_0}{p_1 u} R \begin{cases} \gamma^{-p_1} \left[1 - \left(\frac{\gamma}{\gamma_{0,max}}\right)^{p_1}\right], & \gamma_{0,min} < \gamma < \gamma_{\rm 0,max} \\ \gamma_{\rm 0,min}^{-p_1} - \gamma_{\rm 0,max}^{-p_1}, & \gamma_{\rm R,max} < \gamma < \gamma_{\rm 0,min} \\ \gamma_{\rm 0,min}^{-p_1} - \left(\frac{R\gamma}{R_0}\right)^{-p_1}, & \gamma_{\rm R,min} < \gamma < \gamma_{\rm R,max} \end{cases} \tag{2.24}$$

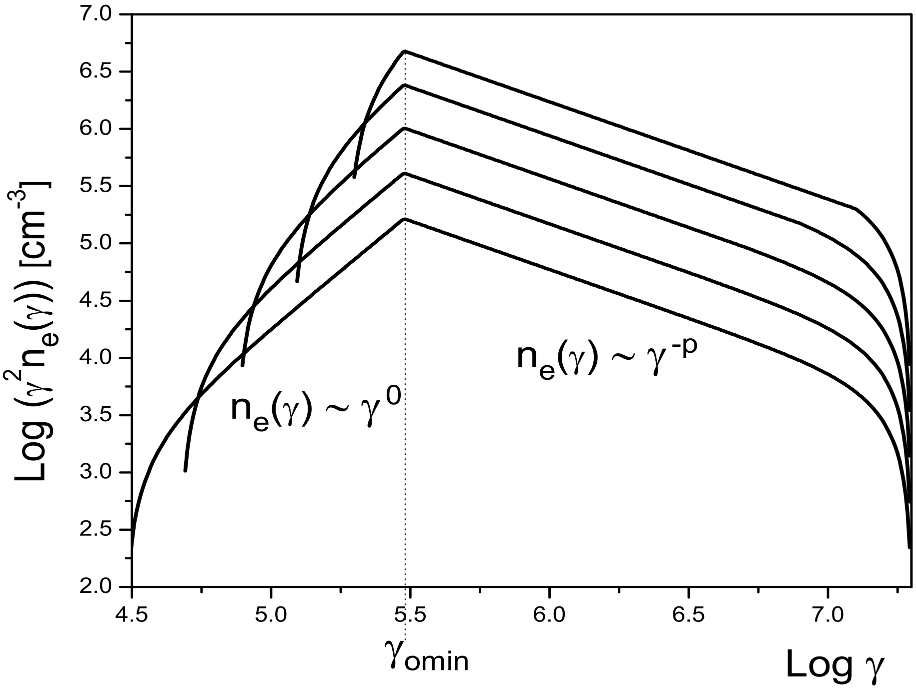

Figure 2.5: Illustration of the evolution of the electron distribution for constant injection and dominant adiabatic losses. The expansion of the source does not modify the power-law index above the initial low-energy cutoff $\gamma_{\rm 0,min}$, whereas below it the distribution becomes approximately flat. The electron number density depends on the radius as $n_e \propto R^{-2}$

The two solutions exhibit the same behavior. The differential electron number density drops with radius as $n_e(\gamma, R) = \frac{N_e(\gamma,R)}{\rm Volume} \propto R^{-2}$, and above the initial low-energy cutoff $\gamma_{\rm 0,min}$ adiabatic losses do not modify the power-law index $n_e(\gamma, t) \propto \gamma^{-p_1}$ (Kardashev 1962). Below $\gamma_{\rm 0,min}$ the resulting distribution is constant with respect to the electron energies, $n_e(\gamma, R) \propto \gamma^0$ (Fig. 2.5). The γ^0-part of the electron population does not show up in the spectrum meaning that the contribution of the injected $\gamma_{\rm 0,min}$ electrons (generating a 1/3-synchrotron wing) remains dominant at low energies (Fig. 2.6). Thus now, in contrast to the synchrotron cooling case, below the injected cutoff the flux is $F_\nu \propto \nu^{1/3}$. For this reason, the classical hard spectrum picture at the TeV range can remain for timescales analogous to the source size. Even though electrons cool adiabatically as the source expands, the hard 1/3-synchrotron slope always appears below the synchrotron frequency related to the initial minimum Lorentz factor

$$\nu_{\min}^{\mathrm{syn}} \propto \gamma_{0,\min}^2 B(R) \propto \frac{1}{t^m}\,. \tag{2.25}$$

Note that any decrease of this break energy occurs due to a decrease of the magnetic field. This is different to the pure synchrotron cooling case, where the corresponding break energy follows the evolution of the minimum electron energy so that $\nu_{\min}^{\mathrm{syn}} \propto 1/t^2$. The same consideration holds for the energy regime where Compton scattering occurs. When we are deep in the KN regime ($b(R)\gamma_{0,\min}^3 > 1$) the energy below which the hard slope remains is, as mentioned above,

$$\nu_{\min}^{C} \propto \gamma_{0,\min}\,. \tag{2.26}$$

It therefore does not move to lower energies though the corresponding synchrotron frequency does (in the pure synchrotron cooling case, obviously, $\nu_{\min}^{C} \propto 1/t^2$). As the source expands and the magnetic field drops, there will be an instant t corresponding to a radius R at which the KN regime no longer applies, and the break Compton frequency becomes

$$\nu_{\min}^{C} \propto B(R)\gamma_{0,\min}^4 \propto \frac{1}{t^m}\,, \tag{2.27}$$

which now moves to lower frequencies with the same rate as the synchrotron one (note that this reveals a very different time-dependence compared to the pure synchrotron cooling case where now $\nu_{\min}^{C} \propto 1/t^4$). However, the peak of the Compton flux still remains close to the initial $\gamma_{0,\min}$ energy (Fig. 2.7 left panel), and in total the decrease of the synchrotron peak flux is much stronger than the decrease in the Compton peak flux (Fig. 2.7 right panel). In general, the dependence of the magnetic field on the radius R has important consequences for the behavior of the system even though the synchrotron losses are not important. The synchrotron peak flux varies as

$$F_\nu^{syn} \propto N_e B(R)^2 \tag{2.28}$$

and as we know from the solution of the kinetic equation that $N_e \propto R$, the variability of the synchrotron luminosity should reflect the magnetic field dependence. The Compton flux, on the other hand, does not necessarily vary quadratically with respect to the synchrotron flux. As discussed above, the drop of the minimum Compton energy (which occurs naturally within the expansion-scenario) reduces the suppression of the cross-section and thereby supports the Compton emission. The variability pattern after "saturation" can therefore approach a quasi-linear dependence (cf. Fig 2.7 right panel). Initially, during the raising phase before the two luminosities reach their maximum, the Compton flux can vary much more strongly, almost more than quadratically, with respect to the synchrotron flux. Moreover, close to saturation the Compton luminosity can exhibit a delay with respect to the synchrotron one as it reaches its maximum at later times compared to the synchrotron luminosity.

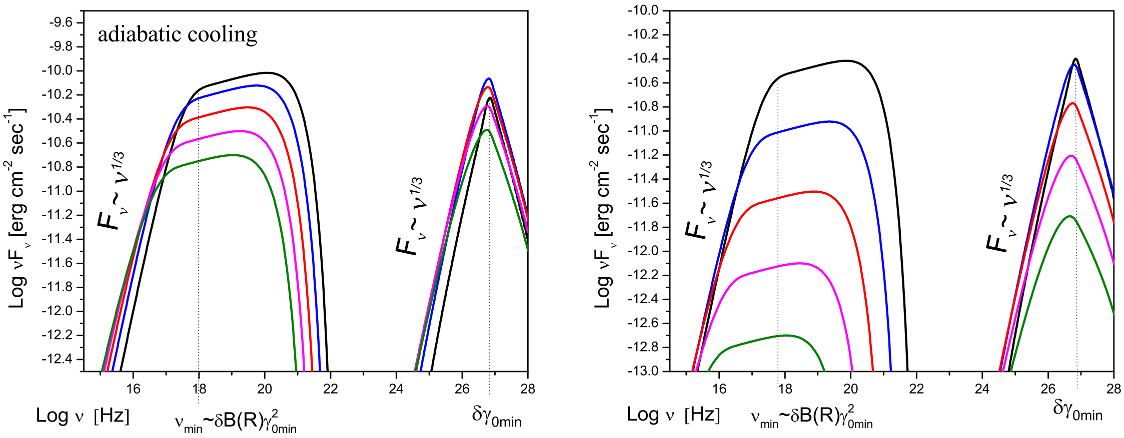

Figure 2.6: (a) Evolution of the observed SSC spectrum with constant injection of a narrow power-law and dominant adiabatic losses. As the source evolves, the synchrotron peak decreases and gets shifted to smaller energies following the decrease of the magnetic field. For the magnetic field, we use an initial value $B_0 = 0.075$ G and we assume that it scales as $B = B_0\ (R_0/R)$ (i.e., $m = 1$). The initial radius is $R_0 = 7.5 \times 10^{14}$ cm, expanding up to $R = 10R_0$ (at $u = 0.1$ c) and corresponding to observed timescales of the order of $t \sim 30/D$ days. The total injected power is $Q \sim 5 \times 10^{41}$ erg/sec. Other parameters used are $\gamma_{\rm min} = 3 \times 10^5$, $\gamma_{\rm max} = 2 \times 10^7$, power law index $p_1 = 2.85$, Doppler factor $D = 25$ and $Q_0 = 1.5 \times 10^{52}$ sec^{-1}. Note that timescales are comparable to the synchrotron cooling case. (b) Same as in left panel but for a different magnetic field scaling, $m = 2$. Other parameters are the same.

The above considerations apply to situations where the expansion of the source completely determines the evolution of the system. In reality, synchrotron losses could modify the electron distribution at high energies, namely for

$$\gamma > \gamma_* = \frac{6\pi m_e c^2}{\sigma_T R B(R)^2} \left(\frac{u}{c}\right) . \tag{2.29}$$

However, as synchrotron losses decrease faster than adiabatic losses, one only needs to ensure that initially $\gamma_* > \gamma_{0,\rm min}$. The change of the electron power index from $-p_1$ to $-p_1 - 1$ due to synchrotron cooling (cooling break) above $\gamma_{0,\rm min}$ would then not disturb the hard 1/3 slope in the TeV range.

2.5 The external Compton scenario

An alternative hypothesis to the SSC scenario concerns the Comptonization of a radiation field external to the electron source. In general, the optical-UV radiation field produced by a standard accretion disk could represent a non-negligible external source of photons to be up-scattered to the VHE γ-ray part of the spectrum. In

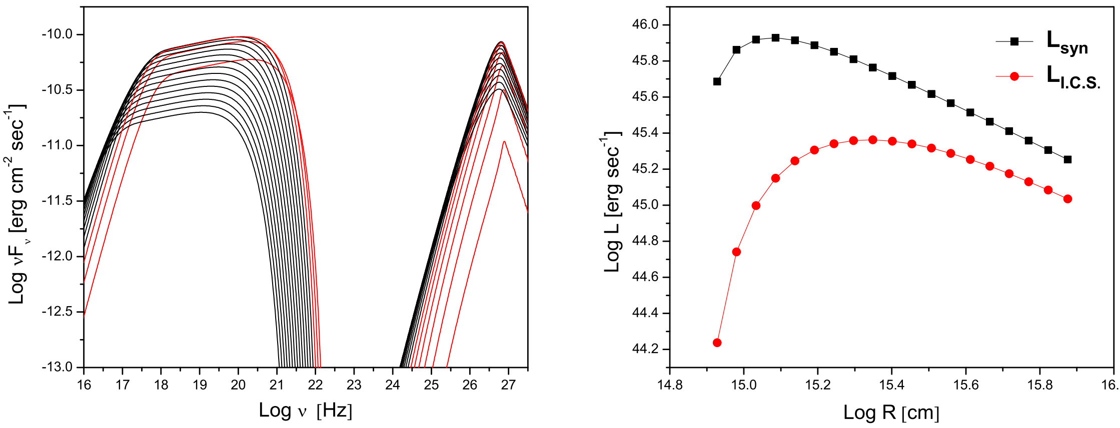

Figure 2.7: (a) Evolution of the SSC spectrum with dominant adiabatic losses (for $B \propto 1/R$, i.e., $m = 1$) from $R_0 = 7.5 \times 10^{14}$ cm to $R = 10R_0$. Whereas the synchrotron peak gets with time significantly shifted to lower energies, the Compton peak can appear almost static. Synchrotron and Compton fluxes are shown until maximum (with red lines) and after (with black lines).(b) Evolution of the corresponding observed luminosities. The Compton flux reaches its maximum at greater radius (i.e., later) compared to the synchrotron one. While during the raising phase the variability pattern approximately shows a quadratic behavior, the correlation becomes almost linear during the declining phase.

the introduction we discussed that this radiation field could be up-scattered either directly by the relativistic electrons of the jet (with target photons coming mostly from the accretion disk, Dermer & Schlickeiser (1993)) or more effectively after being reprocessed/re-scattered by emission line clouds like the broad line region (BLR) (Sikora et al. 1994). In external Compton (EC) scenarios, the geometry of the source and the location of the photon field with respect to the jet are of high importance as they can result in strong boosting or de-boosting effects on the photon energies. Here we explore the possibility of producing a hard TeV spectrum within the EC approach. We consider the BLR case, where the photon field is strongly boosted in the frame of the jet and up-scattered to higher energies.

Let us consider a blob of relativistic electrons that travels with the jet of bulk Lorentz factor Γ along the z-axis. The jet passes through a region assumed to be filled with isotropic and homogeneous photons that obey a Planckian distribution of temperature $T \sim 10^4 - 10^5 K$ (corresponding peak frequency $\nu_d = 2.82kT/h \sim 5 \times 10^{14} - 10^{15}$ Hz). The central disk photon field is then characterized by a special intensity

$$I_\nu^d = \frac{2h\nu^3}{c^2(e^{\frac{h\nu}{kT}} - 1)} \,, \tag{2.30}$$

a fraction $\xi < 1$ of which we assume is isotropized by re-scattering or reprocessing in the BLR (Sikora et al. 2002), so that the spectral energy density of the target photon field is

$$U_\nu^{\rm BLR} = \frac{\xi L_\nu^d}{4\pi c r_{\rm BLR}^2}\,, \tag{2.31}$$

where $L_\nu^d = 4\pi^2 r_d^2 I_\nu^d$ is the spectral luminosity of the disk and where we take $r_d \sim r_s$ for the disk radius.

In order to take anisotropic effects into account, we transform the electron distribution from the comoving blob frame K' to the rest frame K of the external photon field, which in our case coincides with the observer's frame (Georganopoulos et al. 2001). Electrons are assumed to be isotropic in the blob frame K'. In the photon frame K they exhibit a strong dependence on the angle θ, which is the observer's angle. As the up-scattered photons travel inside a cone of opening angle $1/\gamma$, we can make the approximation that they follow the direction of the electrons. The angle between the electron momentum and the bulk velocity of the jet coincides with the observer's angle. The observer practically sees radiation only from electrons that in the photon frame are directed towards him. The observed flux then is

$$F_{\epsilon_\gamma} = \frac{D^3}{d_L^2}\int N_e'(\frac{E}{D})\ W(E,\epsilon_{\rm ph},\epsilon_\gamma)\ n_{\rm ph}(\epsilon_{\rm ph}) dE\ d\epsilon_{\rm ph} \tag{2.32}$$

where $N_e(E)$ denotes the differential number of electrons per energy per solid angle, and $W = E_\gamma \frac{dN}{dtdE_\gamma}$ is the scattered photon spectrum per electron (Blumenthal & Gould 1970). The unprimed quantities refer to the external photon field frame with number density $n_{\rm ph}(\epsilon_{\rm ph})$ and the primed ones to the blob rest frame. Eq. 2.32 is derived analytically in chapter 5.

We show the calculated Compton spectrum for a Maxwellian electron distribution in Fig. 2.8. The resulting TeV slope appears even harder than in the SSC case, with a limiting value of $F_\nu \propto \nu$. Any photon field which is softer than $F_\nu \propto \nu$ will dominate the Compton spectrum at low energies, as in our SSC model case where the up-scattered (synchrotron) photon spectrum follows $F_\nu \propto \nu^{1/3}$. In all other cases, like in the external Compton scenario with a Planckian photon field (that at low energies follows $F_\nu \propto \nu^2$), the characteristic behavior of the Compton cross-section appears, implying that the Compton spectrum at low energies (i.e., below $\sim \gamma_c^2 \epsilon_c$, where γ_c is the electron break frequency in the photon rest frame) is dominated by the contribution from the upscattering of the peak photons with $\epsilon_c \sim 3kT$, yielding a $F_\nu \propto \nu$ dependence.

A similar consideration holds for a narrow (energetic) power-law electron distribution in an expanding source scenario. A hard VHE component $F_\nu \propto \nu$ should then appear below $D\gamma_{0,\rm min}$. The critical energy below which one can see this hard behavior of the Compton flux will not move to lower energies as the external target photon field is quasi-stable, so that the condition for the deep Klein-Nishina regime $\gamma_{0,\rm min}\epsilon_c > 1$ does not change.

2.6 Summary and application to 1ES 0229+200

The observed hard γ-ray spectra of Blazars are difficult to explain within the most popular leptonic synchrotron Compton models. The $n(E) \propto E^{-2}$ shape, that

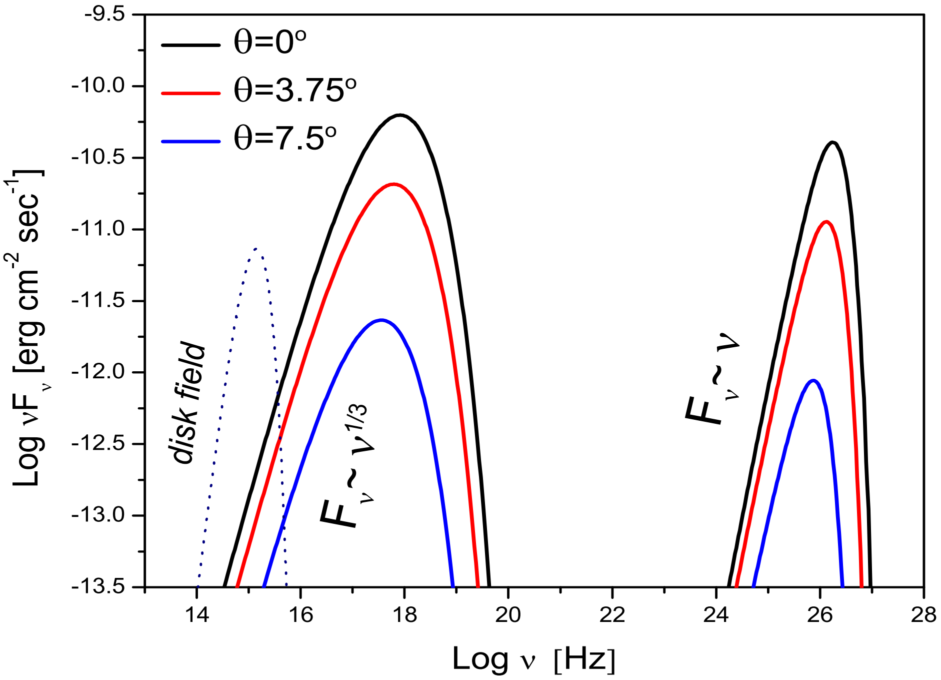

Figure 2.8: External Compton scenario for a Maxwellian-type electron distribution (with $\alpha_p = 0$). The observed spectrum is calculated for different angles θ to the observer. The synchrotron slope follows $F_\nu \propto \nu^{1/3}$. In the TeV range $F_\nu \propto \nu$, i.e., harder than in the SSC case. The dashed line corresponds to the assumed disk spectrum. The bulk Lorentz factor of the jet is $\Gamma = 13$ and the peak energy of the electron distribution is $\gamma_c = 2 \times 10^4$. For the disk photon field a temperature $T = 1.75 \times 10^4$ K is assumed. The relevant radius R_d of the disk is considered to be of the same dimension as the jet (10^{15} cm). The magnetic field is $B = 1$ G and a fraction $\xi = 0.1$ of the disk photons is assumed to be rescattered by the BLR.

the electron energy distribution is expected to quickly develop due to synchrotron cooling, usually results in a $F_\nu \propto \nu^{-1/2}$ radiation spectrum and therefore represents the limiting value of how hard the up-scattered spectrum can be in the TeV range. Moreover, modification due to Klein-Nishina effects can make the up-scattered TeV spectrum steeper and shift the Compton peak to much lower energies than observed.

However, intrinsic source spectra as hard as $F_\nu \propto \nu^{-1/2}$ exist, even when one only corrects for the lowest level of the EBL, most notably in the case of 1ES 1101-232 and 1ES 0229+200 (Aharonian et al., 2006, 2007b). Most likely, the real source spectra are even harder. Investigating the possibility of forming hard VHE Blazar spectra appears therefore particularly important. Methodologically, it seems necessary to first examine the "conventional" radiation and acceleration mechanisms, that have often been successful in interpreting Blazar observations, before adopting very different and often more extreme solutions.

The results of this work show that within a simple homogeneous one-zone SSC approach, a power-law particle distribution with a large low-energy cutoff can in principle produce a hard ($\alpha = 1/3$) – slope in the VHE domain ($F_\nu \propto \nu^\alpha$) by reflecting the characteristic low-energy slope of the single particle synchrotron spectrum (cf. also Katarzyński et al. 2006). As shown in section 2.5, even harder VHE spectra approaching $F_\nu \propto \nu$ ($\alpha = 1$) can be achieved in the external Compton case for a Planckian-type ambient photon field. In total, the hardest possible intrinsic spectrum follows

$$F_\nu^{\rm ICS} \propto \begin{cases} \nu^{1/3} & for\ \ SSC \\ \\ \nu & for\ \ EC \end{cases} \tag{2.33}$$

A power-law electron distribution with a high low-energy cutoff has been used in Tavecchio et al. (2009) to model the emission from 1ES 0229+200 within a stationary SSC approach. In order to avoid the above noted synchrotron cooling problem, an unusually low value for the magnetic field strength was employed, leaving the particle distribution essentially unchanged on the timescales of several years. This goes along with a strong deviation from simple equipartition by several orders of magnitude (i.e., $u_B/u_e \lesssim 10^{-5}$). While it is known from detailed spectral and temporal SSC studies of the prominent γ-ray Blazar Mkn 501 that TeV sources may be out of equipartition (Krawczynski et al. 2002), the SSC modeling of 1ES 0229+200 suggest the hard spectrum sources belong to the more extreme end (within external Compton models values closer to equipartition may be achieved, depending on the external photon field energy density). On the other hand, a large electron energy density (strongly exceeding the magnetic field one) could well facilitate an expansion of the source, and this motivates a time-dependent analysis:

Using a time-dependent SSC model, we have shown that the hard ($\alpha = 1/3$)-VHE slope can be recovered, when adiabatic losses dominate over the synchrotron losses for the low-energy part of the electron distribution (i.e., for Lorentz factors less than the injected $\gamma_{\rm min}$). The main reason for this is, that the resultant electron distribution below $\gamma_{\rm min}$ becomes flat and therefore does not show up in the SSC spectrum. Interestingly, this scheme also allows us to relax the very low magnetic field constraints.

We also examined the relevance of a Maxwellian-like electron distribution that peaks at high electron Lorentz factors $\sim 10^5$. Such a distribution represents a simple time-dependent solution that already takes radiative energy losses into account, and turns out to be capable of successfully reproducing the hard spectra in the TeV range (with limiting values $\alpha = 1/3$ and $\alpha = 1$, respectively). Maxwellian distributions can be the outcome of a stochastic acceleration process balanced by synchrotron or Thomson cooling. Depending on the physical conditions within a source, e.g., if particles undergo additional cooling in an area different from the acceleration one (Saugé & Henri, 2006; Giebels et al., 2007), or if the medium is clumpy supporting a "multi-blob" scenario in which the observed radiation is the result of superposition of regions characterized by different parameters (see chapter 3), the combination of pile-up distributions may allow a suitable interpretation of different type of sources. For the case presented here, they demonstrate a physical way of achieving the high

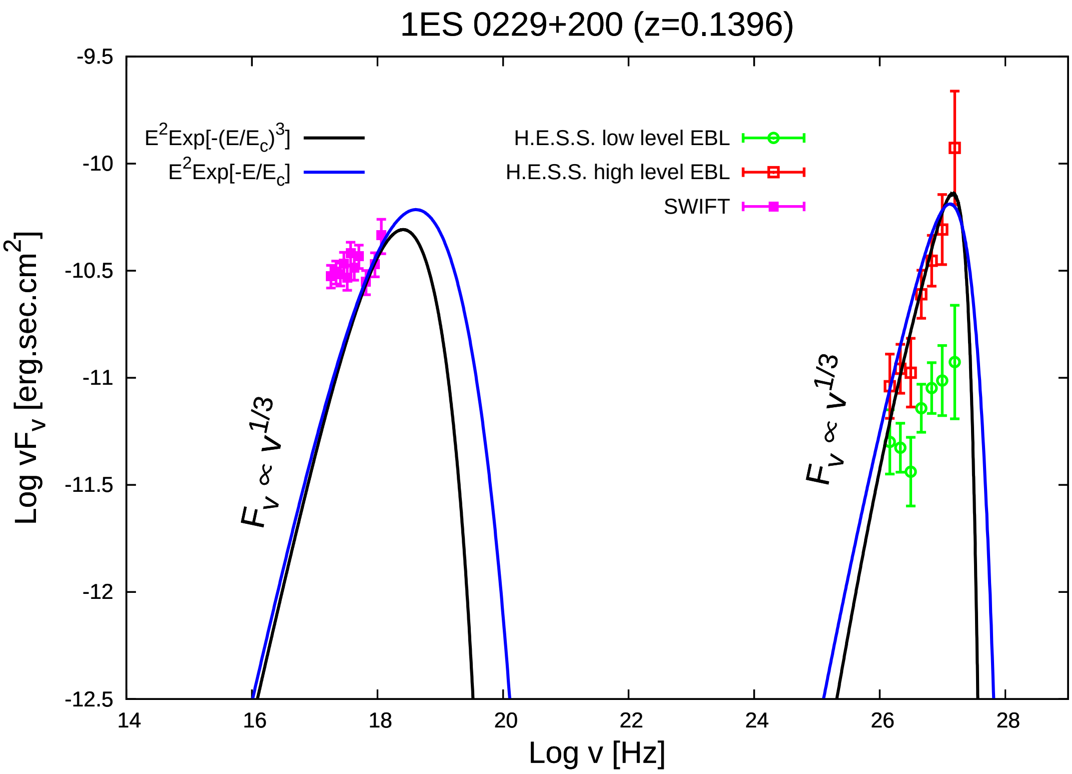

Figure 2.9: The hard spectrum Blazar 1ES 0229+200 at z=0.139 with SED modeled within an SSC approach using Maxwellian-type electron distributions. All parameters used are the same as in Fig.2.4. Data points shown in the figure are from Zacharopoulou et al. (2011), where the intrinsic (de-absorbed) source spectrum has been derived based on the EBL model of Franceschini et al. (2008) with (i) EBL level as in their original paper ("low level EBL") and (ii) (maximum) EBL level scaled up by a factor of 1.6 ("high level EBL").

low-energy cutoffs needed in leptonic synchrotron-Compton models for the hard spectrum sources.

In fig. 2.9 we demonstrate that a narrow electron distribution could provide a satisfactory explanation for the hard TeV component in 1ES 0229+200. In particular we consider a relativistic Maxwell-type distribution within the SSC scenario. The TeV data are corrected using the model of Franceschini et al. (2008) for a low and high EBL flux. Even in a more extreme case (of high EBL flux) the emitted spectrum can be satisfactorily modeled.

Our results illustrate that even within a leptonic synchrotron-Compton approach relatively hard intrinsic TeV source spectra may be encountered under a variety of conditions. While this may be reassuring, the possibility of having such hard source spectra within "standard models" unfortunately constrains the potential of extracting limits on the EBL density based on γ-ray observations of Blazars, one of the hot topics currently discussed in the context of next generation VHE instruments.

Chapter 3

"Leading blob" model in a stochastic acceleration scenario

Evidence for very hard, intrinsic γ-ray source spectra, as inferred after correction for the absorption in the extragalactic background light (EBL), has interesting implications for the acceleration and radiation mechanisms acting in Blazars. A key issue so far has been the dependance of the hardness of the γ-ray spectrum on different existing EBL models. The recent FERMI observations of Mkn 501 now provide additional evidence for the presence of hard intrinsic γ-ray spectra independent of EBL uncertainties. Relativistic Maxwellian-type electron energy distributions that are formed in stochastic acceleration scenarios offer a plausible interpretation for such hard source spectra. In this chapter we show that the combined emission from different components with Maxwellian-type distributions could in principle also account for much softer and broader, power law-like emission spectra. We introduce a "leading blob" scenario, applicable to active flaring episodes, when one (or a few) of these components become distinct over the "background" emission, producing hard spectral features and/or hardening of the observed spectra. We show that this model can explain the peculiar high-energy characteristics of Mkn 501 in 2009, with evidence for flaring activity and strong spectral hardening at the highest γ-ray energies[1].

3.1 The 2009 hard flare of Mkn 501

In the previous chapter we discussed in detail the problems arising in the interpretation of hard spectra within standard leptonic scenarios, i.e., SSC or EC models. The noted small photon indices are generally not easy to achieve, because radiative cooling tends to produce particle energy distributions that are always steeper than $dN_\gamma/dE_\gamma \propto E_\gamma^{-2}$, irrespective of the initially injected particle spectrum. The corresponding TeV photon index would then be $\Gamma \geq 1.5$. Moreover, as the emission from these objects peaks at very high energies, where suppression of the cross-section due to Klein-Nishina effects becomes important, even steeper intrinsic photon spectra

---

[1] The results discussed in this chapter are based on Lefa et al. 2011b

are to be expected.

Nevertheless, sources like the distant Blazars 1ES 1101-232 and 1ES 0229+200 do exhibit hard intrinsic spectra and an interpretation within standard leptonic models is desirable before alternative solutions are adopted. One of the key issues remains the uncertainty of the EBL flux level that affects information on how hard the intrinsic spectra of these sources truly are. The recent *Fermi* detection of variable γ-ray emission from the nearby ($z = 0.034$) TeV Blazar Mkn 501 in 2009 now removes this point of uncertainty, providing strong evidence for hard intrinsic γ-ray source spectra independently of questions related to the EBL. As already indicated in the original FERMI paper on Mkn 501 (Abdo et al. 2011), the spectrum above 10 GeV seems to become much harder during a ($\sim$ 30-day) flaring state. A recent, independent analysis of the same data by Neronov et al. (2011) shows that the (10 GeV-200 GeV) flare spectrum could be as hard as $\Gamma \simeq 1.1$ (see fig. 3.1). While the FERMI collaboration did not comment much on the possible origin of the hard flare spectrum, Neronov et al. (2011) put forward the hypothesis that the hard spectrum flare could result from an electromagnetic cascade in the intergalactic medium, provided that the strength of the intergalactic magnetic field is smaller than 10^{-16} G and that primary γ-rays at 100 TeV energy can escape from the central compact region.

A flare with similar characteristics has also been detected in the Quasar 3C279, at $z = 0.536$, in January 2007 (Aleksić et al. 2011). The MAGIC data corrected for the EBL absorption with the model of Domínguez et al. (2011) reveals a very hard flare with photon index $\Gamma = -0.32 \pm 1.01$ at the range of $150 - 300$GeV. Although the errorbars are large, the low limit for the value of the photon index, $\Gamma \sim 0.69$ is still very small. This detection provides additional evidence for the existence of intrinsically hard spectra during flaring states.

We have shown that in chapter 2 a leptonic context very narrow electron distributions are able to produce hard γ-ray source spectra. These can be either power-law distributions with large value of the minimum cutoff, provided that the magnetic field is sufficiently small to avoid radiative losses (Katarzyński et al., 2006; Tavecchio et al., 2009), or that adiabatic losses dominate at low energies (Lefa et al. 2011). Alternatively, relativistic Maxwell-like distributions formed by a stochastic acceleration process that is balanced by radiative losses can be a viable option (Lefa et al. 2011). In both cases VHE spectra as hard as $E_\gamma dN_\gamma/dE_\gamma \propto E_\gamma^{1/3}$ for the SSC case, and $E_\gamma dN/dE_\gamma \propto E_\gamma$ for EC models can be generated. Maxwellian-type particle distributions are especially attractive for the interpretation of the inferred hard γ-ray source spectra because they resemble to some extent mono-energetic distributions (the hardest possible injection spectra). However, an important question that arises is whether such distributions can also account for softer and broader photon spectra.

Interestingly, the hard high-energy component of Mkn 501 emerged in a flaring state in May 2009, during which little flaring activity was detected at energies below 10 GeV. This suggests that the flare is related to an emission zone that is confined both in space (compact) and time (short, on a timescale of $\sim$ 30 days). Additionally, there is no evidence for a similar, simultaneous increase at X-ray energies (Abdo et al. 2011).

Here we propose a leptonic multi-zone scenario that can accommodate softer emission spectra as well as flaring episodes with hard spectral features, like the one observed in Mkn 501. In this scenario, the observed radiation comes from several emitting regions ("blobs"), in which electrons are accelerated to relativistic energies through stochastic acceleration, forming pile-up distributions. All blobs are considered to have similar parameters except from the characteristic energies ("temperatures") of their Maxwell-like distributions. We note that a "multi-blob" scenario, with power-law components characterized by different trajectories (viewing angles) has also been proposed in the past to account for the TeV emission from non-aligned AGNs (Lenain et al. 2008). What distinguishes the model introduced here is that, due to acceleration and losses, each component is considered to only carry a narrow (pile-up) particle distribution, with broad spectra being formed by an ensemble of components. We show, for example, that in the case where the total energy of the particles is the same for all blobs, the combined emission leads to a spectrum very similar to the one arising from a power-law distribution $dN/dE \propto E^{-p}$ with index $p = 2$. On the other hand, distinct spectral feature can appear once a leading zone dominates. This could happen, for example, if (a) the value of the temperatures changes from blob to blob, and/or if (b) the energetics of a single blob changes.

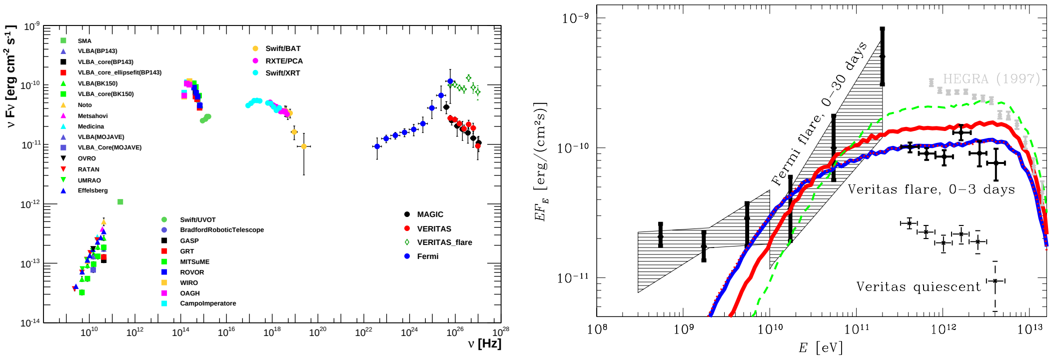

Figure 3.1: (a) Spectral energy distribution for Mrk 501 averaged over all observations taken during the multifrequency campaign performed between 2009 March 15 and 2009 August 1 as presented in Abdo et al. (2011). The TeV data from MAGIC and VERITAS have been corrected for the absorption in the extragalactic background light using the model reported in Franceschini et al. (2008). (b) FERMI spectrum of Mrk 501 for the 30 day period during the flare as analyzed in Neronov et al. (2011). Data points in the TeV band show VERITAS measurements. Model curves show emission from electromagnetic cascade initiated by 100 TeV γ-rays in the intergalactic medium

3.2 A multi-zone scenario

Let us consider N regions in which electrons are stochastically accelerated (e.g., by scattering off randomly moving Alfvén waves) up to energies where acceleration is balanced by synchrotron or inverse Compton (Thomson) losses. Their steady-state energy distributions $n_e(\gamma)$ then take on a relativistic Maxwellian-type form

$$n_i(\gamma) = A_i \gamma^2 e^{-\left(\frac{\gamma}{\gamma_{c_i}}\right)^b} , \tag{3.1}$$

($b \neq 0$; $i = 1, .., N$) with exponential cutoff Lorentz factor

$$\gamma_{c_i} = \left(\frac{bD_0}{\beta_s}\right)^{1/b} (m_e c)^{-1} , \tag{3.2}$$

and normalization factor A_i. Here, β_s refers to energy losses due to synchrotron radiation given by

$$\frac{dp}{dt} = -\beta_s p^2 = -\frac{4}{3}(\sigma_T / m_e^2 c^2) U_B p^2 , \tag{3.3}$$

and the constant D_0 is given by the diffusion coefficient $D_p = \frac{p^2}{3\tau}(\frac{V_A}{c})^2 \equiv D_0 p^{3-b}$, with $V_A = \frac{B}{\sqrt{4\pi\rho}}$ the Alfvén speed and $\tau = \lambda/c \propto p^{b-1}$ (where $b \geq 1$), the mean scattering time (see previous chapter). The shape of the exponential cutoff (characterized by the parameter b) is related to the turbulence wave spectrum $W(k) \propto k^{-q}$ via $b = 3-q$. Note that if the particle distributions would be shaped by inverse Compton cooling in the Klein-Nishina regime, a smoother exponential cutoff is expected (e.g., Stawarz & Petrosian 2008).

For simplicity, we consider below the situation where all blobs have similar properties (e.g., magnetic field strength, linear size, Doppler factor) but different values for the characteristic energy γ_{c_i}. In the case of synchrotron losses and scattering off Alfvén waves, γ_{c_i} depends on the magnetic field and the bulk density of the flow. Thus, the modification in γ_{c_i} that we assume for each blob might be related to a non-homogeneous bulk flow.
The total energy density E_i that the relativistic particles gain through scattering off Alfvén waves is calculated to be

$$E_i = \int_1^\infty \gamma n_i(\gamma) d\gamma m_e c^2 = A_i m_e c^2 \frac{\gamma_{c_i}^4}{b} \Gamma[\frac{4}{b}, \frac{1}{\gamma_{c_i}^b}] , \tag{3.4}$$

where $\Gamma[a, z]$ is the incomplete Γ function. We can now express the normalization factor as a function of the "temperature" (γ_{c_i}) and the energy E_i,

$$A_i = \frac{E_i b}{m_e c^2 \gamma_{c_i}^4 \Gamma[\frac{4}{b}, \frac{1}{\gamma_{c_i}^b}]} , \tag{3.5}$$

which decreases as the cutoff energy increases, with a dependency well approximated by $A_i \propto \gamma_c^{-4}$ for all values of the coefficient b. This is easily seen if we change the lower limit of the previous integration to 0, in which case the result becomes

$$A_i = \frac{4E_i}{m_e c^2 \gamma_{c_i}^4 \Gamma[(4+b)/b]} , \tag{3.6}$$

with $\Gamma[z]$ denoting the Γ function.

The combination of the above electron distributions can lead to power-law-like particle distributions if the temperatures of the different components do not differ significantly and if the components contribute equally to the overall spectra. The power-law index then essentially depends on the amount of energy given to the non-thermal particles in each blob, i.e., on how the total energy E_i of each component scales with temperature (γ_{c_i}). Steep spectra may arise if, e.g., the low temperature components dominate whereas harder spectra may occur if more energy is contained in the high-temperature blobs.

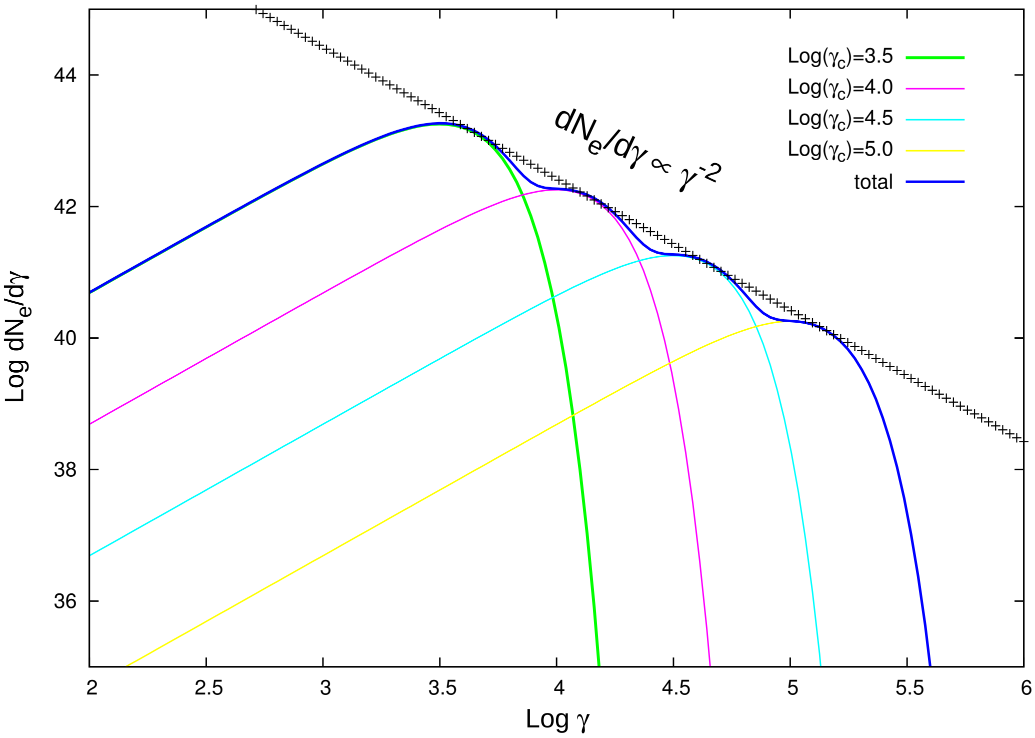

Figure 3.2: The total electron energy distribution from $N = 4$ blobs with different temperatures (γ_c), but the same total energy E_i, tends to establish a power-law $dN_e/d\gamma \propto \gamma^{-2}$ between the minimum and the maximum characteristic energies γ_c. Below $\gamma_{\rm c,min}$, $dN_e/d\gamma \propto \gamma^2$, whereas for $\gamma > \gamma_{\rm c,max}$ one has $dN_e/d\gamma \propto e^{-(\gamma/\gamma_{\rm c,max})^2}$. Here, the exponential cutoff index is $b = 2$, $B = 0.1$ G and $E_i = 2 \times 10^{44}$ erg.

In Fig. 3.2 an example for the total differential electron number is shown assuming $E_i =$ constant. For the plot, an exponential cutoff index $b = 2$ and $N = 4$ have been chosen. The temperatures are equally spaced on logarithmic scale. Then, the total differential energy distribution approximately forms a power-law $dN_e/d\gamma \propto \gamma^{-s}$ with index $s \simeq 2$ between the minimum and maximum temperatures. As discussed above, this "special" value of the power-law index results from the assumption that the blobs have temperatures with equal logarithmic spacing and that all of them have the same total energy, so that the peak $\gamma^2 dN_e/d\gamma$ is the same for each zone. This can be demonstrated more formally by looking for the "envelope", i.e., the mathematical function that describes the curve which is tangent to each of the curves n_i in the

$(dN_e/d\gamma, \gamma_c)$ plane. This function approximates the sum of the energy distribution of the different components as $N \gg 1$ and gives the characteristic behavior of the total distribution between the minimum and the maximum temperature and can be found by solving the set of equations

$$F(\gamma, \gamma_c) = 0, \quad \vartheta_{\gamma_c} F(\gamma, \gamma_c) = 0\,, \tag{3.7}$$

where

$$F(\gamma, \gamma_c) \equiv dN_e/d\gamma - A(\gamma_c)\ \gamma^2 \exp[-(\gamma/\gamma_c)^b]. \tag{3.8}$$

If we assume that the energy in non-thermal particles is the same for each component, we find

$$dN_e/d\gamma = c'(b)\ \gamma^{-2}, \quad \gamma_{\rm c,min} < \gamma < \gamma_{\rm c,max}\,, \tag{3.9}$$

where the parameter $c'(b)$ depends only on the magnetic field

$$c'(b) = 4(4/b)^{4/b} e^{-b/4}/m_e c^2 \Gamma[\frac{4+b}{b}]. \tag{3.10}$$

On the other hand, if particle acceleration to higher energies goes along with a decrease in total energy, e.g., $E \propto 1/\gamma_c$, then steeper power law spectra can appear, i.e., $\frac{dN_e}{d\gamma} \propto \gamma^{-3}$. Note that in all these cases, radiative cooling is already taken into account.

Changing the total energy with γ_{c_i} in each component could also be interpreted as changing the number of contributing blobs as a function of γ_{c_i}, assuming that each component has the same energy. This could be formally accommodated by introducing a statistical weight w_i, so that the overall spectrum is expressed as

$$dN_e/d\gamma = \sum_{i=1}^{i=N} w_i n_i(\gamma)\,. \tag{3.11}$$

Harder spectra may then occur, for example, if more blobs with higher temperatures exist and vice versa. Hence, a conclusion similar to the above can be drawn, once the statistical weights vary with temperature (γ_{c_i}). In a continuous analogue, we may write

$$dN_e/d\gamma = \sum_{i=1}^{i=N} w_i n_i(\gamma) \to \int_{T_1}^{T_N} W(T) n(\gamma, T) dT \tag{3.12}$$

where $W(T)$ is the spectrum the number of components per temperature. Since Maxwellian-type electron distributions behave, to some extent, like mono-energetic ones, the total energy distribution between the minimum and the maximum temperature mimics the spectrum of the number of the blobs $W(T)$ (provided $W(T)$ does not rise quicker than T^2). Thus, in principle a variety of spectra may arise, depending on the choice of $W(T)$. Conversely, observations of extended power law-like energy distributions then impose constraints on how $W(T)$ of a source can vary with temperature.

The SSC spectrum, arising as the sum of the different Maxwell-like distributions of Fig. 3.2, is shown in Fig. 3.3. The synchrotron flux resembles the flux that

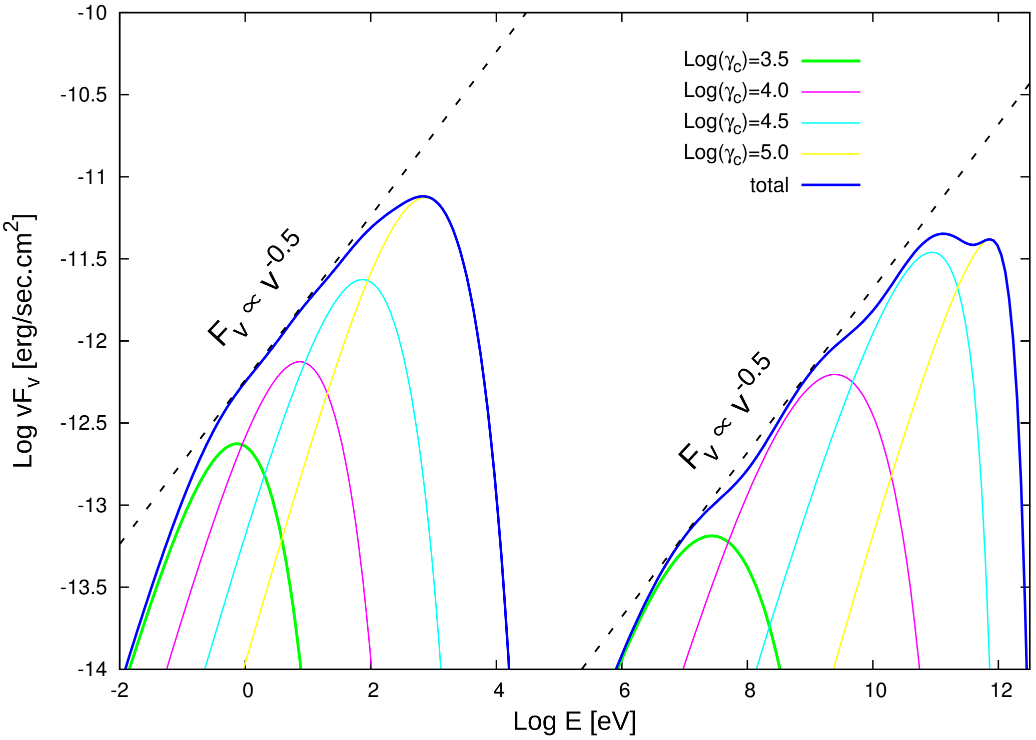

Figure 3.3: Resulting SSC emission from the combination of different components with Maxwellian-like electron distributions. The synchrotron flux exhibits a power-law behavior, $F_\nu \propto \nu^{-1/2}$, approximately between the energies related to the minimum and maximum temperature. The same holds for the Compton flux in the Thomson regime, while in the Klein-Nishina regime the spectrum becomes steeper. Doppler factor $D = 30$ and cutoff index $b = 2$ have been used. Other parameters are $R = 3 \times 10^{14}$ cm, $B = 0.1$ G, $E_i = 2 \times 10^{44}$ erg.

would be emitted by a power-law particle distribution of index 2. Between the frequencies related to the minimum and maximum temperatures, $\nu_{\rm min} \propto B\gamma^2_{\rm c,min}$ and $\nu_{\rm max} \propto B\gamma^2_{\rm c,max}$, it exhibits a $F_\nu \propto \nu^{-1/2}$ behavior. For $\nu < \nu_{\rm min}$ it follows the characteristic $F_\nu \propto \nu^{1/3}$ synchrotron emissivity function, while for $\nu \geq \nu_{\rm max}$ the exponential cutoff becomes smoother (Fritz, 1989; Zirakashvili & Aharonian, 2007)

$$F_\nu \propto \exp\,[-(\frac{\nu}{\nu_{\rm max}})^{\frac{b}{2+b}}]. \tag{3.13}$$

In the present model, the electrons in each blob are considered to only up-scatter their own synchrotron photons and not the ones emitted from the other blobs. The photon fields produced by the other components therefore do not contribute to the emitted Compton spectrum of each blob. In the Thomson regime the up-scattered photon spectrum again approaches a power-law behavior similar to the synchrotron one, i.e. $F_\nu \propto \nu^{-1/2}$. Once Klein-Nishina effects become important, the suppression of the cross-section makes the high-energy spectrum steeper, as expected. In the case of discrete zones, where the particle distributions and synchrotron photons are almost mono-energetic, this happens at (intrinsic) energies greater than

$\gamma_{c_i}(B/B_{cr})\gamma_{c_i}^2 > 1$, where $B_{cr} = m_e^2c^3/(e\hbar)$. Here, $(B/B_{cr})\gamma_{c_i}^2$ is the peak energy of the synchrotron photons emitted by the i-th blob with temperature γ_{c_i}. Below $\nu \propto \gamma_{c,min}^2 B\gamma_{c,min}^2$ the Compton flux reveals the characteristic 1/3-slope, reflecting the low-energy synchrotron spectrum. In the Klein-Nishina regime, the exponential VHE cutoff mimics the shape of the electron cutoff, $F_\nu \propto \exp\left[-(\nu/\nu_{\max})^b\right]$, and is steeper compared to the synchrotron spectrum.

3.3 The origin of hard γ-ray spectrum flares

Once a single component becomes dominant in the overall emission, as naturally expected for a flaring state, hard spectral features can arise. This is more evident in the Compton part of the spectrum as (in the Thomson regime) the separation of the VHE peaks scales as $\sim \gamma_c^4$ and is greater than in the synchrotron case ($\sim \gamma_c^2$). The energetics of such a leading component, which is responsible for an observed flare, could change for a number of reasons: The total (intrinsic) energy offered to the accelerated particles or/and the temperature of the distribution could increase, for example, due to changes in the bulk flow properties or due to an increased injection of seed particles over a finite time. Another possibility concerns an increase in the Doppler factor. Already a slight change of the viewing angle, for example due to the propagation along a curved jet trajectory (e.g., Rieger & Duffy 2004), could lead to the observation of a month-type high-energy flare without an accompanying change of the intrinsic energetics of the components.

The aforementioned possibilities can be applied to explain the ($\sim$ 30 d) high-energy flare of Mkn 501 observed in 2009. Two examples (using four "blobs") are shown in Fig. 3.4: In the left panel, the flaring state is mainly attributed to an increased injection over the duration of the flare (i.e., the normalization of the two components with the highest temperatures is increased by roughly a factor of two). In the right panel, the flaring state is instead modeled by an increase in the Doppler factor (from $D = 30$ to $D = 40$). In both cases, strong spectral hardening becomes apparent above 10 GeV, while the emission below 10 GeV does not vary much. For simplicity, other blob parameters (e.g., magnetic field strength, blob size) have been kept constant to values consistent with the observed variability. This means that both the light-travel time $t_l \sim 2R/(Dc) \leq 0.1$ d and the observed synchrotron cooling time scale

$$t_s \sim 0.3\ (10^5/\gamma_c)(0.1\ \mathrm{G/B})^2(30/\mathrm{D})\ \mathrm{days} \tag{3.14}$$

are much smaller than the observed variability. With these assumptions, modeling of the observed (steeper than $\Gamma = 1.5$) "lower energy" GeV spectrum requires the total energy of each component to drop as the temperature increases (e.g., $E_i \propto \gamma_{c_i}^{-1/4}$). This condition may, however, be modified in more complex models by varying other parameters. For the assumed set of parameters, the synchrotron flux tends to be lower than the observed X-ray flux (Fig. 3.5). This could suggest that the latter is dominated by a different part of the jet, which would be consistent with the fact that little flux variation has been observed in X-rays.

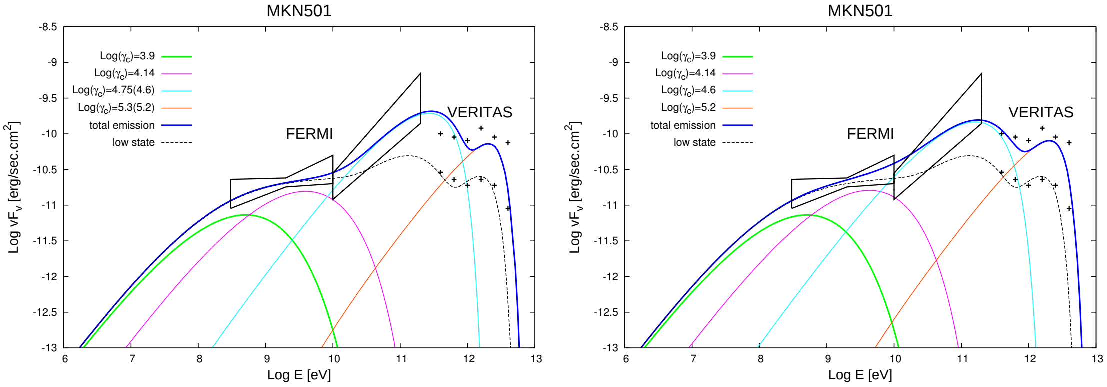

Figure 3.4: (a) SSC emission from the sum of different ($N = 4$) blobs for the "low" (dashed-line) and "flaring state" (blue line) of Mkn 501. The total energy given to the particles scales as $E_i \propto \gamma_{c_i}^{-1/4}$ and for the low state the temperatures are $\log(\gamma_c) = 3.9, 4.15, 4.6$ and 5.2, respectively. The parameters that are kept constant are the magnetic field $B = 0.1$ G, the blob radius $R = 10^{14}$ cm, the cutoff index $b = 3$ and the Doppler factor $D = 30$. For the flaring state, the two blobs with highest temperatures are assumed to be enhanced by a factor of ~ 2 with their temperatures slightly increased. Below 10 GeV, the flux is almost constant with respect to the low state. For data points, see Abdo et al. (2010) and Neronov et al. (2011). (b) Same as in the left panel but assuming the flaring state to occur due to a change of the Doppler factor of the two components with the highest temperatures from $D = 30$ to $D = 40$.

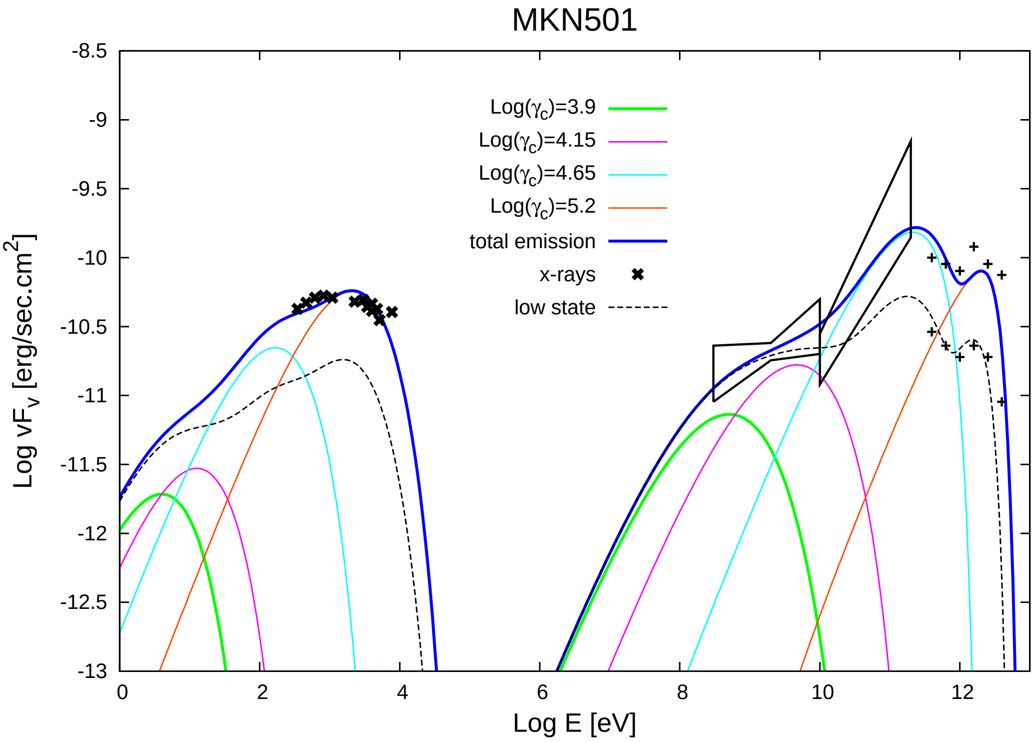

Figure 3.5: Same as figure 3.4 with the synchrotron part of the spectrum included. The X-ray regime is considered to be dominated by emission from a different part of the jet. Thus, during the flare no/little variability at X-ray energies would be observed as long as the synchrotron contribution from the "flaring" components does not exceed the measured X-ray data.

3.4 The case of the Quasar 3C279

A very hard flare was also observed from the Quasar 3C279 ($z = 0.536$) during January 2007 (Aleksić et al. 2011). After correcting for EBL absorption based on the model of Domínguez et al. (2011) the intrinsic photon index is $\Gamma = -0.32 \pm 1.01$, which corresponds to $\nu F_\nu \propto \nu^{1.68 \pm 1.01}$. Such small spectral indices can be achieved with the EC for a very narrow electron distribution, e.g. a relativistic Maxwellian distribution. However, within the errors, the SSC model can as well interpret the observed flare (see fig. 3.6). One main difference with the case of Mkn 501 is the duration of the flare. The flare of 3C279 occurred on much shorter timescales (in the order of a day). As we wish to explain this flare within a stochastic acceleration scenario, we need to ensure that the time needed for the electrons to accelerate remains shorter than the duration of the flare. Indeed, following equation 3.14 we find that, for the parameters chosen here, the cooling timescales for the electrons with maximum energy is shorter than the duration of the flare.

As before we consider that the observed flare is caused by an enhancement of a small blob inside the jet where electrons are stochastically accelerated and form a relativistic Maxwell-type distribution. The rest of the radiation is assumed to come from other components and thus it is not shown in the figure. Both SSC and EC models can reproduce the small photon index within the error. However, the EC scenario approaches better the mean value of the photon index. The synchrotron component is also presented in order to show that there is no violation of the simultaneous low energy data.

3.5 Conclusion

In chapter 2 we have shown that narrow energetic electron distributions, can successfully explain the very hard intrinsic γ-ray spectra that arise in some sources once EBL absorption is taken into account (see also Lefa et al. 2011). In particular, the relativistic Maxwell-type distributions offer an interesting interpretation, as they are steady state solutions of the corresponding Fokker-Planck equation where energy losses are taken into account. However, the sources that exhibit very hard intrinsic spectra are few and a reasonable question that directly arises is whether these distributions have the potential to explain SEDs that appear to be broader.

Here we have demonstrated that the superposition of emission from such distributions could also accommodate much softer and broader γ-ray spectra. To show this, a multi-zone scenario was considered in which particles are accelerated through a stochastic acceleration process balanced by radiative (synchrotron/Thomson) losses in multiple zones characterized by different temperatures (i.e., achievable maximum electron energies). For the parameters examined here, particle escape can be neglected, and the particle distribution in each zone essentially takes a Maxwellian-type shape (however, a combination of power-law distributions with large value of the minimum cutoff would lead to similar conclusions).

Under reasonable conditions and provided the zones are distributed quasi homogeneously in temperature space (using an equal logarithmic spacing), the resultant

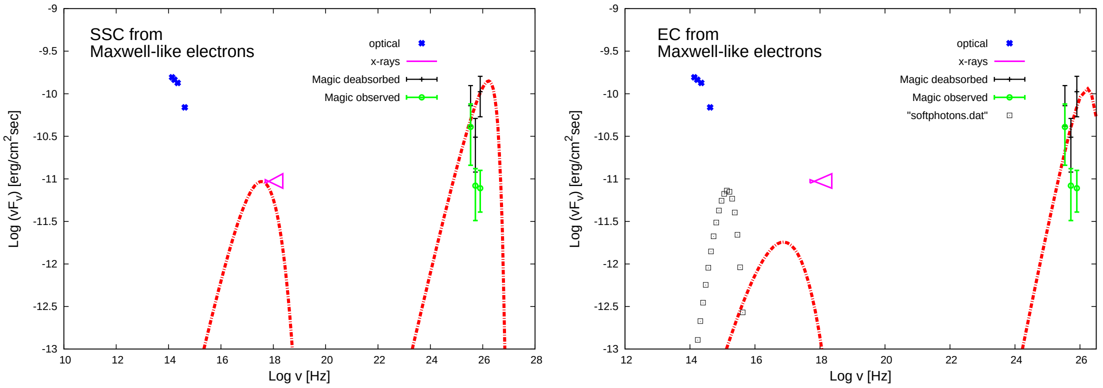

Figure 3.6: (a) SSC emission from Maxwellian electrons for the Quasar 3C279. The parameters used are the electron cutoff energy $\gamma_c = 7 \times 10^4$, the index $\beta = 2$, the magnetic field $B = 0.3G$, the source radius $R = 10^{14} cm$ and the Doppler factor $\delta = 40$. The deviation from equipartition is $Log\,(U_e/U_B) = 4.8$. The (theoretical) slope at the high energy data is somewhat less than 4/3, from 0.8 to 1 approximately. All the data here are have been obtained simultaneously. (b) EC model from maxwellian electrons for 3C279. The parameters used are the electron cutoff energy $\gamma_c = 4. \times 10^4$, the index $\beta = 2$, the magnetic field $B = 0.3G$, the source radius $R = 10^{15} cm$ and the Doppler factor $\delta = 24$. The deviation from equipartition is $Log\,(U_e/U_B) = 2.7$. The (theoretical) slope at the high energy data is a slightly less than 2 (approximately 1.8.)

overall (combined) particle energy spectra then approaches a power-law particle distribution $dN_e/d\gamma \propto \gamma^{-s}$ over the energy range corresponding to the lowest and the highest temperature, with power index s only depending on how the total energy (in non-thermal particles) in each zone scales with temperature (cutoff Lorentz factor γ_c). In the case where all parameters, apart from the temperature, are kept constant (in particular the total energy in each component), the resultant power index approximates $s \to 2$. For similar magnetic fields and Doppler factors, softer/harder power-law γ-ray spectra could arise when the lower/higher temperature components dominate. The larger the number of zones, the smoother the approximation will be. Some peculiar structure may become apparent for a small number of blobs and/or if there is a large gap in temperatures.

In the scheme proposed, the dominance of one (or a few) of the radiating components could lead to a flaring state during which hard spectral features become apparent. This leading component might increase its luminosity for different reasons, e.g., due to a change in the Doppler factor or the injected energy. By using parameters in the typical range of leptonic SSC flare models such a scenario can, as shown above, account for the 2009 flare in Mkn 501 during which a strong hardening of the emission spectra above 100 GeV was observed (Abdo et al., 2011; Neronov et al., 2011). We note that Mkn 501 is indeed known to be a source where detailed temporal and spectral modeling has provided evidence for the contributions of different components (such as a steady X-ray component plus a variable SSC component, see Krawczynski et al. 2002).

While in the case of Mkn 501 an SSC approach has been employed, similar features are to be expected in external Compton scenarios. In the latter case, an even stronger spectral hardening up to $F_\nu \propto \nu$ may occur, while in the SSC case this is limited to $F_\nu \propto \nu^{1/3}$ (Lefa et al. 2011). For example, the VHE flare that was detected in the Quasar 3C279 exhibits a very small value of the photon index, and is more easily explained within an EC model, though the large errors allow for an SSC interpretation.

The suggested scenario for Mkn 501 is of a more phenomenological nature, but it can explain in an interesting way VHE features that are otherwise difficult to interpret within the SSC framework. It will be interesting to check to what extent this also applies to other sources, apart from 3C279 and investigate the parameter space for which the combination of narrow electron distributions can account for broader spectra which more often appear in Blazars.

Chapter 4

On the spectral shape of radiation due to Inverse Compton Scattering close to the maximum cut-off

A large part of the previous chapters we mainly focused on the importance of the low energy cutoff of the emitting electron distribution. The value of the minimum electron energy plays an important role in the interpretation of the hard TeV spectra. In this chapter we explore the high energy cutoff of the electron distribution, which is as well crucial when modeling observed spectra within leptonic models. In particular, the spectral shape of radiation due to ICS is analyzed, in the Thomson and the Klein-Nishina regime, for electron distributions with exponential cutoff. We derive analytical, asymptotic expressions for the spectrum close to the maximum cutoff region. We consider monoenergetic, Planckian and synchrotron photons as target photon fields. These approximations provide a direct link between the distribution of parent electrons and the up-scattered spectrum at the cutoff region[1].

4.1 On ICS and the importance of the maximum cutoff

In the introduction we discussed that the ICS mechanism provides one of the principal γ-ray production processes in astrophysics. The observed spectra of various astrophysical sources is often attributed to the upscattering of low energy photons.

The basic features of the ICS have been analyzed by Jones (1968) and Blumenthal & Gould (1970). The case of anisotropic electrons and/or photons has been studied by Aharonian & Atoyan 1981c; Narginen & Putanen 1993; Brunetti 2000; Sazonov & Sunyaev 2000 and recently by Poutanen & Vurm (2010). The impact of the Klein-Nishina effect on the formation of the energy distribution of electrons was first realized by Blumenthal (1971). Its importance in astrophysics has been discussed in the literature in the context of different non-thermal phenomena, in particular by Aharonian & Ambartsumyan 1985; Zdziarski et al. 1989; Dermer & Atoyan 2002;

---

[1] the results presented in this chapter are based on Lefa et al. 2012

Moderski et al. 2005; Khangulyan & Aharonian 2005; ?; Stawarz et al. 2006; ?.

Generally, the energy spectrum as well as the effects related to ICS are numerically calculated using the exact expression for the Compton cross section. On the other hand, compact, analytical approximations can serve as useful tools for a deeper understanding of the properties of Compton radiation and the implications of the complex numerical calculations. In particular, inferring the energy distribution of the parent particles from the observed spectrum is a much more efficient procedure when analytical approximations are available. For example, a power-law distribution of electrons normally results in power-law photon spectra. If the observed photon index is Γ (in a $dN_\gamma/dE_\gamma \propto E_\gamma^{-\Gamma}$ representation), then we can obtain the power-law index of the electron distribution $dN_e/dE_e \propto E^{-\Gamma_e}$ from the relation $\Gamma_e = 2\Gamma - 1$, for the Thomson regime, and from $\Gamma_e \approx \Gamma - 1$, if the scattering occurs in the Klein-Nishina regime.

This however only applies to the energy interval far from the cutoff (the "main" part of the electron distribution). At the highest (and lowest) energies, there should be a break/cutoff in the electron distribution and in fact, the corresponding break at the radiation spectrum contains a lot of interesting information on the parent electrons. In particular, the peaks in the SED appear at this energy range in the majority of cases, indicating that the source luminosity is mostly radiated at the maximum cutoff. Moreover, as the main, power-law part of the distribution, the shape of the cutoff carries as well important information for the acceleration of the particles and in general the mechanisms acting in the source. Although the shape of the spectrum close to the highest energy cutoff is critical, this topic has not yet been adequately addressed. In this chapter we examine the shape of the Compton spectrum close to the maximum cutoff and we derive analytical formulas that allow to approximate the radiated flux in this specific energy range.

In general, the shape of the electron distribution around the cutoff can be expressed as an exponential, $exp[-(E_e/E_c)^\beta]$. This allows us to describe a quite broad range of distributions, even very sharp, abrupt, step-function like cutoffs for $\beta \gg 1$. Apart from the convenience of such a mathematical description, exponential cutoffs naturally arise in theoretical considerations. For example, in diffusive shock acceleration, power-law particle distributions with exponential cutoff are formed when (synchrotron) energy losses are taken into account (Webb et al. 1984) and the cutoff index is very important for investigating the acceleration mechanism. Analytic solutions show that in the case of Bohm diffusion a simple exponential cutoff $\exp[-E_e/E_c]$ arises, whereas the index approaches $\beta = 2$ if $\dot{E}_e \propto E_e^2$ type energy losses are taken into account, e.g. synchrotron or Thomson losses (see Zirakashvili & Aharonian 2007).

In stochastic acceleration scenarios, where pile-up particle distributions are formed when acceleration is balanced by synchrotron type losses, the shape of the electron cutoff is directly related to the assumed turbulent wave spectrum (Schlickeiser, 1985; Aharonian et al., 1986), e.g. $\beta = 5/3$ for Kolmogorov, $\beta = 3/2$ for Kraicman like or $\beta = 2$ for the hard sphere approximation. Of course, if more complicated energy losses dominate, like in the case of Klein-Nishina losses in radiation-dominated environments, more complex shapes for the electron distribution cutoff may be expected in both stochastic and diffusive shock acceleration scenarios (e.g. Stawarz & Petrosian, 2008; Vannoni et al., 2009)

Nevertheless, it seems reasonable to consider particle distributions that exhibit exponential cutoff in a general form, for investigating and modeling the radiated spectra. In Fritz (1989) and Zirakashvili & Aharonian (2007), the shape of the synchrotron spectrum close to the high energy cutoff has been discussed. They found that when the electron distribution possesses an exponential cutoff of index β, then the radiated synchrotron spectrum exhibits a smoother cutoff, of index $\beta/(\beta+2)$. Apart from the practical importance, this analytic result demonstrates that a δ-function approximation for the synchrotron radiation emissivity does not give the correct result.

Here we examine the corresponding Compton spectrum, in the Thomson and Klein-Nishina regimes, considering different target photon fields so that both SSC and EC scattering can be addressed. We derive analytically the asymptotic behavior of the up-scattered photon distribution close to the cutoff region. We consider a general electron energy distribution of the form

$$\frac{dN_e}{dE_e} = F_e(E_e) = A E_e^{\alpha} e^{-\left(\frac{E_e}{E_c}\right)^{\beta}}, \tag{4.1}$$

where $E_e = \gamma mc^2$ is the electron energy and $E_c = \gamma_c mc^2$ is the cutoff energy. This presentation allows us to consider either a power-law distribution (for $\alpha = -|\alpha|$) with exponential cutoff or a relativistic Maxwell-like distribution (for $\alpha = 2$), that may be formed in stochastic acceleration scenarios. We consider monochromatic, Planckian and synchrotron photons as target photon fields. The resulting IC spectral shape is discussed for the Thomson and the Klein-Nishina regime and we show that is not always identical to the synchrotron spectrum, as is often silently assumed. Finally, we discuss basic features and physical properties of the radiated spectrum.

4.2 Compton spectrum for monochromatic photons

In this section we calculate the asymptotic behavior that the Compton spectrum exhibits close to the maximum cutoff, when monochromatic photons (with isotropic angular distribution) are up-scattered. Let as consider the general function of eq. (4.1), that describes the differential number of electrons. Electrons are considered to be isotropically and homogeneously distributed in space. In this case the spectrum of photons generated per unit time due to ICS is (see e.g. Blumenthal & Gould 1970)

$$d\dot{N}_\gamma/dE_\gamma = \int_0^\infty \int_{E_{emin}}^\infty W(E_e, \epsilon_\gamma, E_\gamma) F_e(E_e) n_{ph}(\epsilon_\gamma) dE_e d\epsilon_\gamma, \tag{4.2}$$

where

$$E_{e\,\mathrm{min}} = \frac{1}{2} E_\gamma \left(1 + \sqrt{1 + \frac{m^2c^4}{\epsilon_\gamma E_\gamma}}\right), \tag{4.3}$$

$$W(E_e, \epsilon_\gamma, E_\gamma) = \frac{8\pi r_e^2 c}{E_e\, \eta} \left[2q \ln q + (1-q)\left(1 + 2q + \frac{\eta^2 q^2}{2\,(1+\eta q)}\right)\right], \tag{4.4}$$

and

$$\eta = \frac{4\,\epsilon_\gamma E_e}{m^2c^4}, \quad q = \frac{E_\gamma}{\eta\,(E_e - E_\gamma)}\,. \tag{4.5}$$

Here the function $W(E_e, \epsilon_\gamma, E_\gamma)$ in eq. (4.4) describes the total scattering probability, taking into account Klein-Nishina effects. The parameter η in eq. (4.5) defines the domain of the scattering. For $\eta \ll 1$ the Thomson regime applies whereas for $\eta \gg 1$ we are in the Klein Nishina regime. In the case of monochromatic photons, the number density is $n_{ph}(\epsilon_\gamma) = n_0\delta(\epsilon_\gamma - \varepsilon_0)$ and we will set n_0 equal to 1 for this case. From now on we set $mc^2 = 1$ throughout the calculations for simplicity, apart from the formulas at which the final results are demonstrated. The case of $\alpha < 0$ will be referred to as power-law distribution, whereas $\alpha = 2$ will be referred to as Maxwellian distribution.

4.2.1 Thomson Regime

In the limiting case of $4\varepsilon_0 E_\mathrm{c} \ll 1$, where all the scatterings occur in the Thomson regime, the photons take a small fraction of the electron energy. Thus, from the previous relation, it follows that $E_\gamma \ll 1/(4\varepsilon_0)$ and the lower limit of the integration becomes

$$E_e \geq E_{e\,\mathrm{min}} \approx \sqrt{E_\gamma/(4\varepsilon_0)} \gg E_\gamma\,. \tag{4.6}$$

Therefore, in this case $\eta q = E_\gamma/E_e \ll 1$ and eq. (4.4) can be written as

$$W(E_e, \varepsilon_0, E_\gamma) = \frac{8\pi r_e^2 c}{E_{\gamma\,\mathrm{max}}}\left[2q\,\ln q + (1-q)\,(1+2q)\right], \tag{4.7}$$

and in this approximation $q = E_\gamma/E_{\gamma\,\mathrm{max}}$, where $E_{\gamma\,\mathrm{max}} = 4\varepsilon_0 E_e^2$. Using the electron distribution of eq. (4.1) and changing the integration variable from E_e to q, the integral of eq. (4.2) for the Compton spectrum becomes

$$d\dot{N}_\gamma/dE_\gamma = \int_0^1 \frac{2\pi r_e^2 c}{2^\alpha}\varepsilon_0^{-\frac{\alpha+1}{2}} E_\gamma^{\frac{\alpha-1}{2}} e^{-\frac{\xi}{q^{\beta/2}}} q^{-\frac{\alpha+1}{2}}\left[2q\,\ln q + (1-q)\,(1+2q)\right] dq, \tag{4.8}$$

where

$$\xi = \left(\frac{E_\gamma}{4\varepsilon_0 E_\mathrm{c}^2}\right)^{\beta/2}. \tag{4.9}$$

We are interested in the behavior of the spectrum near the exponential cutoff, i.e. $E_\gamma >> 4\varepsilon_0 E_c^2$ or $\xi >> 1$. Then the integrant is dominated by values of q very close to unity and in order to perform the above integration it is convenient to change again variables to $\tau = q^{-\beta/2}$ so that

$$d\dot{N}_\gamma/dE_\gamma = \int_1^\infty \frac{2\pi r_e^2 c}{2^\alpha}\,\varepsilon_0^{-\frac{\alpha+1}{2}} E_\gamma^{\frac{\alpha-1}{2}} f(\tau) e^{-\xi\tau} d\tau, \tag{4.10}$$

where

$$f(\tau) = 2\frac{4\tau^{\frac{\alpha-3}{\beta}}\ln\tau - \beta\tau^{\frac{\alpha-1}{\beta}} - \beta\tau^{\frac{\alpha-3}{\beta}} + 2\beta\tau^{\frac{\alpha-5}{\beta}}}{\beta^2\tau}. \tag{4.11}$$

The function $f(\tau)$ is also dominated by values of τ close to unity. Thus, we expand $f(\tau)$ in series around $\tau = 1$. By keeping terms up to first order, the resulting spectrum is

$$\left.\frac{d\dot{N}_\gamma}{dE_\gamma}\right|^T = \frac{8\pi r_e^2 cA(mc^2)^{\alpha+1}}{2^\alpha}\,\frac{\varepsilon_0^{-\frac{\alpha+1}{2}}\,E_\gamma^{\frac{\alpha-1}{2}}}{\beta^2\xi^2}e^{-\xi}\,, \quad \text{for} \quad E_\gamma \gg \frac{\epsilon_\gamma E_c^2}{(mc^2)^2}\,. \tag{4.12}$$

The above expression gives the asymptotic behavior of the Thomson spectrum with exponential accuracy at the cutoff region. When monochromatic photons are up-scattered by electrons with index β, the radiated flux exhibits a smoother cutoff, of index $\beta/2$, i.e.

$$\left.\frac{d\dot{N}_\gamma}{dE_\gamma}\right|^T \propto \exp\left[-\left(\frac{E_\gamma(mc^2)^2}{4\varepsilon_0 E_c^2}\right)^{\beta/2}\right]. \tag{4.13}$$

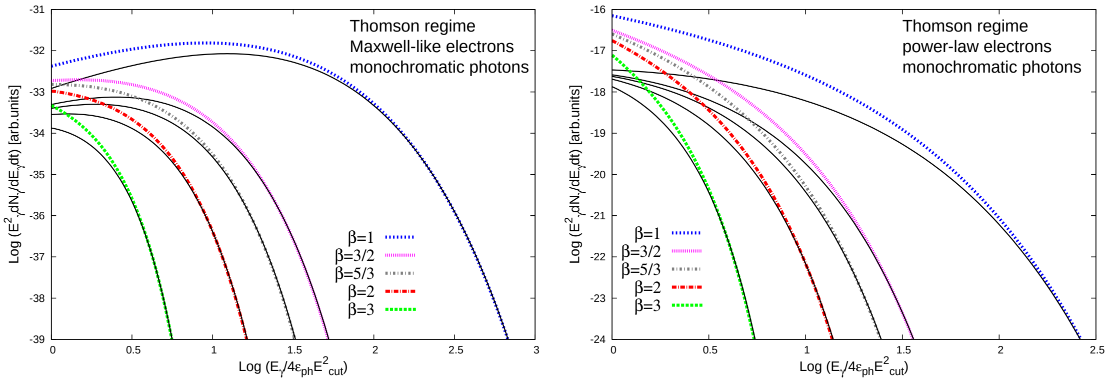

Figure 4.1: (a) Asymptotics in the Thomson regime for monochromatic photons. The $\eta_c = 4\varepsilon_0 E_c$ parameter that defines the domain of scattering for the cutoff electrons is $\eta_c = 0.0004$ ($E_c = 10^2$ and $\varepsilon_0 = 10^{-6}$ both in mc^2 units). For this figure relativistic Maxwell-like electron distributions are used with different shapes of exponential cutoff, β parameter. The exponential cutoff of the up-scattered photon spectrum posses an index of $\beta/2$. As in all figures, black solid lines show the numerical spectrum, whereas colored, dashed lines correspond to the analytic approximation. (b) Same as in the left panel but for power-law electrons. The asymptotics approach the numerical solution only for $E_\gamma \gg 4\varepsilon_0 E_{cut}^2$. For smaller values of E_γ the numerical spectrum is smoother than the approximated one.

As expected, the cutoff in the photon spectrum, $4\varepsilon_0 E_c^2/(mc^2)^2$, corresponds to the maximum photon energy that an electron of energy E_c can radiate in the Thomson regime. We also note that in this case, an abrupt cutoff ($\beta \to \infty$) of the electron energy distribution would correspond to an abrupt cutoff of the photon spectrum. In fig. 4.1 the analytic formula of eq. (4.12) and the full, numerical spectrum are presented, for a Maxwellian and a power-law distribution respectively. Asymptotics are better for $\alpha = 2$. For the power-law distribution the numerical and analytical solution converge for very large values of the parameter ξ. In both cases, very close to the cutoff energy, the numerical spectrum is smoother than the approximated one.

Finally, for a "pure" power-law distribution without exponential cutoff (α negative and $\beta = 0$) one can integrate eq. (4.10) directly to obtain the result

$$\left.\frac{d\dot{N}_\gamma}{dE_\gamma}\right|^{T} = \frac{2\pi r_e^2 c A (mc^2)^3}{2^\alpha} \varepsilon_0^{-\frac{\alpha+1}{2}} E_\gamma^{\frac{\alpha-1}{2}} \frac{4(\alpha^2 - 4\alpha + 11)}{(\alpha-3)^2(\alpha^2 - 6\alpha + 5)}, \quad \text{if} \quad \alpha < 3, \tag{4.14}$$

that demonstrates that in the Thomson regime the radiated spectrum follows a power-law of the form $d\dot{N}_\gamma/dE_\gamma \propto E_\gamma^{\frac{\alpha-1}{2}}$.

4.2.2 Klein-Nishina Regime

When $\eta = 4\varepsilon_0 E_e \gg 1$, photons take almost all the energy of the electrons in one scattering. Then, we may define the parameter $\zeta \equiv 4\varepsilon_0 E_\gamma$ and the low limit of the integration in eq. (4.3) becomes $E_{emin} \approx E_\gamma$. Let us change variables to $x \equiv E_\gamma/E_e$. As $\zeta \gg 1$, we keep only the leading terms

$$\frac{d\dot{N}_\gamma}{dE_\gamma} = \frac{8\pi r^2 c}{\zeta} \int_0^{1-1/\zeta} \left[1 + \frac{x^2}{2(1-x)}\right] F_e(E_\gamma/x) dx. \tag{4.15}$$

Here we have approximated the upper limit of the integration by $1-1/\zeta$ because the integral in eq. (4.15) diverges logarithmically at $x = 1$. For an electron distribution with exponential cutoff the main contribution to the integral comes from regions of x close to unity, so that $1 \ll \frac{x^2}{2(1-x)}$ and we can neglect the first term of the expression in the brackets,

$$\frac{d\dot{N}_\gamma}{dE_\gamma} = \frac{4\pi r^2 c}{\zeta} \left[\int_0^{1-1/\zeta} \frac{x^2 dx}{(1-x)} F_e(\frac{E_\gamma}{x})\right]. \tag{4.16}$$

Now the integral of eq. (4.16) can be calculated for energies close to the cutoff region, $E_\gamma \gg E_c$, leading to a spectrum of the form

$$\left.\frac{d\dot{N}_\gamma}{dE_\gamma}\right|^{KN} = \frac{\pi r^2 c (mc^2)^2}{\varepsilon_0 E_\gamma} \left[\ln\left(\frac{4\varepsilon_0 E_\gamma}{(mc^2)^2}\right) - \ln\beta - \beta \ln(\frac{E_\gamma}{E_c}) - \gamma\right] F_e(E_\gamma), \text{ for } E_\gamma \gg E_c, \tag{4.17}$$

where $\gamma = 0.5772$ is the Euler's constant. In the Klein-Nishina regime where electrons loose almost all their energy in each scattering, the Compton Spectrum practically reflects the behavior of the electron distribution. Thus, in this case, the exponential cutoff maintains the index β and is steeper than in the Thomson case

$$\left.\frac{d\dot{N}_\gamma}{dE_\gamma}\right|^{KN} \propto \exp\left[-\left(\frac{E_\gamma}{E_c}\right)^\beta\right]. \tag{4.18}$$

As before, the photon cutoff energy corresponds to the maximum photon energy that electrons of energy E_c radiate in the Klein-Nishina regime. Moreover, an abrupt electron distribution cutoff would result in an abrupt photon spectrum cutoff. The asymptotics of eq. (4.17) are presented in fig. 4.2; as can be seen, they provide a good approximation just after the peak of the SED.

The fact that the exponential index becomes $\beta/2$ and β in the Thomson and Klein-Nishina regime, respectively, indicates that using a δ-function approximation for the cross section provides a correct result for the calculated spectrum in these two regimes (for an extended discussion on the applicability of δ-function approximation see Coppi & Blandford (1990)). Obviously this is not true for values of η_c close to unity (see fig. 6.3), where $\eta_c = 4\varepsilon_0 E_c$ refers to the electron cutoff energy. As we are interested in the highest energy part of the spectrum, the approximation in the Klein-Nishina regime is satisfactory even for values of η_c that do not significantly exceed unity. This happens because since $\eta_c > 1$ for the electron cutoff energy it holds for all the energies $E_e > E_c$ that actually form the shape of the exponential cutoff. On the contrary, for the Thomson regime one needs all the radiated photons above the cutoff to be emitted at this regime, which indicates rather small values of η for the approximation to be good, especially for small β factors.

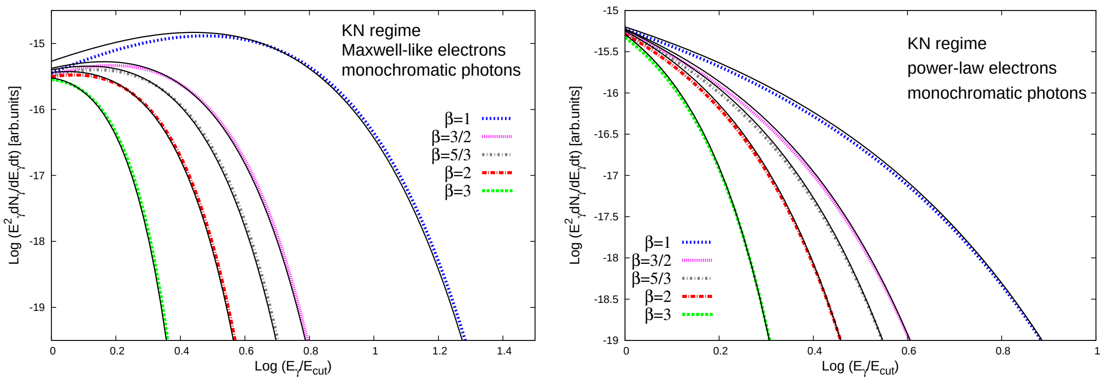

Figure 4.2: (a) Asymptotics in the Klein-Nishina regime for monochromatic photons and Maxwell-like electrons. The η_c parameter that defines the domain of the scattering is $\eta_c = 400$ ($E_c = 10^6$ and $\varepsilon_0 = 10^{-4}$ both in mc^2 units). The photon spectrum exhibits a cutoff index β, same as the electron distribution. The analytical approximation is in very good agreement with the numerical spectrum just after the peak of the SED. (b) Same as in the left panel but for a power-law electron distribution.

A similar calculation can be performed for a "pure" power-law electron distribution, with $\beta = 0$. If we rewrite the second term of eq. (4.15) in the form

$$\int_0^{1-1/\zeta} \frac{x^2}{1-x} x^{-a} F_e(E_\gamma/x) = F_e(E_\gamma) \int_0^{1-1/\zeta} \frac{x^2 dx}{1-x} + F_e(E_\gamma) \int_0^1 \frac{(x^{2+\alpha}-1)dx}{1-x}, \tag{4.19}$$

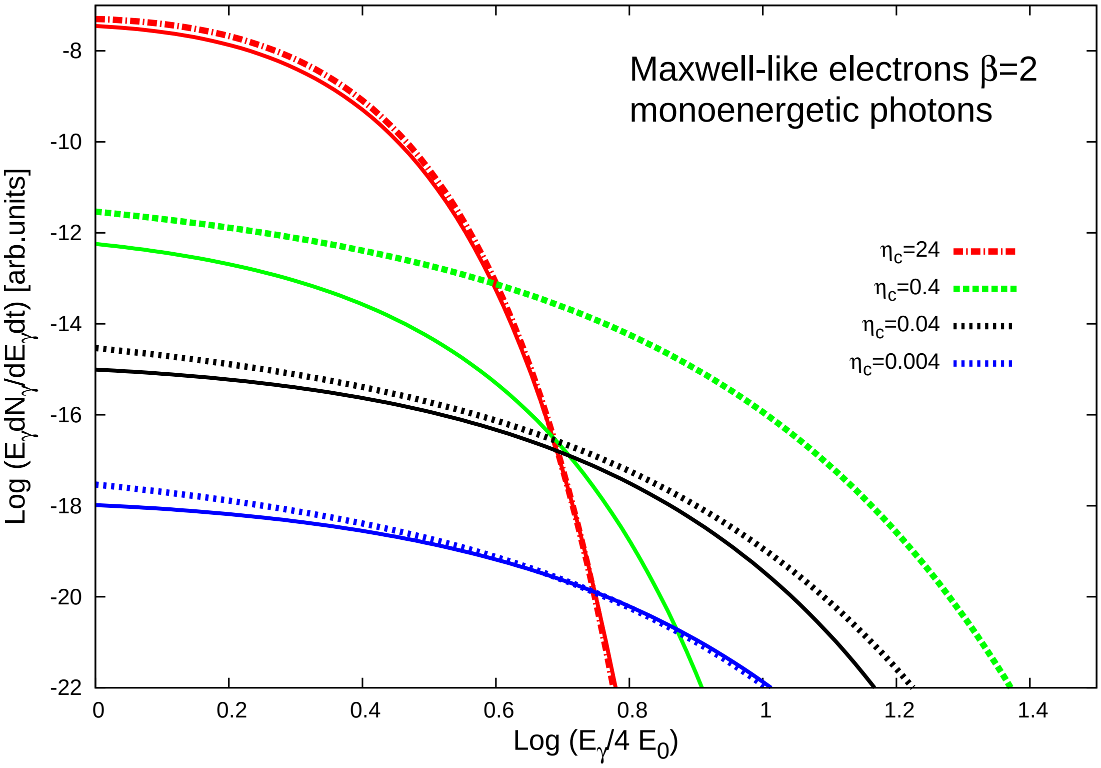

Figure 4.3: Asymptotics for a Maxwell-like distribution with $\beta = 2$ for different values of the parameter η_c that defines the domain of the scattering for electrons with energy E_c. In the Klein-Nishina regime the approximation is good even for not very large values of η_c. In the Thomson regime the approximation becomes acceptable for $\eta \sim 0.004 \ll 1$. In the intermediate domain the exact numerical spectrum decays more sharply than the approximated one, indicating that while $4\varepsilon_0 E_c < 1$, part of the electrons with $E_e > E_c$ already up-scatter the soft photon in the Klein-Nishina regime.

we can perform the above integration resulting in an emitted spectrum of the form

$$\left.\frac{d\dot{N}_\gamma}{dE_\gamma}\right|^{KN} = \frac{\pi r^2 c A (mc^2)^2}{\varepsilon_0} E_\gamma^{-\alpha-1}\left[\ln\left(\frac{4\varepsilon_0 E_\gamma}{(mc^2)^2}\right) - \frac{3\alpha^2+15\alpha+14}{4\alpha(\alpha+1)(\alpha+2)} - \gamma - \Psi(\alpha)\right], \tag{4.20}$$

where $\Psi(\alpha)$ is the digamma function defined as the logarithmic derivative of the Γ function ($\Psi(\alpha) = \Gamma'(\alpha)/\Gamma(\alpha)$). This formula shows that the emitted Compton spectrum is much steeper in this than in the Thomson regime due to the suppression of the cross-section. The functional dependance of eq. (4.20)

$$\left.\frac{d\dot{N}_\gamma}{dE_\gamma}\right|^{KN} \propto E^{-\alpha-1} \tag{4.21}$$

has been obtained in Blumenthal & Gould (1970) (see e.g. their eq. (2.87)), and Aharonian & Atoyan (1981c) (see their eq. (32)). These formulas differ in the term related to the power-law index α, due to the different approach used for the calculation of the asymptotics. This difference is negligible.

4.3 Compton spectrum for a broad photon distribution

Once we have calculated the radiated spectrum for monochromatic photons, we can examine the behavior of the Compton spectrum for various photon fields. The case of monochromatic photons is important for understanding the scattering mechanism and a necessary step for further calculations. However, in nature the photon fields are usually broader than the monochromatic one, except if we deal with emission lines. Here we will consider a Planckian photon distribution which is often the case in external Compton scenarios and we will examine as well the case of synchrotron photons from the same parent electron distribution, that are used as the target photon field in synchrotron self-Compton models.

4.3.1 Planckian photon field

Let as assume a Planckian distribution for the photon field so that the differential number density is given by

$$n_{ph}(\epsilon_\gamma) = \frac{1}{\pi^2 \hbar^3 c^3} \frac{\epsilon_\gamma^2}{e^{\epsilon_\gamma/kT} - 1}. \tag{4.22}$$

For the Thomson regime, where now we demand $4kTE_e \ll 1$, we can use the Wien limit ($\epsilon_\gamma \gg kT$) at which

$$n_{ph}(\epsilon_\gamma) = \frac{1}{\pi^2 \hbar^3 c^3} \epsilon_\gamma^2 e^{-\epsilon_\gamma/kT}. \tag{4.23}$$

This is acceptable as the asymptotic behavior of the Compton spectrum at high energies is mostly defined by the soft photons with energy around and greater than kT.

In that case the integration of the spectrum eq. (4.12) over the photon energies can be evaluated by the saddle point method of integration. After replacing ε_0 with ϵ_γ in eq. (4.12), the integral is written as

$$\left.\frac{d\dot{N}_\gamma}{dE_\gamma}\right|_{BB}^{T} = \int_0^\infty \left.\frac{d\dot{N}_\gamma}{dE_\gamma}\right|^{T} n_{ph}(\epsilon_\gamma) d\epsilon_\gamma = \int_0^\infty g(E_\gamma, \epsilon_\gamma) e^{S(E_\gamma, \epsilon_\gamma)} d\epsilon_\gamma, \tag{4.24}$$

where

$$g(E_\gamma, \epsilon_\gamma) = \frac{8\pi r_e^2 A}{2^\alpha \pi^2 \hbar^3 c^2} \frac{E_\gamma^{\frac{\alpha-1}{2}} \epsilon_\gamma^{\frac{3-\alpha}{2}}}{\beta^2 \xi^2} \tag{4.25}$$

and

$$S(E_\gamma, \epsilon_\gamma) = -\left(\frac{E_\gamma}{4\epsilon_\gamma E_{\rm c}^2}\right)^{\beta/2} - \frac{\epsilon_\gamma}{kT}. \tag{4.26}$$

Here BB stands for black body. Let as define the parameter ξ_1 that is related to the cutoff of the up-scattered photon spectrum for the case of monochromatic photons, if we replace ϵ_γ with kT

$$\xi_1 \equiv \frac{E_\gamma}{4kTE_c^2}. \tag{4.27}$$

This parameter simply describes the outgoing photon energy normalized to the maximum energy which E_c electrons radiate when they up-scatter photons of energy kT. One can use the saddle point method for the above integration because the integral at large energies ($\xi_1 \gg 1$) is determined by the soft photon energy interval around the energy x_0 which optimizes the function $S(E_\gamma, \epsilon_\gamma)$. The saddle point x_0 is at

$$x_0 = \frac{\beta}{2}\left(\frac{2\xi_1}{\beta}\right)^{\frac{\beta}{\beta+2}} kT. \tag{4.28}$$

Then, the Thomson spectrum for a Planckian photon distribution is calculated to be $d\dot{N}_\gamma/dE_\gamma = g(E_\gamma, \epsilon_*)\ \exp[-S(E_\gamma, x_0)]\sqrt{2\pi/-S''(E_\gamma, x_0)}$ where S'' the second derivative of S at the saddle point x_0. After rearranging the terms, we retrieve the following expression

$$\left.\frac{d\dot{N}_\gamma}{dE_\gamma}\right|_{BB}^{T} = \frac{4\pi r_e^2 A (kT)^{\frac{5}{2}}(mc^2)^{\alpha+1}}{2^\alpha \pi^2 \hbar^3 c^2}\sqrt{\frac{\pi}{\beta+2}}\, x_0^{-\frac{\alpha}{2}} E_\gamma^{\frac{\alpha-1}{2}} e^{-\frac{\beta+2}{2}\left(\frac{2\xi_1}{\beta}\right)^{\frac{\beta}{\beta+2}}}, \text{ for } E_\gamma \gg \frac{4kTE_c^2}{(mc^2)^2}, \tag{4.29}$$

Therefore, when the target photon field is a black-body, the shape of the cutoff is affected by the soft photon distribution and the exponential cutoff in the Thomson spectrum is smoother in comparison to the monochromatic photons case. The index now becomes $\beta/(\beta+2)$ as

$$\left.\frac{d\dot{N}_\gamma}{dE_\gamma}\right|_{BB}^{T} \propto \exp\left[-\frac{\beta+2}{2}\left(\frac{2}{\beta}\frac{E_\gamma (mc^2)^2}{4kTE_c^2}\right)^{\frac{\beta}{\beta+2}}\right]. \tag{4.30}$$

This exponential cutoff is always smooth (less than unity) and it becomes unity in the case of an abrupt electron distribution cutoff, as $\lim_{\beta\to\infty}\beta/(\beta+2) = 1$. Interestingly, the Thomson spectrum for Planckian photons at high energies exhibits the same exponential cutoff shape as the synchrotron spectrum. This is the only case where the two components of the spectrum show the same behavior for arbitrary index β. For the Maxwellian and power-law type distributions of electrons, eq. 4.30 is presented in fig. 4.4.

In the Klein-Nishina regime the shape of the exponential cutoff does not depend on the up-scattered photon distribution but, as mentioned above, preserves the electron index β. Integration of eq. (4.17) over photon energies (after replacing ε_0 with ϵ_γ) requires the calculation of the following integrals

$$\int_0^\infty \frac{1}{\epsilon_\gamma} n(\epsilon_\gamma) d\epsilon_\gamma = \frac{(kT)^2}{6\hbar c^3}, \tag{4.31}$$

$$\int_0^\infty \frac{1}{\epsilon_\gamma} n(\epsilon_\gamma) \ln(4\epsilon_\gamma E_\gamma) d\epsilon_\gamma = \frac{(kT)^2}{6\hbar c^3}\left(\ln(4kTE_\gamma) - 0.1472\right). \tag{4.32}$$

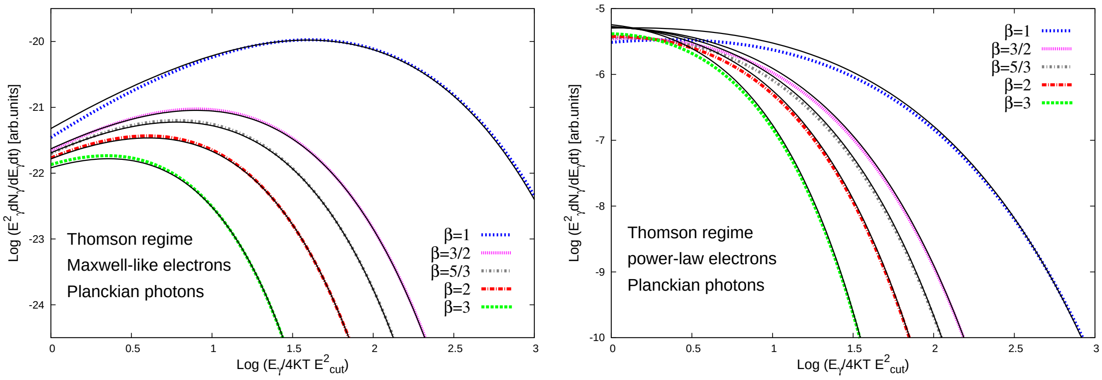

Figure 4.4: Asymptotic behavior of the Thomson spectrum at the cutoff region, for Maxwell-like (left panel) and power-law electrons (right panel) up-scattering Planckian photons. Parameters used are $E_c = 10^2$, $KT = 10^{-6}$ so that $\eta_c = 4kTE_c = 0.0004 \ll 1$. The exponential cutoff possesses an index $\beta/(\beta+2)$.

Then, the asymptotic behavior of the up-scattered spectrum close to the cutoff follows the formula

$$\left.\frac{d\dot{N}_\gamma}{dE_\gamma}\right|^{KN}_{BB} = \frac{\pi^2 r_e^2 A(KT)^2(mc^2)^2}{\hbar^3 c^2}\frac{F_e(E_\gamma)}{E_\gamma}\left[\ln\frac{4KTE_\gamma}{(mc^2)^2} - \ln\beta - \beta\ln\frac{E_\gamma}{E_c} - 0.724\right], \quad E_\gamma \gg E_c. \tag{4.33}$$

Thus, in the Klein-Nishina regime the cutoff is always much sharper than in the Thomson regime. The spectra for Maxwellian and power-law distributions of electrons are shown in fig. 4.5. For values of the index $\beta = 1, 2, 3$, the corresponding shape in Thomson regime becomes 1/3, 1/2 and 3/5 respectively, always less than unity. For an abrupt cutoff ($\beta \to \infty$), the Klein-Nishina spectrum appears sharp as well, while the Thomson spectrum exhibits a simple exponential cutoff.

4.3.2 Synchrotron photon field

In synchrotron self-Compton models, the electrons up-scatter the photon which they produced via synchrotron radiation. In contrast to external Compton models, we do not have an analytic expression for the target photon density. However, we can use an approximation for the synchrotron spectrum at energies around the synchrotron cutoff, i.e. for $\epsilon_\gamma \geq bE_c^2$, given that the main contribution to the scattering process at high energies comes from this energy range. Here $b = 3qBh/4\pi mc(mc^2)^2$.

4.3.3 Synchrotron spectrum

In the case of chaotic magnetic fields, the synchrotron emissivity of an electron with energy E_e is described by the equation

$$\frac{d\dot{N}_\gamma}{d\epsilon_\gamma} = \frac{\sqrt{3}q^3B}{mc^2h\epsilon_\gamma}\tilde{G}\left(\frac{\epsilon_\gamma}{\epsilon_s}\right), \tag{4.34}$$

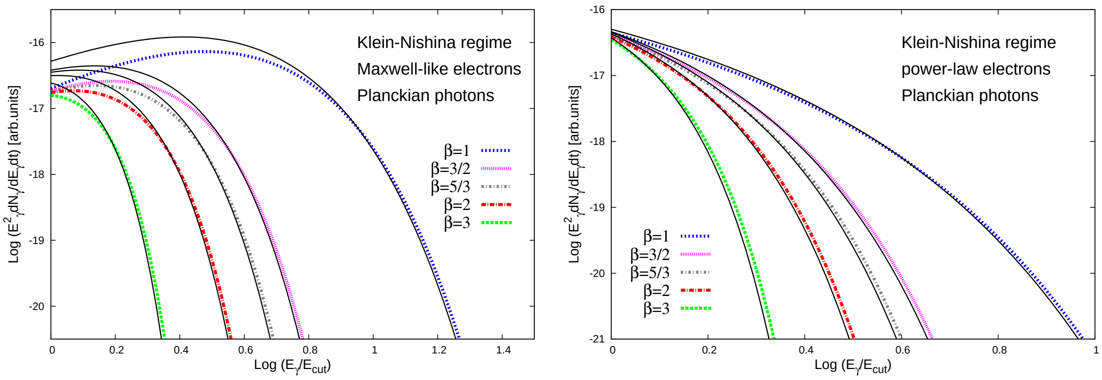

Figure 4.5: Compton spectrum in the Klein-Nishina regime for Maxwellian electrons (left panel) and Planckian photons. $E_c = 10^6$, $K_e = 10^{-4}$ and $\eta_c = 4kTE_c = 400 \gg 1$. The spectrum shows a cutoff of index β, same as the electron energy distribution. At the right panel the case for power-law electrons upscattering Planckian photons is shown.

where

$$\epsilon_s = b\gamma^2 = \frac{3qBh}{4\pi mc}\frac{E_e^2}{(mc^2)^2} \tag{4.35}$$

is the "critical" energy for synchrotron emission. The synchrotron power $\epsilon_\gamma \dot{N}_\gamma / d\epsilon_\gamma$ peaks at $0.29\epsilon_s$ (e.g. Rybicki & Lightmann 1979). The function $\tilde{G}(y)$ can be well approximated, with an accuracy better than 0.2% over the entire range of variable y, by the formula (Aharonian et al. 2010)

$$\tilde{G}(y) = G(y)e^{-y} = \frac{1.808y^{1/3}}{\sqrt{1+3.4y^{2/3}}}\frac{1+2.21y^{2/3}+0.347y^{4/3}}{1+1.353y^{2/3}+0.217y^{4/3}}\, e^{-y}. \tag{4.36}$$

For large $y \gg 1$, the function $G(y)$ is approximately $G(y) \approx \sqrt{\pi/2}$. The parameter ξ_2 that defines the synchrotron photon energy normalized to the energy ϵ_s (eq. 4.35) for the electrons with energy E_c is

$$\xi_2 = \epsilon_\gamma/\epsilon_0 = \frac{\epsilon_\gamma}{bE_c^2}. \tag{4.37}$$

In order to calculate the emitted synchrotron spectrum, we need to integrate eq. (4.34) over the electron distribution given by eq. (4.1). By changing variables from E_e to $y = \epsilon_\gamma/\epsilon_s$, we find

$$\left.\frac{d\dot{N}_\gamma}{d\epsilon_\gamma}\right|_{SYN} = \int_0^\infty \frac{d\dot{N}_\gamma}{d\epsilon_\gamma}F_e(E_e)dE_e = \frac{\sqrt{3}q^3BA}{2mc^2h\epsilon_\gamma}(\frac{\epsilon_\gamma}{b})^{\frac{\alpha+1}{2}}\int_0^\infty y^{-\frac{\alpha}{2}-1}G(y)e^{-y-(\frac{\xi_2}{y})^{\beta/2}}dy. \tag{4.38}$$

For $\xi_2 > 1$ the integration over y reveals a saddle point at

$$y_0 = \frac{\beta}{2}\left(\frac{2\xi_2}{\beta}\right)^{\frac{\beta}{\beta+2}}, \tag{4.39}$$

so that finally the emitted synchrotron spectrum can be expressed as

$$\left.\frac{\epsilon_\gamma d\dot{N}_\gamma}{d\epsilon_\gamma}\right|_{SYN} = \frac{\sqrt{3}q^3B}{mc^2h}\sqrt{\frac{\pi}{\beta+2}}A\left(\frac{\epsilon_\gamma}{b}\right)^{\frac{\alpha+1}{2}} y_0^{-\frac{\alpha}{2}-1}G(y_0)e^{-\frac{2+\beta}{\beta}y_0}. \tag{4.40}$$

This formula indicates the shape of the exponential cutoff for synchrotron radiation

$$\left.\frac{\epsilon_\gamma d\dot{N}_\gamma}{d\epsilon_\gamma}\right|_{SYN} \propto \exp\left[-\frac{\beta+2}{2}\left(\frac{2\epsilon_\gamma}{\beta\epsilon_0}\right)^{\beta/(\beta+2)}\right]. \tag{4.41}$$

We note that the $\beta/(\beta+2)$ index for the synchrotron exponential cutoff has already been found in Fritz (1989) and Zirakashvili & Aharonian (2007). With the above calculations we can moreover estimate critical aspects of the emitted spectrum, and in particular the cutoff energy of the emitted synchrotron spectrum (see section 4). The above equations correspond to optically thin synchrotron sources when the synchrotron-self absorption can be ignored. This could be the case of even very compact and highly magnetized sources, as long as the synchrotron cutoff appears at optical and higher frequencies. One should also mention that the synchrotron spectrum is sensitive to inhomogeneities of the magnetic field (e.g. Katz-Stone & Rudnick, 1994; Eilek et al., 1997). Obviously, the fluctuations of the magnetic field should have an impact on the synchrotron spectrum, namely they will make the cutoff smoother and shifted towards higher frequencies (see e.g. Eilek & Arendt, 1996). In this regard, the ICS γ-ray spectrum is free of uncertainties related to the magnetic field distribution, except for realization of the SSC scenario in the Thomson limit.

Last, we should mention that using a δ-function approximation for the synchrotron emissivity would result to an exponential cutoff of index $\beta/2$, whereas the correct value is $\beta/(2+\beta)$. The synchrotron asymptotics are presented in fig. 4.6, for Maxwellian and power-law electron distributions. For comparison, the Thomson spectrum for Planckian photons is also shown.

4.3.4 SSC spectrum

Now we can integrate the Compton spectrum for monochromatic photons over the photon energies for the synchrotron distribution. The differential photon number density (for a spherical source) is

$$n_{ph}(\epsilon_\gamma) = \frac{3}{4\pi R^3}\frac{R}{c}\frac{d\dot{N}_\gamma}{d\epsilon_\gamma}, \tag{4.42}$$

where R is the source radius. Let us first perform the calculations for the Thomson regime described by eq. (4.12) with $\varepsilon_0 \to \epsilon_\gamma$. In that case the exponential factor in the integrant is $\exp[-S]$, where $S = \xi + (2-\beta)y_0/\beta$. The function S has extremum at the saddle point

$$z_0 = \frac{\beta}{2}\left(\frac{2}{\beta}\frac{E_\gamma}{E_0}\right)^{\frac{\beta+2}{\beta+4}}\epsilon_0, \tag{4.43}$$

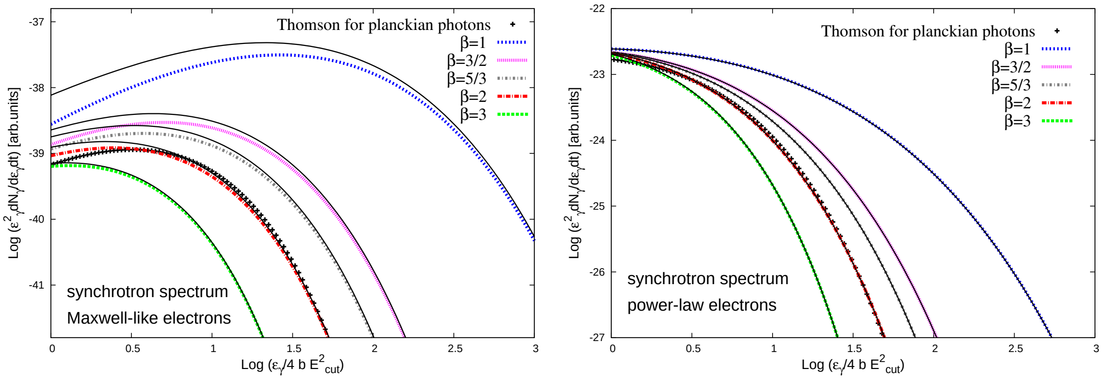

Figure 4.6: Synchrotron spectrum of relativistic Maxwell-like (left panel) and power-law (right panel) electrons. With black crosses the Thomson spectrum is shown for Planckian photons and $\beta = 2$, scaled to $E_\gamma/5kTE_{cut}^2$ and normalized to the synchrotron flux. At large energies, the Thomson and synchrotron spectra show similar shape of the cutoff and the corresponding index is $\beta/(\beta+2)$. The cutoff energy for the electrons is $E_c = 10^2$ and the magnetic field $B = 1G$.

where $E_0 = 4bE_c^4$ is the maximum photon energy that results from electrons with energy E_c when they up-scatter synchrotron photons with energy ϵ_0. The analogy with the case of Planckian soft photons is direct. Replacing the synchrotron characteristic energy bE_c^2 with kT results in the same saddle point.

Here the second derivative of the exponent at the saddle point has a simple form

$$S''(z_0) = \frac{\beta E_0}{2E_\gamma}\frac{1}{\epsilon_0^2}, \tag{4.44}$$

so that the integration over the synchrotron number density gives

$$\left.\frac{d\dot{N}_\gamma}{dE_\gamma}\right|_{SSC}^{T} = \frac{3}{4\pi c R^2}\frac{2\pi^2 r^2 c A^2 (mc^2)^{\alpha+1}\sqrt{3}q^3 B}{2^\alpha\sqrt{\beta(\beta+2)}h}\left(\frac{E_\gamma}{b}\right)^{\frac{\alpha}{2}}\frac{G(\tilde{y}_0)}{z_0}\tilde{y}_0^{\,-\frac{\alpha}{2}-3}\, e^{-\frac{\beta+4}{\beta}\tilde{y}_0}, \tag{4.45}$$

where $\tilde{y}_0$ is calculated at the saddle point

$$\tilde{y}_0 = \frac{\beta}{2}\left[\frac{2E_\gamma}{\beta E_0}\right]^{\frac{\beta}{\beta+4}}, \qquad E_0 = \frac{4bE_c^4}{(mc^2)^2}. \tag{4.46}$$

In the case of SSC radiation, the electron distribution up-scatters the synchrotron photon distribution with an exponential cutoff $\exp[-(\epsilon_\gamma/\epsilon_c)^{\frac{\beta}{\beta+2}}]$. The corresponding Compton flux at high energies exhibits a cutoff index $\beta/(\beta+4)$ which is smoother than the seed synchrotron distribution,

$$\left.\frac{E_\gamma d\dot{N}_\gamma}{dE_\gamma}\right|_{SSC}^{T} \propto \exp\Big[-\frac{\beta+4}{2}\left(\frac{2E_\gamma}{\beta E_0}\right)^{\frac{\beta}{\beta+4}}\Big]. \tag{4.47}$$

For $\beta = 1$, 2 and 3, the corresponding values for the Thomson exponential index are 1/5, 1/3 and 3/7 respectively, significantly less than the electron distribution index and different than the ones in the synchrotron case. If $\beta \to \infty$, then the SSC spectrum shows a simple cutoff, like in the case of up-scattering Planckian photons. The asympotic formula of eq. (4.45) is shown in fig. 4.7 for Maxwellian and power-law electrons.

In the Klein-Nishina regime, the integration over the synchrotron photon density can not be performed analytically for arbitrary values of the indexes α and β. In this regime however, the soft photon field does not play an important role in the shape of the up-scattered spectrum close to the maximum cutoff. Thus, eq. (4.17) for monochromatic photons offers a rather good description of the asymptotic behavior of the SSC spectrum at Klein-Nishina regime. See e.g. fig. 4.8 for Maxwellian and power-law electrons. The analytic formula describing the asymptotes in eq. (4.17) normalized to the numerical solution, where the soft photon energy ϵ_γ has been replaced by $\epsilon_s = bE_c^2$.

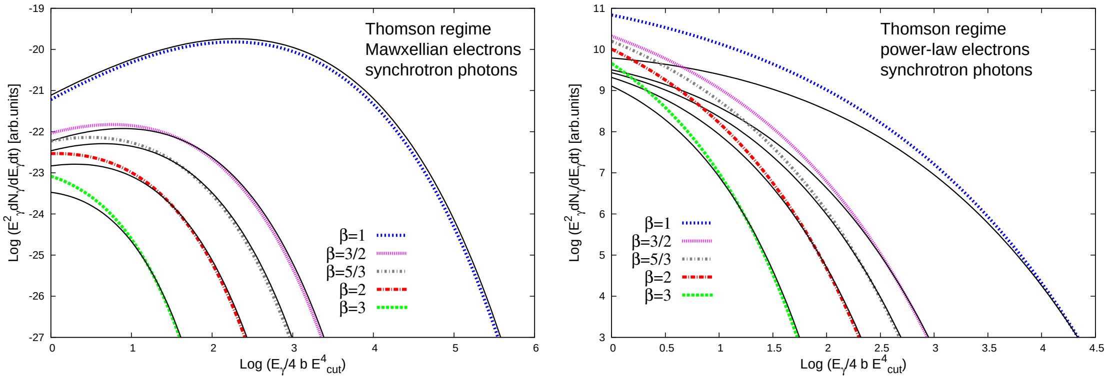

Figure 4.7: (a) SSC radiation at the cutoff region in Thomson regime. A Maxwellian electron distribution has been used, with parameters $E_c = 10^2$ and $B = 1G$ for the magnetic field. The exponential cutoff that arises is very smooth, with an index of $\beta/(\beta+4)$. (b) Same as in the left panel but for power-law electrons. The asymptotics approach the numerical solution only for $E_\gamma \gg 4bE_{cut}^4$. Very close to the photon cutoff energy, the numerical spectrum is smoother than the approximated one.

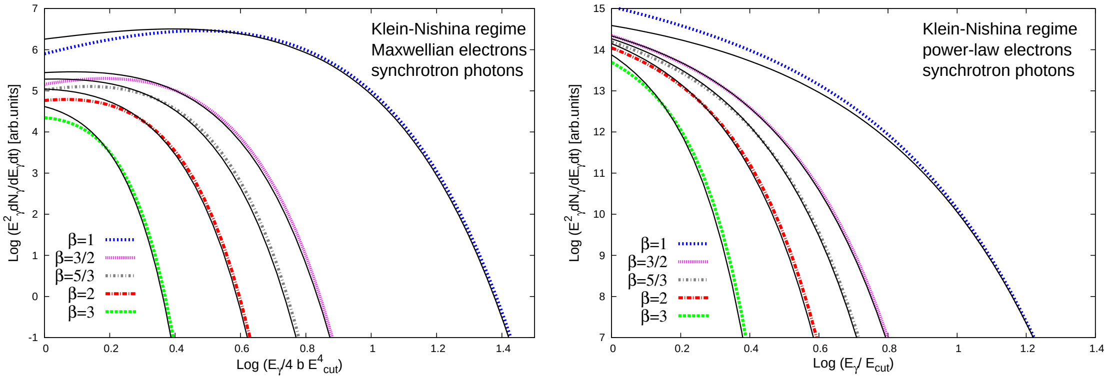

Figure 4.8: SSC radiation at the cutoff region in the Klein-Nishina regime for Maxwellian (left panel) and power-law (right panel) electrons. The parameters used are $E_c = 10^5$ and $B = 1G$, so that the parameter $\eta_c \approx 4bE_c^4$ that defines the domain of the scattering is $\eta_c \approx 90 \gg 1$. The analytical formula plotted here is eq. (4.12) for monoenergetic photons with $\epsilon_\gamma = bE_{cut}^2$, scaled to the numerical spectrum. The cutoff shape has the same index β, as the electron distribution.

4.4 Cooled electron distribution

In the previous sections we have assumed that the particle distribution that radiates is either uncooled or the radiative cooling is taken into account at the formation of the distribution. The latter is indeed very often the case. For example, in stochastic acceleration scenarios the relativistic Maxwell-type distribution is the steady state solution of the corresponding Fokker-Planck equation at which synchrotron type losses are included. If Compton losses in the Klein-Nishina regime dominate then the cutoff is smoother (Stawarz & Petrosian 2008), but can be still represented by an exponential cutoff with smaller index β and thus it can be directly connected to the cutoff shape of the photon spectrum through our approximations. In Diffusive Shock Acceleration (DSA), for an energy-dependent diffusion coefficient (e.g. Bohm diffusion) when energy losses are taken into account the electron distribution exhibits an exponential cutoff (Zirakashvili & Aharonian 2007). There is however one remaining possibility that is often considered when modeling the SED of Blazars. If particles cool in a zone different than the one in which they are accelerated then the exponential cutoff linked to the radiated spectrum is not the one that characterizes the injected distribution as energy losses may alter its shape.

In the aforementioned case, we can describe the problem by the electron' s kinetic equation

$$\frac{dN_e}{dt} - \frac{\vartheta}{\vartheta E_e}\left(\dot{E}_e N_e\right) = Q_0 E_e^{\alpha} e^{-(\frac{E_e}{E_c})^{\beta}}. \tag{4.48}$$

In the steady state ($\vartheta/\vartheta t = 0$) the solution becomes

$$N_e = \frac{1}{\dot{E}_e}\int_{E_e}^{\infty} Q_0 E_e^{\alpha} e^{-(\frac{E_e}{E_c})^{\beta}} dE_e. \tag{4.49}$$

The above integral does not have a general solution, however we can study some special cases with representative values for the exponential index. For $\alpha = -2$ and $\beta = 1$, we find

$$N_e \propto E_e^{-2}\left(\frac{e^{-\frac{E_e}{E_c}}}{E_e} - \frac{\Gamma[0, \frac{E_e}{E_c}]}{E_c}\right), \tag{4.50}$$

where $\Gamma[x, y]$ represents the incomplete Γ function. The first terms represents the cooled distribution with the characteristic power-law slope of $\alpha - 1 = -3$ in this case and an exponential cutoff with the same index β as for the injected particle distribution. This is the leading term of the solution whereas the second term only introduces a small modification. Thus, the exponential shape remains almost the same after cooling in contrast to the power-law part which is changed significantly by a factor of 1 (see fig. 4.9, left panel). Similar conclusions can be made for the case of $\beta = 2$ for which the solution becomes

$$N_e \propto E_e^{-2}\left(\frac{e^{-\frac{E_e}{E_c}}}{E_e} - \frac{\sqrt{\pi} Erfc[\frac{E_e}{E_c}]}{E_c}\right), \tag{4.51}$$

where $Erfc[x]$ gives the complementary Error function. The change in the exponential index is also very small with respect to the uncooled electron distribution

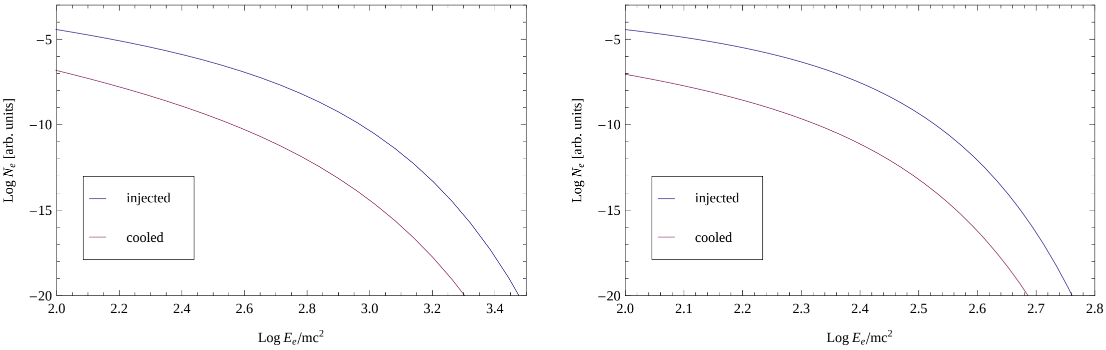

Figure 4.9: Injected and cooled (steady-state) electron distributions for energies larger than the cutoff energy. Here $E_c = 100/mc^2$ and the power-law index is $\alpha = -2$. In the left panel the exponential cutoff has index $\beta = 1$, whereas in the right panel $\beta = 2$. In both cases the modification of the exponential part of the distribution due to cooling is not severe.

(see fig. 4.9, right panel). The main reason is that at the high energy cutoff the exponential function results in a very sharp decrease of the distribution and thus the cooling of the particles does not seriously affect the shape. Although it is not possible to perform analytical approximations for the Compton spectrum that is derived from the distribution of eq. (4.50) and (4.51), we may still approximately infer the injected electron exponential index from the observed spectrum.

4.5 Comparison of the results

The main results of this chapter are summarized in table 4.1. In the Klein-Nishina regime the up-scattered Compton spectrum exhibits the same exponential cutoff index β_C, as the electron distribution index β, and does not depend strongly on the target photon field. This implies that from the γ-ray spectrum we practically "observe" the electron cutoff shape. In particular, an abrupt electron distribution cutoff ($\beta \to \infty$) would result in an abrupt cutoff for the photon spectrum ($\beta \to \infty$). The case of up-scattering monochromatic photons is shown in fig. 4.2 . The case of Planckian photons is plotted in fig. 4.5, whereas fig. 4.8 corresponds to the SSC spectrum. In all of these cases, the asymptotics are rather good just after the peak of the SED.

On the contrary, in the Thomson regime the up-scattered photon exponential shape is always smoother than the electron distribution cutoff shape. For monochromatic target photons this is $\beta_C = \beta/2$, as shown in fig. 4.1. In this case, the shape of the cutoff in both Thomson and Klein-Nishina regime (eqs. 4.13 and 4.18) shows that using a δ-function for the Compton emissivity provides the correct result. Here the asymptotic analytic expression of eq. (4.12) approaches better the numerical solution for a Maxwellian electron distribution.

Interestingly, for Planckian photons we find a different relation between β_C and β, which is the same as for synchrotron radiation, $\beta_C = \beta/(\beta + 2)$. As can be seen from fig. 4.4, the approximation is very good. Finally, for synchrotron photons it holds that $\beta_C = \beta/(\beta+4)$. As in the case of monochromatic photons, the SSC asymptotics in the Thomson regime are better for Maxwellian electrons. Our results are supported from numerical studies regarding log-parabolic electron distributions and the curvature of the emitted spectra (Massaro et al. 2006).

In general, although in the Klein-Nishina regime the Compton spectrum preserves the electron distribution index $\beta_C = \beta$, in the Thomson regime the up-scatter photon cutoff index is always smaller than the electron distribution cutoff, $\beta_C < \beta$. The only exception occurs for monochromatic photons up-scattered by electrons with $\beta \to \infty$. In this case the Compton spectrum should exhibit as well an abrupt cutoff. For Planckian and synchrotron photons $\beta \to \infty$ for electrons means a simple exponential cutoff for the Compton SED, $\beta_C = 1$.

The reason why an abrupt cutoff for the electron distribution results in the same index $\beta_C = 1$ for both Planckian and synchrotron photons is related to the fact that electrons with a sharp cutoff radiate photons with sharp cutoff as well in the case of monochromatic photons (the most narrow and sharp soft photon field that can be assumed). Thus, when the target photons are not monoenergetic, the Thomson spectrum that arises from electrons with $\beta \to \infty$, practically reveals the soft photon distribution at energies close to the maximum cutoff. As both synchrotron and Planckian photon fields exhibit the same dependance on the soft photon energy ($\exp(-\epsilon_\gamma/\epsilon_0)$), the resulting Thomson spectrum is the same at high energies for both cases. If however the soft photon distribution exhibits a cutoff with different dependance on the photon energies, then the radiated Compton SED would differ. One may easily check that if e.g. soft photons exhibit an exponential cutoff shape of the form $\exp[-(\epsilon/\epsilon_0)^\lambda]$, then the upscatter Thomson distribution will lead to a exponential cutoff of the same index λ. If we do not consider an abrupt cutoff for the electron distribution then the Thomson spectrum for synchrotron photons is smoother than in the case of Planckian photons, making these two cases distinguishable for the Thomson regime.

The Thomson spectrum for Planckian photons exhibits a cutoff index $\beta_S = \beta/(\beta+2)$, the same as the synchrotron spectrum. Thus, if the SED of the observed object is considered to consist of these two components (synchrotron radiation for the low energies and up-scattering of Planckian photons in the Thomson regime for high energies), then the exponential part of the two "bumps" is very similar (see fig. 4.6). This is not true if the up-scattering occurs in Klein-Nishina regime at the cutoff region. While $\beta_S = \beta/(\beta+2)$ for the synchrotron component cutoff, $\beta_C = \beta$ for the high energy component. Even if we consider an abrupt cutoff for the electron distribution, the two bumps would be different ($\beta_S = 1$ and $\beta_C \to \infty$, respectively). For an SSC model, the two components do not show the same exponential cutoff shape neither in the Thomson (where we get $\beta_S = \beta/(\beta+2)$ and $\beta_C = \beta/(\beta+4)$ for low and high energies respectively), nor in the Klein-Nishina regime ($\beta_S = \beta/(\beta+2)$ and $\beta_C = \beta$). Only if the electron distribution has an abrupt cutoff, then in the Thomson regime we can get $\beta_C = \beta_S = 1$, while in the Klein-Nishina regime $\beta_C \to \infty$. Thus, the two components of the SED do not show in general the same shape at the cutoff region.

Table 4.1: The index of the exponential cutoff in the energy spectrum of IC radiation β_C calculated for three different target photon fields, in the Thomson and Klein-Nishina regimes. The index β characterizes the exponential cutoff in the electron energy distribution given by Equation 4.1.

scattering regime	Thomson	KN	Thomson	KN
electrons radiation field	β	β	abrupt	abrupt
monochromatic photons	$\beta/2$	β	∞	∞
Planckian photons	$\beta/(\beta+2)$	β	1	∞
synchrotron photons	$\beta/(\beta+4)$	β	1	∞

4.6 The cutoff energy of the Compton spectrum

Apart from the shape of the up-scattered, photon spectrum at the cutoff region, another interesting point is the cutoff energy itself, $E_{\gamma,cut}$. We have shown that in the Klein-Nishina regime this remains always at $E_{\gamma,cut} = E_c$, the same as the electron distribution cutoff energy, independently of the soft photon field. On the contrary, at the Thomson regime, the cutoff photon energy depends on the target photon field. For the monochromatic target photons the value of $E_{\gamma,cut}$ is obvious; it is simply equal to the cutoff energy of electrons. For monochromatic photons, the resulting value of $E_{\gamma,cut}$ is rather obvious, simply because there is a maximum up-scattered photon energy for the fixed electron energy. Consequently, the cutoff energy of the IC spectrum must be equal to the maximum up-scattered photon energy by electrons of energy E_c, as it follows from (eq. 4.13),

$$E_{\gamma,cut} = \frac{4E_c^2\varepsilon_0}{(mc^2)^2}. \tag{4.52}$$

On the other hand, in the case of a broad distribution of target photons, the relation between E_c and $E_{\gamma,cut}$ depends on the seed photon spectrum and the index β of the electron distribution. For the Planckian photon distribution, we find (see eq. 4.30)

$$E^{BB}_{\gamma,cut} = \frac{4E_c^2kT}{(mc^2)^2}\left(\frac{2}{\beta+2}\right)^{\frac{\beta+2}{\beta}}\frac{\beta}{2}. \tag{4.53}$$

In analogy to the monoenergetic photons case, the maximum energy at which electrons of energy E_c can radiate, when they up-scatter photons of energy kT, is $4E_c^2KT/(mc^2)^2$. In respect to this, the Thomson spectrum cutoff energy is smaller by a factor of $(\beta/2)[2/(\beta+2)]^{(\beta+2)/2}$. This factor is not negligible especially for small β, e.g. it takes values of ~ 0.15, 0.25 and 0.33 for $\beta = 1$, 2 and 3 respectively (almost one order of magnitude for a simple exponential cutoff). As expected, it tends to unity for $\beta \to \infty$. It does not depend however on the index α of the electron distribution.

For synchrotron radiation, from eq. (4.41), we find the cutoff energy

$$\epsilon_{\gamma,cut}^{SYN} = bE_c^2 \left(\frac{2}{\beta+2}\right)^{\frac{\beta+2}{\beta}} \frac{\beta}{2}, \tag{4.54}$$

which reveals exactly the same factor as in the case of Thomson spectrum for Planckian photons, but now in respect to the characteristic energy bE_c^2.

Finally, for the case of SSC, eq. (4.47) gives

$$E_{\gamma,cut}^{SSC} = \frac{4bE_c^4}{(mc^2)^2} \left(\frac{2}{\beta+4}\right)^{\frac{\beta+4}{\beta}} \frac{\beta}{2} = \frac{4E_c^2\, \epsilon_{\gamma,cut}^{SYN}}{(mc^2)^2} \left(\frac{2}{\beta+4}\right)^{\frac{\beta+4}{\beta}} \left(\frac{\beta+2}{2}\right)^{\frac{\beta+2}{\beta}} \tag{4.55}$$

If we compare the cutoff energy with e.g. $4bE_{cut}^2\, \epsilon_{\gamma,cut}^{SYN}/(mc^2)^2$ then the factor related to the index β takes values of ~ 0.035, 0.15 and 0.25 for $\beta = 1$, 2 and 3, which are slightly less than in the case of a Planckian target photon field. This is due to the fact that the cutoff shape is now smoother. These analytic results are useful when modeling the observed spectrum, as one may infer the electron distribution cutoff energy from the photon spectrum cutoff energy with only the uncertainty introduced by a (possible) Doppler boosting. The position and the amplitude of the synchrotron and IC peaks in the SED contain very important information about physical parameters of non-thermal sources, like the strength of the average magnetic field and the energy density of relativistic electrons. The shape of the SED, especially in the region of the cutoffs of the synchrotron and IC components of radiation, provide additional, more detailed information about the distributions of electrons and magnetic fields. For example, the spectral cutoff in the IC component formed in the the Klein-Nishina regime provides direct, model-independent information about the energy spectrum of the highest energy electrons. This is a critical issue for understanding the particle acceleration mechanisms. Furthermore, combined with the shape of the synchrotron cutoff, it allows us to extract information about the distribution of the magnetic field. This can be demonstrated by the following simple example. Let as assume that we have observed a smooth synchrotron cutoff which can be interpreted as the result of an electron distribution with an exponential index e.g. $\beta \approx 1$. This hypothesis can be checked by the shape of the cutoff of the IC component. If the IC spectrum is formed in the Klein-Nishina regime, and exhibits a sharp cutoff behavior indicating an electron distribution with $\beta > 1$, then one should attribute the smoothness of the synchrotron cutoff to magnetic field inhomogeneities rather than to the actual shape of the electron distribution.

4.7 Summary

In this study we have examined the asymptotic behavior of the Compton spectrum close to the maximum cutoff. We assumed that the electron distribution follows the general formula $E_e^\alpha \exp[-(E_e/E_c)^\beta]$ so that our analysis may account for a relativistic Maxwellian-type distribution, as well as for a power-law distribution with exponential cutoff. The exponential cutoff of the electron energy spectrum results in an exponential cutoff in the Compton spectrum, of the form $\exp[-(E_\gamma/E_{\gamma,cut})^{\beta_c}]$, with β_c and $E_{\gamma,cut}$ the corresponding cutoff index and energy respectively. We show that in the Klein-Nishina regime, the cutoff index remains unchanged, $\beta_c = \beta$. The shape of the up-scattered spectrum close to the maximum cutoff basically "reflects" the electron distribution and does not depend strongly on the target photon field. The cutoff energy also corresponds to the electron distribution cutoff energy, $E_{\gamma,cut} = E_c$.

In the Thomson regime, the resulting spectrum close to the cutoff is very different. First of all it strongly depends on the up-scattered photon field. Monoenergetic photons lead to a cutoff of index $\beta_c = \beta/2$, whereas Planckian photons result in $\beta_c = \beta/(\beta + 2)$. When the up-scattered photon field is the synchrotron photon field, as in SSC models, then the cutoff appears extremely smooth, with an index $\beta_c = \beta/(\beta + 4)$. In contrast to the Klein-Nishina regime, the Thomson spectrum cutoff energy $E_{\gamma,cut}$ depends not only on the electron distribution cutoff energy, but also on the target photon field and as well on the index β.

The obtained analytic expressions are useful for deriving the electron spectral shape at the cutoff region directly from the observed high energy flux. These two parameters may give important insight into the acceleration and radiation mechanisms acting in the source. Furthermore, one may use the higher energy part of the observed Compton spectrum as a "diagnostic tool" to distinguish between EC and SSC models, as different photon fields lead to different cutoff shapes.

Chapter 5

On radiation boosting due to relativistic motion and effects of anisotropy

5.1 Introduction

In the previous chapters we examined in detail several aspects of the radiation processes that account for the Blazar spectra. Apart from the importance of a self-consistent approach for the hard spectra interpretation, we have discussed the functional dependance (on energy) of the emitted synchrotron and ICS spectrum at low and high energies. Below the minimum cutoff, the emitted flux is $F_\nu \propto \nu^{1/3}$ for the synchrotron and SSC mechanisms, whereas for the EC scenario, $F_\nu \propto \nu$ (if the target photon field is narrow, like in the case of Planckian photons). We have also examined the shape of the synchrotron and ICS spectrum close to the maximum cutoff, and we have provided analytical approximations that are illustrating for the acceleration process of the electrons. For the synchrotron spectrum the exponential cutoff index becomes $\beta/(\beta+2)$, whereas for the ICS spectrum it strongly depends on the regime for scattering as well as on the target photon field. In the intermediate regime, i.e. the power-law part of the spectrum, the shape is well known (see however appendix). It roughly follows $F_\nu \propto \nu^{-(s-1)/2}$, where s is the power-law index of the electrons, for both synchrotron and Thomson spectra. An exception holds for the Klein-Nishina regime of the ICS where $F_\nu \propto \nu^{-s}$.

The investigation of the emitted spectrum has proven very illustrating for the properties of the parent particles. An important "ingredient" needed for the calculation of the observed spectrum is the modification of the intrinsic spectrum due to Doppler boosting. In general, when it comes to AGNs (but also to GRBs, microquasars etc.), the radiation processes occur within a jet that moves at relativistic velocities. Relativistic Doppler boosting effects are then expected to lead to a significant enhancement of the radiated flux measured by a distant observer.

In this chapter, we discuss the anticipated beaming pattern for synchrotron, synchrotron-self Compton (SSC) and external Compton (EC) emission. In the EC case, where the soft seed photon field for inverse Compton upscattering is assumed to be dominated by an ambient photon source external to the jet, the beaming pattern has been previously discussed by Dermer (1995) and Georganopoulos et al. (2001) using two different approaches: By first transforming the soft photon field to the jet frame (where the electron distribution is considered to be isotropy) and then the radiative outcome back to the observer frame; and by first transforming the electron distribution from the jet to the ambient photon frame.

Here, we solve the photon transfer equation which allows one to derive the different beaming patterns in a concise way that is also applicable to more general (e.g., non-stationary, non-homogeneous and/or anisotropic) electron distributions. This allows us to investigate an interesting deviation from "standard" models, the case of anisotropic particles and how this anisotropy may affect the results.

5.2 Photon transfer

Let $g(\mathbf{k}, \mathbf{r}, t)$ be the (invariant) distribution function of photons in phase space, so that their differential number (an invariant) is

$$dN_\gamma = g(\mathbf{k}, \mathbf{r}, t) d^3k \; d^3r \,, \tag{5.1}$$

where $\mathbf{k}$ denotes the photon momentum vector. The photon transfer equation for optically-thin media is

$$\left(\frac{\partial}{\partial t} + c\mathbf{n} \frac{\partial}{\partial \mathbf{r}} \right) g(\mathbf{k}, \mathbf{r}, t) = Q(\mathbf{k}, \mathbf{r}, t) \,, \tag{5.2}$$

where Q represents a source of photons, $\mathbf{n} = \mathbf{k}/|\mathbf{k}|$ is the unit vector in the direction of photon propagation, and c is the speed of light. In the following, we set $c = 1$ and $\hbar = 1$.
If the source emits a photon at $(\mathbf{r}_0, t_0)$, this is detected at $(\mathbf{r}, t)$, where

$$\mathbf{r} - \mathbf{r}_0 = \mathbf{n}(t - t_0) \,. \tag{5.3}$$

Then, the solution to eq. (5.2) can be found from the corresponding Green function, and reads

$$g(\mathbf{k}, \mathbf{r}, t) = \int_{-\infty}^{t} dt_0 \int d^3r_0 \delta(\mathbf{r} - \mathbf{r}_0 - \mathbf{n}(t - t_0)) \times Q(\mathbf{k}, \mathbf{r}_0, t_0) \,. \tag{5.4}$$

We need to integrate over the direction of photons as we are interested in the total number of photons that reach point $\mathbf{r}$. Thus, we define the function

$$\tilde{g}(k, \mathbf{r}, t) = \int g(\mathbf{k}, \mathbf{r}, t) d\Omega_{\mathbf{n}} \,. \tag{5.5}$$

By substituting the photon momentum vector $\mathbf{k}$ in the source term $Q(k, \mathbf{r}, t)$ by $k\mathbf{n} = \frac{(\mathbf{r} - \mathbf{r}_0)}{|\mathbf{r} - \mathbf{r}_0|}$, the only dependency on $\mathbf{n}$ remains through the δ-function which we can transform in spherical coordinates using

$$\delta(\mathbf{x} - \mathbf{x}') = \frac{1}{r^2 \, \sin\theta} \delta(r - r')\delta(\theta - \theta')\delta(\phi - \phi') \,, \tag{5.6}$$

so the integral over the solid angle reads

$$\int \delta(\mathbf{r} - \mathbf{r}_0 - \mathbf{n}(t - t_0))\, d\Omega_{\mathbf{n}} = \frac{\delta(|\mathbf{r} - \mathbf{r}_0| - (t - t_0))}{|\mathbf{r} - \mathbf{r}_0|^2}\,, \tag{5.7}$$

Using the above equation, the function $\tilde{g}$ becomes

$$\tilde{g}(k, \mathbf{r}, t) = \int_{-\infty}^{t} dt_0 \int d^3r_0\, \frac{Q(\mathbf{n}k, \mathbf{r}_0, t_0)}{|\mathbf{r} - \mathbf{r}_0|^2}\, \delta(|\mathbf{r} - \mathbf{r}_0| - (t - t_0))\,, \tag{5.8}$$

and the integration over time results in

$$\tilde{g}(k, \mathbf{r}, t) = \int d^3r_0 \frac{Q(\mathbf{n}k, \mathbf{r}_0, t - |\mathbf{r} - \mathbf{r}_0|)}{|\mathbf{r} - \mathbf{r}_0|^2}\,. \tag{5.9}$$

At large distances $r \gg R_0$, with R_0 the typical dimension of the source, we can expand $|\mathbf{r} - \mathbf{r}_0| \approx r - (\mathbf{n}_r \mathbf{r}_0)$, where $\mathbf{n}_r = \mathbf{r}/r$ denotes the unit vector in the direction of $\mathbf{r}$ and where $\mathbf{n} \approx \mathbf{n}_r$, i.e., all photons detected by a distant observer essentially travel in the direction of $\mathbf{r}$. In this case the solution becomes

$$\tilde{g}(k, \mathbf{r}, t) = \int d^3r_0 \frac{Q(\mathbf{n}_r k, \mathbf{r}_0, t - r + (\mathbf{n}_r \mathbf{r}_0))}{r^2}\,. \tag{5.10}$$

Using the above equation, we can now find the beaming pattern for various processes. Let K' be the source frame and K the observer' s frame. Noting that g is invariant, we can see from eq. (5.2) that

$$\epsilon Q(\mathbf{k}, \mathbf{r}, t) = \epsilon' Q'(\mathbf{k}', \mathbf{r}', t') \Rightarrow Q(\mathbf{k}, \mathbf{r}, t) = \frac{Q'(\mathbf{k}', \mathbf{r}', t')}{D}\,, \tag{5.11}$$

where ϵ denotes the photon energy and D the Doppler factor. If we assume (without loss of generality) that the source is moving with velocity V along the z-axis, then (in Cartesian coordinates) $d^3r_0 = dx_0 dy_0 dz_0$, where

$$\begin{aligned} x_0 &= x_0', \;\; y_0 = y_0', \\ z_0' &= \Gamma(z_0 - V[t - r + n_x x_0 + n_y y_0 + n_z z_0])\,, \end{aligned} \tag{5.12}$$

with $\Gamma = (1 - V^2)^{-1/2}$, so that $dz_0' = \Gamma(1 - V n_z) dz_0 = dz_0/D$, and obviously

$$d^3r_0 = D d^3r_0'\,. \tag{5.13}$$

Note that in the last relation the Lorentz factor Γ comes from length contraction, whereas the factor $(1 - V n_z)$ corresponds to the effect that the relativistic motion of the source has on the received radiation related to the emitted one. In Georganopoulos et al. (2001), this additional Doppler factor was treated as an effective volume that appears in the calculation of the observed flux and corresponds to the emitting volume at the retarded time. Substituting eq. (5.11) and eq. (5.13) into eq. (5.10) for the function $\tilde{g}$, it follows directly

$$\tilde{g}(k, \mathbf{r}, t) = \int d^3r_0' \frac{Q'(\mathbf{k}', \mathbf{r}_0', t' - r' + (\mathbf{n'}_r \mathbf{r'}_0))}{r^2}\,. \tag{5.14}$$

Non stationarity

From the above relation we can see that considering a non-stationary source would differ from the stationary case only if variations in the source occur on timescales smaller than the light crossing time of the source ($t' < R_0$). Such variations are however smoothed out and are not expected to be observed due to casuality arguments. Thus, we assume that the source does not depend on time

$$\tilde{g}(\mathbf{k}, \mathbf{r}, t) = \int d^3 r_0' \frac{Q'(\mathbf{k}', \mathbf{r}_0')}{r^2} \,. \tag{5.15}$$

Let us assume that the source is spherical, isotropic and homogeneous. Then we can write in the frame K' of the source

$$Q'(k', r_0') = Q'(k') \; \Theta(R_0'^2 - r_0'^2) \,, \tag{5.16}$$

so that function $\tilde{g}$ takes on a simple form,

$$\tilde{g}(k, \mathbf{r}, t) = \int_{V'} dV' \, \frac{Q'(k')}{r^2} \,, \tag{5.17}$$

with V' the volume of the source. Note that in spherical coordinates $dN_\gamma = g \; d^3k d^3r = g \; \epsilon_\gamma^2 d\epsilon_\gamma d^3r$, so that the number of photons per energy, per unit volume (integrated over photon directions), is $\tilde{g}\epsilon_\gamma^2$. Thus, the energy flux $F_\epsilon \propto \epsilon_\gamma dN_\gamma / d\epsilon_\gamma d^3 r_0$ (multiplied by the speed of light) that the observer receives is related to $\tilde{g}$ according to

$$F_{\epsilon_\gamma} = \epsilon_\gamma^3 \tilde{g}(k, \mathbf{r}, t) \,. \tag{5.18}$$

With the same argument we can write $j'_{\epsilon'_\gamma} = Q'(k')\epsilon_\gamma'^3$ for the emission factor of the source. Thus, we conclude that the beaming pattern follows the known relation (Lind & Blandford 1985)

$$F_{\epsilon_\gamma} = \frac{D^3}{r^2} \int_{V'} dV' j'_{\frac{\epsilon_\gamma}{D}}(\frac{\epsilon_\gamma}{D}) = \frac{D^{3+\alpha}}{r^2} \int_{V'} dV' j'_{\frac{\epsilon_\gamma}{D}}(\epsilon_\gamma) \,, \tag{5.19}$$

where the last equality holds if the source has a spectral index α (i.e., $j'_{\epsilon'} \propto \nu'^{-\alpha}$). For synchrotron or SSC emission (in Thomson limit) of a power-law electron distribution of index p, the resultant spectral index is $\alpha = (p-1)/2$ (e.g., Blumenthal & Gould 1970). Hence, for the canonical index $p = 2$, $\alpha = 0.5$ and the dependance on the doppler factor becomes $D^{3.5}$.

For the external Compton case the corresponding formula for $\tilde{g}$ is given by

$$\begin{aligned} \tilde{g}(k, \mathbf{r}, t) \;\; &= \;\; \frac{1}{r^2} \int \int d^3 r_0 \, f_e(\mathbf{p}, \mathbf{r}_0, t - r + \mathbf{n}_r \mathbf{r}_0) \; n_{\rm ph}(\epsilon_{\rm ph}) \\ &\quad \times W(\mathbf{p}, \epsilon_{\rm ph}, \epsilon_\gamma, \mathbf{n}_r k) \; d^3p \; d\epsilon_{\rm ph} \,, \end{aligned} \tag{5.20}$$

where $f_e(\mathbf{p}, \mathbf{r}, t)$ is the distribution function of the electrons with momentum $\mathbf{p}$ that up-scatter a soft photon field of number density $n_{\rm ph}(\epsilon_{\rm ph})$. The function W

is the scattering probability. As before, we consider a spherical blob containing a stationary electron distribution that moves with relativistic velocity in the z-direction. The distribution function is Lorentz-invariant, so that we can write

$$\begin{aligned} \tilde{g}(\mathbf{k},\mathbf{r},t) &= \frac{D}{r^2}\int\int d^3r'_0\ f'_e(\mathbf{p}',\mathbf{r'_0})\ n_{\mathrm{ph}}(\epsilon_{\mathrm{ph}}) \\ &\quad \times W(\mathbf{p},\epsilon_{\mathrm{ph}},\epsilon_\gamma,\mathbf{n}_r k)\ d^3p\ d\epsilon_{\mathrm{ph}}\,. \end{aligned} \tag{5.21}$$

We make the approximation that the up-scattered photons move in the electrons' direction, so that the observed flux becomes

$$F_{\epsilon_\gamma} = \frac{D^3}{r^2}\int N'_e(\frac{E_e}{D})\ W(E_e,\epsilon_{\mathrm{ph}},\epsilon_\gamma)dE_e\ n_{\mathrm{ph}}(\epsilon_{\mathrm{ph}})\ d\epsilon_{\mathrm{ph}} \tag{5.22}$$

where $N_e(E_e)$ denotes the differential number of electrons per energy per solid angle, and $W = \epsilon_\gamma dN_\gamma/dtd\epsilon_\gamma$ is the scattered photon energy spectrum per electron (Blumenthal & Gould 1970). If the electron distribution obeys a power-law, $N'_e(E'_e) \propto E'^{-p}_e$, the beaming pattern becomes

$$F_{\epsilon_\gamma} \propto D^{3+p}\,. \tag{5.23}$$

In the Thomson limit, the integral in eq. (5.22) results in a power-law inverse Compton spectrum of index $\alpha = (p-1)/2$. Substituting this, gives a beaming pattern dependence of the form $F_{\epsilon_\gamma} \propto D^{4+2\alpha}$ in the case of external Compton. Hence, the beaming pattern is obviously different for the synchrotron or SSC mechanism when compared with the external Compton (Thomson) case (Dermer 1995).

5.3 Non-isotropy

In this paragraph we examine how anisotropy in the source may alter the above conclusions. Anisotropic emission can be caused due to two different reasons. The particle distribution might be anisotropic, as being formed e.g. in relativistic jets when radiation losses are taken under account (see e.g. Dempsey & Duffy 2007), in the converter mechanism (Derishev et al. 2003) or due to relativistic pair plasma reconnection (see e.g. Cerutti et al. 2012). Additionally the magnetic field in the source might not be randomly oriented and thus introduce anisotropy of the emitted radiation in the case of synchrotron and SSC radiation.

First we will assume that the anisotropy is described in the source term Q' (neglecting the physical cause) by a factor of the form $(1+\lambda'(\mathbf{n}'\mathbf{v}')^2)$. Here $\mathbf{n}'$ is the outgoing photons' unit vector and $\mathbf{v}'$ denotes a constant axis, which we will consider for simplicity to coincide with the axis of motion of the source. Then $\mathbf{n}'\mathbf{v}' = \cos(\theta'-\theta'_*)$, where θ'_* is the symmetry axis of the anisotropy. If this coincides with the axis of motion then $\theta'_* = 0$. The parameter λ' shows the degree of anisotropy. All quantities are measured in the source frame.[1]

---

[1] As we wish to describe anisotropy on a phenomenological level we assume that it can be expressed as an expansion in $\cos\theta$, i.e. $1+\lambda'_1\cos\theta+\lambda'_2\cos\theta^2+...$ We chose to neglect the first order term, or equivalently $\lambda'_1 \ll \lambda'_2$ for simplification reasons and to avoid non-physical negative values for the source.

For a spherical, stationary source, in analogy to eq. 5.17, we find

$$\tilde{g}(k, \mathbf{r}, t) = \int_{V'} dV' \left(1 + \lambda' \cos^2(\theta' - \theta'_*)\right) \frac{Q'(k')}{r^2} , \tag{5.24}$$

In order to normalize with respect to the isotropic case, we demand the total emitted power (integrated over volume and energy) to be the same independent of the angular distribution of the emitted photons. This yields a normalization factor of the form

$$B(\lambda, \theta_*) = \left(1 + \frac{\lambda'}{2} - \frac{\lambda'}{3} \cos 2\theta'_*\right) . \tag{5.25}$$

If we denote with θ_0 the viewing angle then we find that the observed flux should be

$$F_{\epsilon_\gamma} = \frac{D^3}{B(\lambda, \theta_*) r^2} \left[1 + \lambda' \left(\frac{(\cos\theta_0 - V)\cos\theta'_* + \frac{\sin\theta_0}{\Gamma_c}\sin\theta'_*}{1 - V\cos\theta_0}\right)^2\right] \int_{V'} dV' j'_{\frac{\epsilon_\gamma}{D}} \left(\frac{\epsilon_\gamma}{D}\right) , \tag{5.26}$$

due to light abberation. The total emitted luminosity ($\int F_{\epsilon_\gamma} d\epsilon_\gamma$) for different observation angles is shown in fig. 5.1 for different values of the degree of anisotropy λ parameter. In fig. 5.2 the same case is shown but for slower outflows where the effects of anisotropy are more evident. One can see that the maximum of the observed radiation does not occur at $\theta_0 = 0$ as it happens in the isotropic case (except for $\theta'_* = 0$). Instead it is shifted to higher angles as the axis of anisotropy increases. An additional effect regards the estimation of the doppler factor.

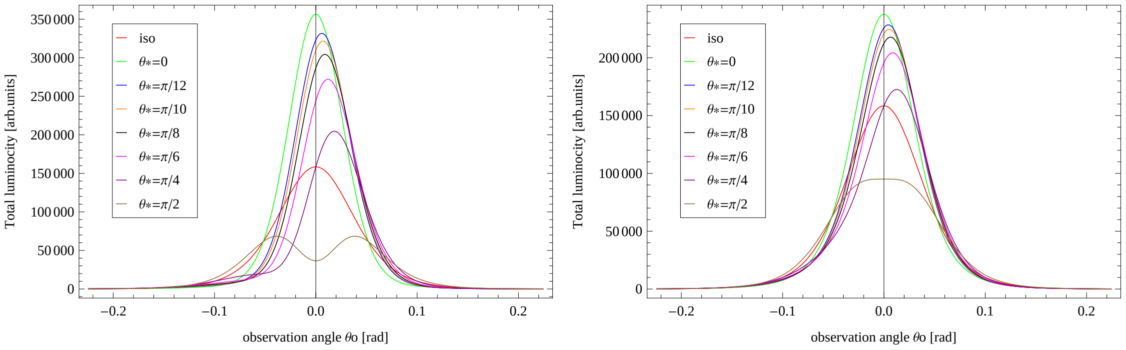

(a) (b)

Figure 5.1: (a) Angular distribution (in respect to the observation angle θ_0). Here the jet bulk Lorentz factor is $\Gamma_c = 10$ and θ_* denotes the "axis of anisotropy". The parameter λ' is 5. (b) Same as in the left panel but for the case $\lambda' = 1$

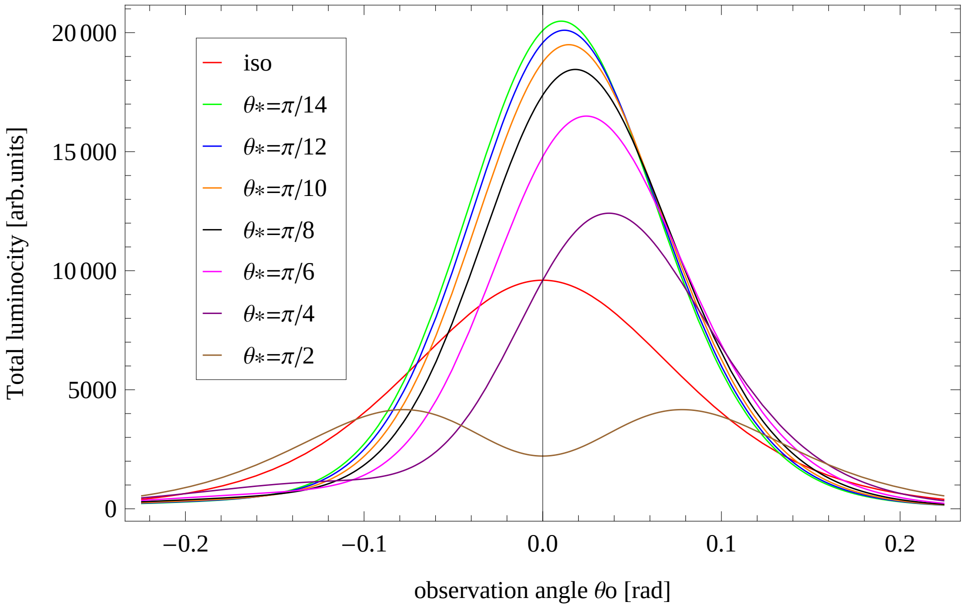

Figure 5.2: Same as 5.2 but for $\Gamma_c = 5$ and $\lambda' = 5$. The effects of anisotropy is more evident for slower moving source as the doppler boosting is not so strong.

The same intrinsic emitted power results in different values of the observed luminosity, which can differ significantly from the luminosity in the isotropic case (e.g. by a factor of 3 as can been seen in fig. 5.1). This leads to a possible mis-estimation of the doppler factor of the source if the observed luminosity is compared with the intrinsic (extracted by the model) luminosity. The slower is the outflow (fig. 5.2), the more evident are the effects of anisotropy, as the Doppler boosting is less strong.

In a more general picture we can allow the parameter λ' to depend on energy. We will assume that the emitting particles are anisotropic. This could be the case e.g. in diffusive shock acceleration (DSA), where the lower energy particles get isotropized at the downstream region due to pitch-angle scattering, whereas the higher energy particles radiate their energy before they have enough time to isotropize (see e.g. Derishev et al. 2007). It is difficult however to decouple the electron space distribution from the magnetic field structure but as a first approximation we will consider a randomly oriented magnetic field. For simplicity we will assume that the λ' parameter depends on some power of the energy, $\lambda' \to \lambda'\gamma'^{p_1}$, so that the electron energy distribution follows the form

$$N_e'(\gamma') = k_e(1 + \lambda'\gamma'^{p_1}\cos^2(\theta - \theta_*))\gamma'^{-p}e^{-\left(\frac{\gamma}{\gamma_c}\right)^{\beta}} \tag{5.27}$$

We normalize in respect to the isotropic case as before, assuming that the total energy integrated over volume

$$\int_{V'}\int_{\gamma'} N_e'(\gamma')\gamma' mc^2 d\gamma' dV' \tag{5.28}$$

is the same for both cases. For illustration we will examine the synchrotron and EC radiation (for a detailed discussion on synchrotron and IC spectra from anisotropic

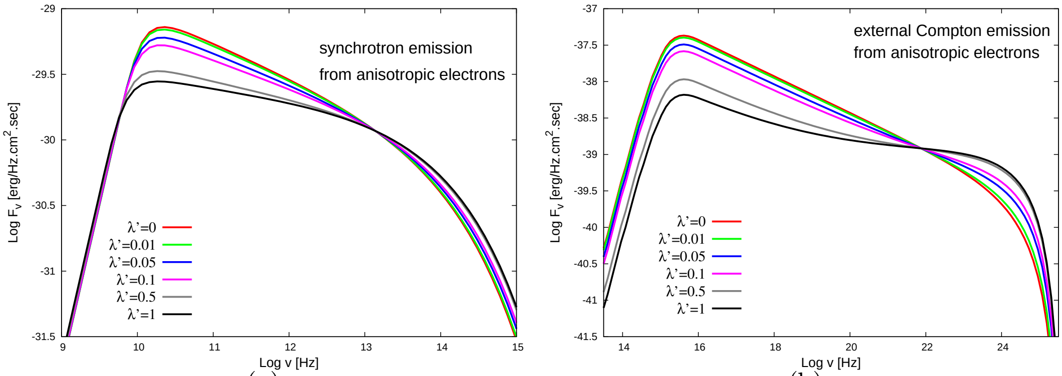

(a) (b)

Figure 5.3: (a) Observed synchrotron flux from anisotropic electrons. With the red line the isotropic case is shown ($\lambda = 0$). The anisotropy axis here is $\theta_* = 0$, whereas the viewing angle is $\theta_0 = 4^o$. As the parameter λ increases, the spectrum becomes harder. Parameters of the source are $\Gamma_c = 10$, $R = 10^{14}$cm, $B = 0.3G$, $\gamma_c = 10^4$, $p = 2$ whereas the dependance of the anisotropy factor is assumed to be $\propto \gamma^{0.5}$. (b) EC emission for Planckian photon field (with the same parameters for the electron distribution). The effect of anisotropy are more evident than in the synchrotron spectrum because the EC emission extends over a larger energy band.

particle distributions see Derishev et al. 2007). The observed spectrum for both cases is shown in fig. 5.3, for the values $p' = 2$ and $p'_1 = 1/2$.

The synchrotron spectrum (left panel) appears harder for more anisotropic particle distributions and the low energy break appears slightly shifted to lower energies. In the isotropic case the photon SED index is $F_\nu \propto \nu^{-0.5}$ as expected and for $\lambda = 1$ (the contribution of the anisotropic part of the particle distribution dominates the emission) the spectrum roughly becomes $F_\nu \propto \nu^{-0.26}$ because in this case

$$N_e \propto \gamma^{-p+p_1}. \tag{5.29}$$

In the ICS spectrum (right panel) the effect of anisotropy is more evident. This happens because in comparison to the synchrotron spectrum, the ICS extends over a larger energy band. When λ' is close to one, we can clearly see that at high energies the spectrum is harder than at low energies, as expected for an anisotropic factor that increases towards larger electron energies. Thus, a spectral hardening occurs and the slope change value from the one that corresponds to $N_e \propto \gamma^{-p}$ up to the value that corresponds to $N_e \propto \gamma^{-p+p_1}$.

Obviously, this spectral feature is related to the dependance of λ' on the electron energy. We note that the SSC spectrum is expected to differ substantially from the EC spectrum due to the fact that the target photon field in this case (the synchrotron photons) will be as well anisotropic. Thus, one can no longer use eq. 5.22, but instead needs to calculate the emitted flux for anisotropic electrons and photons. This is however, beyond the scope of this chapter.

5.4 Conclusions

In various astrophysical objects, like AGNs, microquasars and GRBs, the observed flux emerges from a relativistically moving source. The Doppler boosting due to this motion enhances substantially the emitted flux and thus the observed spectrum appears different than the intrinsic one. A deep understanding of the Lorentz transformations that are required is important. In this chapter we have obtained in a compact mathematically way, i.e. by solving the photon transfer equation, the beaming pattern for the synchrotron, IC and SSC radiation (note that the formula for the synchrotron beaming pattern can be applied for any radiation mechanism for which the intrinsic photon distribution is known). Our calculations allow for a generalization of the previously obtained results, i.e. they can account for general electron distributions, non-stationary, non-homogeneous and non-isotropic.

Non-stationarity is an important characteristic especially of Blazars (but as well as for GRBs and microquasars) because these objects are very often observed to exhibit violent changes in their flux. We have discussed that time variability affects the beaming pattern only if the timescale of variability is less than the dynamical timescale of the source. In this case however, the variations would be smoothed out and not observed in such small timescales due to casuality arguments. On the other hand, the assumption of non-isotropic particles is very well justified in various acceleration theories, as DSA and magnetic reconnection.

We have shown that strong anisotropy modifies the total luminosity, an effect that becomes more prominent in slower (but still relativistic) outflows, because the modification due to anisotropic effects competes with the effects of Doppler boosting. In respect to the isotropic case the total luminosity peaks at different viewing angles and it also appears enhanced, leading to a possible mis-estimation of the source Doppler factor (we have normalized in respect to the total intrinsic power emitted). Under the assumption that the emitting particles are more anisotropic at higher energies, the spectrum may appear harder. How hard the spectrum can become is relevant to the energy dependance that the particle distribution' s anisotropy exhibits. This effect is more evident in the EC component than in the synchrotron component as it extends over a larger energy band. In any case, once anisotropic effects become evident, the slope of the emitted spectrum differs from the one that results from the acceleration of the particles.

Chapter 6

Leptonic radiation from stratified jets

6.1 Evidence for non-homogeneous outflows

As shown in the previous chapter, deviation from isotropy may lead to interesting features of the observed spectrum and the total luminosity may differ significantly from the one that corresponds to the isotropic case. Another assumption that is usually made, when modeling the high energy emission of Blazars, regards the homogeneity of the source. In general, the leptonic radiation is regarded to originate from a homogeneous (and isotropic) part of the jet, where the parameters of the bulk flow do not depend on the space coordinates. This is the case in the one-zone, homogeneous SSC model, where the parent electrons are considered to be contained in a homogeneous, spherical blob. In the EC models the same assumptions for the emitting particles are made in the majority of the cases.

However, such an approach appears adequate only to a first approximation, since real jets are naturally expected to exhibit a significant stratification. There is plenty of observational evidence that the jets' physical parameters, like the bulk velocity or the magnetic field, vary in space. For example, VLBI observations of the intensively studied Mkn 501 and Mkn 421 show a limb-brightening morphology (Giovannini et al., 1998, 1999). A similar behavior has been observed in 3C274 and 1144+35 (Giovannini et al., 2001). In the nearby radio galaxy M87 complicated structures (side-to-side oscillations, transverse expansion) are revealed by VLBI maps (Reid at al. 1989). Owen et al. (1989) have explained these structures in terms of a boundary shear layer that dominates the dynamics of the jet. Later, radio polarization measurements of M87 have confirmed this complex structure. The optical jet appears considerably more compact than the radio jet, and the observed knots are more centrally concentrated (Perlman et al. 1999).

Similar morphologies have been seen in other FR I sources, such as 3C 31 (Laing, 1996; Laing & Bridle, 2002) and 3C296 (Hardcastle et al. 1997), where spine-layer structures are confirmed on kpc scales giving evidence for strong velocity shear. Even at parsec scales the radio jet of the Blazar 1055+018 exhibits a transverse structure consistent with the existence of an inner spine and a distinct boundary layer (Attridge et al. 1999). The polarization studies support the outcome of the radio observations as they have shown that the magnetic field topology changes within the jet. The longitudinal and toroidal components become dominant in different parts of the jet and at the boundary it does not have a transverse component (e.g. Laing et al. 2006). In the presence of a strong velocity shear, the magnetic field tends to become parallel to the flow velocity (see e.g. Kahn, 1983; Begelman et al., 1984). This is due to the sheared flow stretching the lines of force of any magnetic field frozen into the plasma. The dominant field direction is therefore parallel to the jet axis.

In principle the presence of brightness variations inside the jet has been confirmed in several sources (e.g. Laing et al., 2006a,b). Apart from transverse velocity structures, stratification along the jet has been claimed in several cases. For example, the side-to side asymmetries observed in a sample of low-luminosity FR I radio galaxies are consistent with the hypothesis that the jet is decelerating from relativistic velocities close to the core to lower velocities farther away, indicating longitudinal velocity structures (Laing et al. 1999).

Apart from the aforementioned observational evidence for stratification, hydrodynamical studies support as well the existence of jet stratification. Hydrodynamical simulations give rise to a fast spine that is surrounded by a slower layer (Aloy et al. 2000). Coupled with the magnetohydrodynamical properties of the bulk flow, synthetic synchrotron emission maps have, been investigated for a 2-component jet (an inner relativistic outflow and an outer cold disk wind) in order to reproduce the limb-brightening morphology of M87 (Gracia et al. 2009). Various MHD simulation models for jet formation suggest that a spine-layer structure naturally arises as the inner jet is launched by the central Black Hole via the Blandford-Znajek process, whereas the outer layer is formed from the cold disk wind (see the introduction for more details).

One should also mention that the presence of a velocity structure in the jet can resolve difficulties in the unification of FR I sources and BL Lacs, if the jets of these sources are indeed intrinsically identical (Chiaberge et al. 2000). The different beaming due to velocity differences would then alter the observed properties of these sources. It seems thus interesting to study in more detail the emission properties of a jet that exhibits stratification in its bulk velocity and the magnetic field. Additionally, because the acceleration of the particles to relativistic energies depends on these parameters, it appears promising to extend the consideration for stratification to parameters that characterize the emitting particles, such as the number density and the maximum energy of the distribution.

The modifications of the observed spectrum due to possible boundary layers has been early realized from Komissarov (1990), mainly with respect to the effects that the different relativistic beaming of the different parts of the jet has on the overall spectrum. Several authors have attempted to approach open problems in the AGNs' physics and phenomenology within leptonic models assuming the radiation to originate in inhomogeneous jets. Velocity variations have been examined in both the longitudinal and transverse direction and interesting effects of the stratification on the emitted flux have been discussed.

Motivated by observational implications for jet deceleration Georganopoulos & Kazanas (2003) have shown that, if the jet deceleration occurs within the γ-ray emitting zone, then the particles at the base of the jet will see the photons from the deceleration zone boosted. This leads to an enhancement of the Compton component and allows for less extreme values of the physical parameters of the jet in comparison to the homogeneous SSC models. On the other hand, Ghisellini et al. (2005) have examined the synchrotron and Compton emission from a spine+layer system. The interplay between the two zones through inverse Compton scattering can cause significant deceleration of the jet due to Compton drag (Phinney, 1982; Sikora et al., 1996). The layer, having a smaller bulk Lorentz factor emits in a cone much wider than the spine. Observers at large viewing angles should then see the layer, not the spine and vice versa. Depending on whether the emission from the core or the layer dominates the high energy component of the observed spectrum, the overall radiation from these jets may exhibit characteristics similar to the ones of BL Lac objects or FRI radio galaxies, "pairing" in this way these different sources (see e.g. the case of M87 in Tavecchio & Ghisellini 2008).

The transverse velocity profile that Ghisellini et al. (2005) examined is practically a step-function. Regarding smooth transverse velocities profiles, Li et al. (2004) and Yang et al. (2009) have investigated the synchrotron and Compton emission from a jet with a continuous decrease of the bulk Lorentz factor from the core of the jet to the edge. As it seems, the unification of BL Lacs and FRI may be less constrained by the viewing angles, but rather be imprinted by velocity structures intrinsic to the jets themselves. Furthermore, in the comoving frame, the SSC process, in the case of a stratified jet, has properties similar to the EC model (Li & Wang 2004).

Once a velocity structure exists in the jet, additional particle acceleration is expected to occur in the shear flow (see e.g. Rieger & Duffy 2004). As the particles scatter of the magnetic field inhomogeneities, they gain energy traveling through the shear. This stochastic process can be efficient enough to lead to the formation of relativistic particle distributions. The diffusive shock acceleration process seems to be a plausible mechanism for the origin of the non-thermal power-law distributions in the case of relativistic parsec scale AGN jets. In large-scale jets however, shear acceleration might represent an attractive mechanism for boosting of particles at high energies (Rieger et al. 2007). In any case, even in small scale jets, it is possible that stochastic processes operate at least complementary to the DSA (re-acceleration).

Stawarz & Ostrowski (2002) examined the expected radiated spectra of such distributions that can be generated at the boundary shear layers of large scales jets, showing that the emission of these electrons can substantially contribute to the jet radiative output and create observational signatures characteristic of the shear acceleration. Aloy & Mimica (2008) further investigate more complex velocity profiles in order to show observable differences with respect to conventional monotonic and smooth boundary layers.

Obviously, studying the emission properties of a jet that exhibits stratification seems not only highly motivated by observations, but it also appears promising for approaching unresolved puzzles in AGNs' physics and phenomenology. Deviation from the standard, homogeneous models requires careful investigation of the effects that processes like Compton scattering, relativistic beaming or possible shear acceleration may have on the observed spectrum.

In this chapter we examine the synchrotron radiation from a jet that exhibits stratification in the bulk Lorentz factor, the magnetic field, but also in the number density and the maximum energy of the electron distribution. The reasoning for the latter two varying parameters regards the fact that the characteristics of the electron population are bounded to the bulk flow physical parameters through the acceleration process. We consider transverse velocity and magnetic field profiles and we assume that the dominating cooling process is synchrotron radiation.

6.2 Relativistic jet with stratification at the transverse direction

Let us consider an axisymmetric, irrotational, relativistic jet emerging from the central engine of the AGN. In cylindrical coordinates, each point of the jet is characterized by the position vector $\vec{r} = (\varpi, \phi, z)$, where z is the (longitudinal) distance from the core, ϖ is the cylindrical (transverse) radius and ϕ the azimuthal angle (see the sketch in fig. 6.1). The outflow is moving in the $\hat{z}$-direction. We assume that the jet is sufficiently collimated at distance $z_0 \sim 10^{16} cm$ (sub-parsec scale jet), which will be referred to as the base of the jet. This value for z_0 is consistent with MHD studies and moreover it is far away enough from the disk where intense photon field may exist and cool down the particle distribution very rapidly. At z_0 the outer radius is of the order of $\varpi(z = z_0) \equiv R_0 \sim z_0/10$. Up to a distance z_1 we approximate the shape of the jet with a cylinder, i.e. the outer radius varies very slowly in respect to z, $R(z) \sim R_0 \approx constant$. For $z > z_1$ the jet may start to expand in the ϖ direction, introducing adiabatic losses that make the particles inefficient emitters.

We consider a scheme where relativistic electrons are injected at the base of the jet, e.g. by 1st order Fermi acceleration at a standing shock. The presence/creation of standing shocks inside the jet has been suggested before (for instance, recollimation shocks in an initially over-pressurized outflow (Gomez et al., 1995; Perucho & Martí, 2007). The radiation of the particles that are accelerated in such shocks may dominate the observed spectrum (e.g. Mandal & Chakrabarti, 2008; Becker et al., 2008).

Let K' be the comoving flow frame and K the observer' s frame. The energy distribution of the injected electrons at the base of the jet is assumed to be a power-law with varying (with respect to ϖ coordinate) number density and maximum cutoff

$$n'_{0\varpi}(\gamma'_0) = k'_{0\varpi}\gamma_0'^{-s}\Theta(\gamma'_0 - \gamma'_{0,min})\Theta(\gamma'_{0,max} - \gamma'_0). \tag{6.1}$$

From now on we will use the notation $X_{z\varpi} = X(z, \varpi)$ for the parameter that depend on both spatial coordinates, ϖ and z. Thus $X_{0\varpi}$ symbolizes the value of the parameter X at $(z = 0, \varpi)$. An exception holds for the electrons Lorentz factors, with $gamma'_0$ to imply that the particles are the base of the edge at any radius and γ' to refer to an arbitrary point (ϖ, z) of the outflow. The parameters that depend only on the polar radius will be simply denoted as $X(\varpi)$.

The bulk velocity and Lorentz factor of the flow exhibit dependance on the cylindrical radius

$$\beta = \beta(\varpi), \quad \Gamma = \Gamma(\varpi) = \frac{1}{\sqrt{1-\beta(\varpi)^2}}, \tag{6.2}$$

and thus the Doppler factor at each point (z, ϖ) is

$$D(\varpi) = \frac{1}{\Gamma(\varpi)(1-\beta(\varpi)cos\theta_0)}, \tag{6.3}$$

implying different beaming for each point of the jet. As we will consider decreasing velocity profiles from the center to the edge, the inner layers of the jet will radiate in a smaller cone than the outer layers. We furthermore assume that the magnetic field depends as well on the ϖ coordinate, $B = B(\varpi)$. For simplicity, we consider that the dominant cooling process is synchrotron radiation. The particles loose energy as they travel along the jet according to

$$\frac{d\gamma'}{dz'} = \frac{d\gamma'}{dt'}\frac{dt'}{dz'} = -\frac{4}{3}\frac{\sigma_T c}{mc^2}U'_B(\varpi)\gamma'^2\frac{dt'}{dz'}. \tag{6.4}$$

It holds that $dz' = c\beta(\varpi)dt'$ and due to Lorentz transformations, $dz = \Gamma(\varpi)dz'$, we find

$$\frac{d\gamma'}{dz} = \frac{d\gamma'}{\Gamma(\varpi)dz'} = \frac{1}{c\beta(\varpi)\Gamma(\varpi)}\frac{d\gamma'}{dt'}. \tag{6.5}$$

In principle, all the parameters are expressed for convenience in the comoving frame, apart from the spatial coordinates. Practically, z corresponds to the time needed for an electron to travel from the base of the jet up to the point z. Note that this is not the time coordinate. The outflow is stationary and thus the radiation that an observer receives is independent on whether the timescales of observation are smaller or larger than the light crossing time of the jet.

By expressing all spatial coordinates at the observer' s frame K we reach to the formula

$$\frac{d\gamma'}{dz} = -C'(r){\gamma'}^2, \quad C'(\varpi) = \frac{4}{3}\frac{\sigma_T U'_B(\varpi)}{mc^2}\frac{1}{\Gamma(\varpi)\beta(\varpi)}. \tag{6.6}$$

The solution of equation 6.6 results in the energy evolution of monoenergetic electrons with initial Lorentz factor γ'_0

$$\gamma' = \frac{\gamma'_0}{C'(\varpi)(z-z_0)\gamma'_0+1}. \tag{6.7}$$

Determining the electron distribution at any point (z, ϖ) of the jet can be performed in two equivalent ways. Either through the electron number conservation or by solving the kinetic equation after replacing $(t \to z)$. For a stationary, incompressible and irrotational flow (without shear or vorticity) the volume element is constant along the flow. Thus, from the conservation of the total number of particles (integrated over energies) it follows that

$$n'_{0\varpi}(\gamma'_0)d\gamma'_0 = n'_{z\varpi}(\gamma')d\gamma'. \tag{6.8}$$

We can easily calculate $d\gamma_0'/d\gamma' = (1 - \gamma' C'(\varpi)(z - z_0))^{-2}$, which, in combination with equations (6.1) and (6.6), leads to the electron's energy distribution at an arbitrary point (z, ϖ) of the jet

$$n_{z\varpi}'(\gamma') = k_{0\varpi}' \frac{\gamma'^{-s}}{[1 - \gamma' C'(\varpi)(z - z_0)]^{2-s}} \Theta(\gamma' - \gamma_{max}') \Theta(\gamma_{min}' - \gamma'), \tag{6.9}$$

where the minimum and maximum cutoff energies are given by

$$\gamma_{min}' = \frac{\gamma_{0,min}'}{C(\varpi)(z - z_0)\gamma_{0,min}' + 1}, \quad \gamma_{z,min}' = \frac{\gamma_{0,max}'}{C(\varpi)(z - z_0)\gamma_{0,max}' + 1}. \tag{6.10}$$

The local electron energy distribution preserves almost the same shape of the injected one, while the minimum and maximum cutoff decrease as shown in figure (6.2). The same result can alternatively be reached using the electrons' kinetic equation for synchrotron losses

$$\frac{\vartheta n_{z\varpi}'(\gamma')}{\vartheta t'} = \frac{\vartheta}{\vartheta \gamma'} \left(\dot{\gamma}' n_{z\varpi}'(\gamma')\right), \tag{6.11}$$

with the initial conditions imposed by equation (6.1). Changing the integration variable to $z = \Gamma(\varpi)\beta(\varpi)ct'$, we can write

$$\frac{\vartheta n_{z\varpi}'(\gamma')}{\vartheta z} = C'(\varpi) \frac{\vartheta}{\vartheta \gamma'} \left(\gamma'^2 n_{z\varpi}'(\gamma')\right). \tag{6.12}$$

The above equation has the solution of equation (6.9) (see Kardashev 1962) and allows to add more terms for possible energy losses or acceleration of the electrons.

So there is a characteristic length scale at which the electrons have radiated away all off their energy and completely cooled down. We may define this distance as

$$z_{cool} = z_0 + \frac{1}{\gamma_0' C'(\varpi)} + \frac{1}{C'(\varpi)} \tag{6.13}$$

in which the third term dominates (for $\gamma_0' \gg 1$), implying practically that this cooling length scale does not strongly depend on the initial energy of the particles, mainly because of the way electrons cool down as shown in fig. (6.2). Two distinct cases can be examined. Either the electrons lose all their energy before reaching the "top" of the jet, at a fixed distance z_1 imposed e.g. by the domination of adiabatic losses after a certain distance from the jet base, or they escape from the radiating zone before they completely cool down due to synchrotron losses.

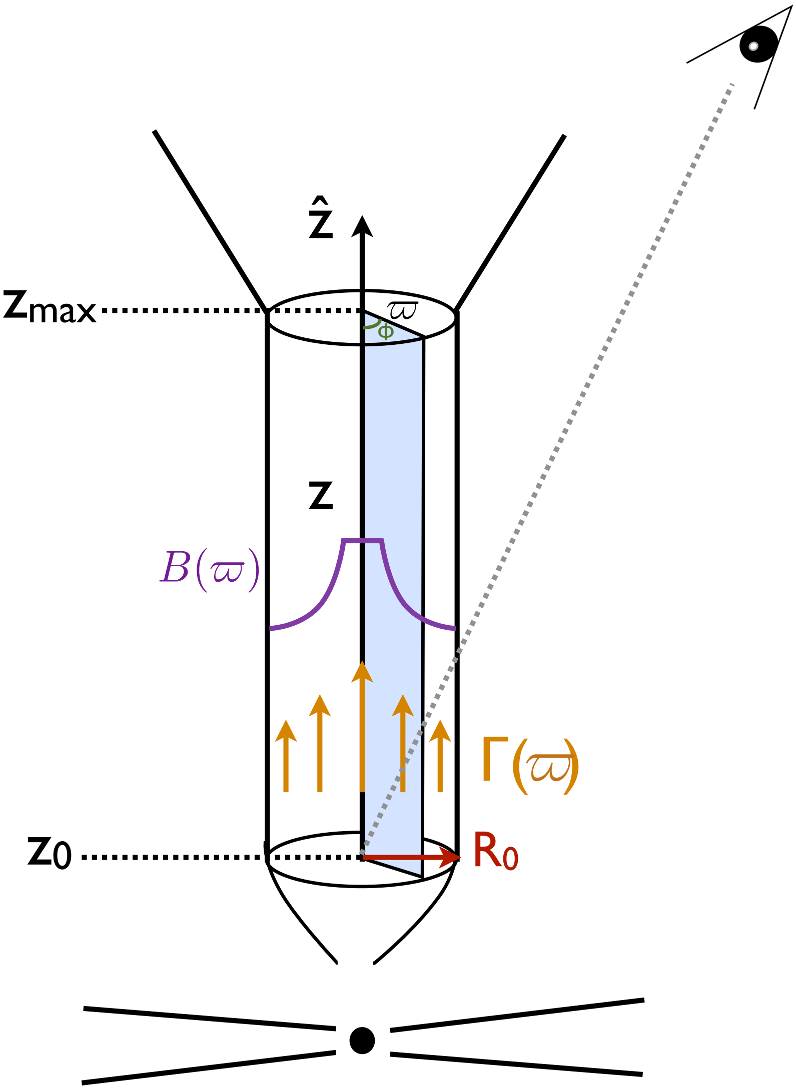

Figure 6.1: Schematic representation of the considered jet geometry. The radiation zone extends from z_0 to z_1. The particles are injected in the jet after being accelerated at its base. They cool down as the travel along the z-direction due to synchrotron energy losses.

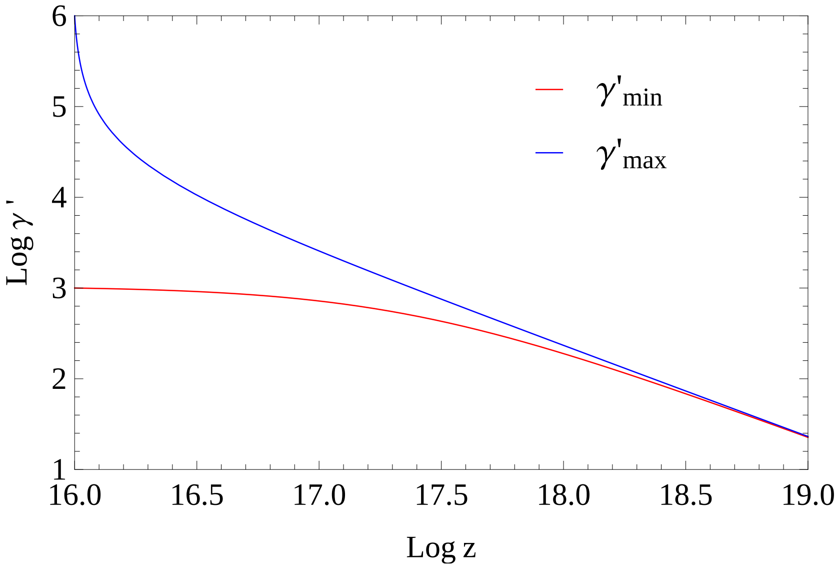

Figure 6.2: Evolution of the minimum and maximum cutoff energies of the electron distribution in respect to z. The maximum energy decreases rapidly while the minimum energy is approximately constant. After $\gamma'_{z\varpi,min} \sim \gamma'_{z\varpi,max}$ the two cutoff energies evolve together.

6.3 Properties of the layers

The reason that we have not yet specified the ϖ-dependance for the parameters of the jet and the particle distribution concerns the fact that integration over the z-coordinate is not affected by the variations along the cylindrical coordinate. The hidden assumption is that the particles' mean free path is smaller than the scale at which the velocity changes significantly. Thus, one may determine the particle distribution, as well as the synchrotron emission, in each layer. This can be illustrating for the multiple luminosity profiles from different velocity and magnetic field structures.

6.3.1 Electron distribution integrated over the longitudinal direction

With the local electron energy distribution of equation (6.9) at hand, the z-integrated energy distribution reads

$$n'_{\varpi}(\gamma') = \int_{z_0}^{z_1} n'_{z\varpi}(\gamma')dz. \tag{6.14}$$

From the properties of the heaviside step-function yields that

$$\Theta(\gamma' - \gamma'_{min}) = \Theta\left(z - z_{min}(\gamma')\right), \quad \Theta(\gamma'_{max} - \gamma') = \Theta\left(z_{max}(\gamma') - z\right), \tag{6.15}$$

where

$$z_{min}(\gamma') = z_o + \frac{1}{C'(\varpi)}\left(\frac{1}{\gamma'} - \frac{1}{\gamma'_{0,min}}\right), \quad z_{max}(\gamma') = z_o + \frac{1}{C'(\varpi)}\left(\frac{1}{\gamma'} - \frac{1}{\gamma'_{0,max}}\right). \tag{6.16}$$

Due to the above limitations, the integration limits become

$$n'_{\varpi}(\gamma') = \int_{max[z_0, z_{min}(\gamma')]}^{min[z_1, z_{max}(\gamma')]} \frac{k'_{0\varpi}\gamma'^{-s}}{[1-\gamma' C'(\varpi)(z-z_0)]^{2-s}}dz. \tag{6.17}$$

The comparison of the various length scale elements entering the limits of integration will reveal the different branches of the solution. One can see e.g. that $z_1 < z_{max}(\gamma')$, when $\gamma' < \gamma'_{1,max}$. The Lorentz factor $\gamma'_{1,max}$ corresponds to the energy that an electron should have when it reaches the top of the jet, if it's initial energy is at the high energy cutoff $\gamma'_{0,max}$

$$\gamma'_{1,max} \equiv \frac{\gamma'_{0,max}}{1 + C'(\varpi)(z_1 - z_0)\gamma'_{0max}}. \tag{6.18}$$

The value of $\gamma'_{1,min}$ for the injected low cutoff energy is correspondingly

$$\gamma'_{1,min} \equiv \frac{\gamma'_{0,min}}{1 + C'(\varpi)(z_1 - z_0)\gamma'_{0min}}. \tag{6.19}$$

Investigating all the limits of the integral and assuring that none of them overlap reveals two cases for the electron distribution depending on the maximum length scale and the injected low energy cutoff value.

- $\gamma'_{1,max} > \gamma'_{0,min}$: The electrons with injected energy at the maximum cutoff have not cooled below $\gamma'_{0,min}$ at the top of the jet.
- $\gamma'_{1,max} < \gamma'_{0,min}$: The electrons with injected energy at the maximum cutoff have traveled a long enough distance to reduce their energy below $\gamma'_{0,min}$ at the top of the jet.

In the former case, the solution becomes

$$n'_{\varpi}(\gamma') = \Lambda(\varpi) \begin{cases} \gamma'^{-s-1}\left[(1-\gamma' C'(\varpi)(z_1-z_0))^{s-1} - \left(\frac{\gamma'}{\gamma'_{0,min}}\right)^{s-1}\right], & \gamma'_{1,min} < \gamma' < \gamma'_{0,min} \\ \gamma'^{-s-1}\left[(1-\gamma' C(\varpi)(z_1-z_0))^{s-1} - 1\right], & \gamma'_{0,min} < \gamma' < \gamma'_{1,max} \\ \gamma'^{-s-1}\left[\left(\frac{\gamma'}{\gamma_{0,max}}\right)^{s-1} - 1\right], & \gamma'_{1,max} < \gamma' < \gamma'_{0,max} \end{cases} \tag{6.20}$$

where

$$\Lambda(\varpi) = \frac{k_{0\varpi}}{C'(\varpi)(1-s)}. \tag{6.21}$$

The last branch of the expression represent the cooled distribution, for which the power-law index becomes steeper by 1. The particles with energy below $\gamma'_{1,max}$ have not cooled, thus the distribution is proportional to γ'^{-s}. The first branch corresponds to a cutoff practically at $\gamma'_{0,min}$. The injected electrons with energy $\gamma'_{0,min}$ have not reduced significantly their energy, even when reaching the top of the jet, and thus $\gamma'_{1,min} \sim \gamma'_{0,min}$. For illustration see fig. 6.3.

When the opposite situation occurs, $\gamma'_{1,max} < \gamma'_{0,min}$, the solution takes the form

$$n'_{\varpi}(\gamma') = \lambda(\varpi) \begin{cases} \gamma'^{-s-1}\left[(1-\gamma' C'(\varpi)(z_1-z_0))^{s-1} - \left(\frac{\gamma'}{\gamma'_{0,min}}\right)^{s-1}\right], & \gamma'_{1,min} < \gamma' < \gamma'_{1,max} \\ \gamma'^{-2}\left[\gamma'^{1-s}_{0,max} - \gamma'^{1-s}_{0,max}\right], & \gamma'_{1,max} < \gamma' < \gamma'_{0,min} \\ \gamma'^{-s-1}\left[\left(\frac{\gamma'}{\gamma_{0,max}}\right)^{s-1} - 1\right], & \gamma'_{0,min} < \gamma' < \gamma'_{0,max} \end{cases} \tag{6.22}$$

Here all the particles completely cool down and thus the distribution exhibits two power-law indexes, $n'_{\varpi}(\gamma') \propto \gamma'^{-2}$ at high energies and $n'_{\varpi}(\gamma') \propto \gamma'^{-s-1}$ at energies below $\gamma'_{0,min}$. The first branch shows, as before, a cutoff. For constant physical parameters (no stratification) the jet geometry gives rise to particle distributions equivalent with the ones emerging from a spherical blob. The value of the time needed for the particles to escape the blob would then allow to distinguish between the two cases discussed above. Actually the condition $\gamma'_{0min} \sim \gamma'_{1,max}$ demonstrates what the horizontal size of the jet should be, in order to result in the first or second solution. If $z < z_1^*$, the size of the jet is not large enough to allow the injected electrons at the maximum cutoff to cool down to $\gamma'_{0,min}$ so that we take the first solution and vice versa. The limiting value for z_1^* is

$$z_1^* = \frac{1}{C(\varpi)} \left[\frac{1}{\gamma'_{0,min}} - \frac{1}{\gamma'_{0,max}} \right]. \tag{6.23}$$

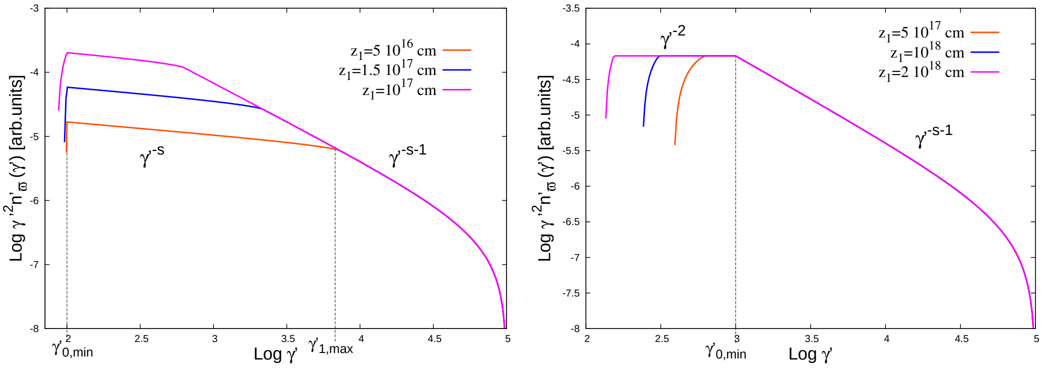

Figure 6.3: Electron energy distribution emerging from each layer. (a) A break, the value of which depends on z_1, occurs at $\gamma'_{1,max}$ below which the particles have not cooled down. Here the values for the injected distribution are $s = 2.2$, $\gamma'_{0,min} = 10^2$ and $\gamma'_{0,max} = 10^5$. The low energy cutoff is at $\gamma' \approx \gamma'_{0,min} = 10^2$. Different colures denote different maximum length scales for the emitting region. (b) The break occurs at $\gamma'_{0,min}$ (here $\gamma'_{0,min} = 10^3$) and thus remains constant in respect to z_1. For energies smaller than $\gamma'_{0,min}$ the power-law index is 2.

6.3.2 Intrinsic synchrotron emission from each layer

The energy losses for synchrotron radiation do not depend on z. This derives from the fact that synchrotron losses are constant in respect to time, something that does not hold e.g. for adiabatic losses. Thus, we may define the synchrotron emission from each layer by convolving the electron distribution of equations (6.20) and (6.22) with the synchrotron kernel. In the case of chaotic magnetic fields, the emitted synchrotron power of an electron with energy $E'_e = \gamma' mc^2$ is described by the equation

$$\frac{\epsilon'_\gamma d\dot{N}'_\gamma}{d\epsilon'_\gamma} = \frac{\sqrt{3} q^3 B'(\varpi)}{mc^2 h} \tilde{G}\left(\frac{\epsilon'_\gamma}{\epsilon'_s}\right), \tag{6.24}$$

where

$$\epsilon'_s = b'\gamma'^2 = \frac{3qB'(\varpi)h\gamma'^2}{4\pi mc} \tag{6.25}$$

is the "critical" energy for synchrotron emission, as the synchrotron power peaks at $0.29\epsilon'_s$ (e.g. Rybicki & Lightmann 1979). As in the previous chapters we will use the approximation provided in Aharonian et al. (2010)

$$\tilde{G}(y') = \frac{1.808 y'^{1/3}}{\sqrt{1 + 3.4 y'^{2/3}}} \frac{1 + 2.21 y'^{2/3} + 0.347 y'^{4/3}}{1 + 1.353 y'^{2/3} + 0.217 y'^{4/3}} e^{-\psi}. \tag{6.26}$$

The synchrotron power emitted from each layer is then

$$J'_{\varpi} = \int_1^{\infty} \frac{\epsilon'_{\gamma} d\dot{N'}_{\gamma}}{d\epsilon'_{\gamma}} n'_{\varpi}(\gamma') d\gamma' \tag{6.27}$$

The corresponding intrinsic emissivity (integrated over z) is shown in fig. 6.4. The breaks in the electron distribution result in the following synchrotron breaks

$$\epsilon'_{0,min} = b'\gamma'^2_{0,min}, \quad \epsilon'_{0,max} = b'\gamma'^2_{0,max}, \quad \epsilon'_{1,min} = b'\gamma'^2_{1,min}, \quad \epsilon'_{1,max} = b'\gamma'^2_{1,max} \tag{6.28}$$

Then, the energy dependance of the emissivity for the electron distribution of equation (6.20) exhibits roughly the following behavior

$$J'_{\varpi}(\epsilon') \propto \begin{cases} \epsilon'^{1/3}, & \epsilon' < \epsilon'_{0,min} \\ \epsilon'^{-\frac{s-1}{2}}, & \epsilon'_{0,min} < \epsilon' < \epsilon'_{1,max} \\ \epsilon'^{-\frac{s}{2}}, & \epsilon'_{1,max} < \epsilon' < \epsilon'_{0,max} \end{cases} \tag{6.29}$$

For the solution of equation (6.22) the corresponding emission factor reads

$$J'_{\varpi}(\epsilon') \propto \begin{cases} \epsilon'^{1/3}, & \epsilon' < \epsilon'_{1,max} \\ \epsilon'^{-1/2}, & \epsilon'_{1,max} < \epsilon' < \epsilon'_{0,min} \\ \epsilon'^{-\frac{s}{2}}, & \epsilon'_{0,min} < \epsilon' < \epsilon'_{0,max} \end{cases} \tag{6.30}$$

The $J'_{\varpi}(\epsilon') \propto \epsilon'^{1/3}$ dependance below the low energy cutoff is the characteristic behavior of the synchrotron function. Note that the results are applicable in the optical thin limit of synchrotron radiation.

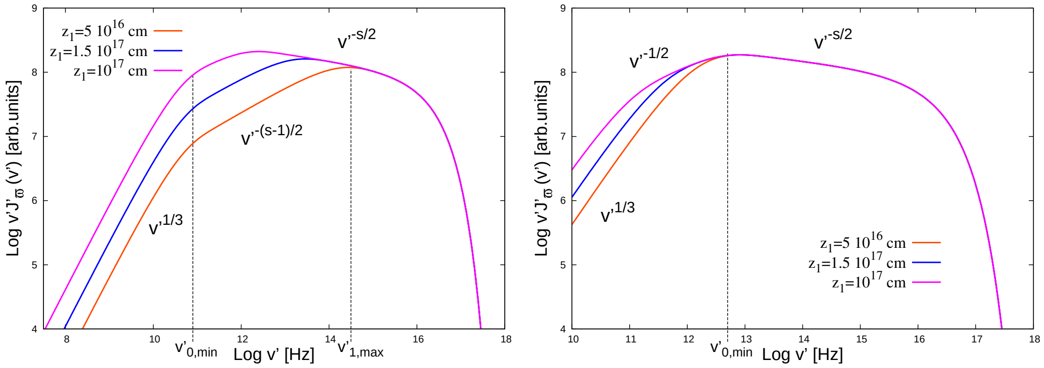

Figure 6.4: The emission factor that arises for the electron distributions plotted in fig. 6.3. The spectral index follows $J'_{\varpi}(\nu') \propto \nu'^{-(s-1)/2}$ as expected, whereas below the low energy cutoff $J'_{\varpi}(\nu')\nu'^{1/3}$. This dependance is mentioned in the plot, but note that the y-axis corresponds to $\nu' J'_{\varpi}(\nu')$ for better illustration.

6.4 Parametrization of the physical parameters

The local (and the integrated over z) particle distribution depends on the ϖ-coordinate through $k'_{0\varpi}$ and the energy losses related term $C'(\varpi)$. Thus the total, volume integrated, electron distribution may possess interesting features around the energy breaks, depending on the ϖ-dependance of these parameters. Furthermore, the radiation is boosted by the Doppler factor which, in a stratified flow, varies as well along the jet and consequently may enhance these modifications. Our scope is to investigate the observed synchrotron spectrum that arises from a stratified outflow and the possible differences compared to the homogeneous case.

We will assume that the inner core of the jet possess constant physical parameters. This corresponds to a fast spine, where the radius R_c is a free parameter of the model. Outside the core the bulk Lorentz factor changes with respect to ϖ and, at first place, we will consider the simplest case of a linear dependance within the boundary layer. Thus, the bulk Lorentz factor scales as

$$\Gamma(\varpi) = \Gamma_c \Theta(R_c - \varpi) + \left[\Gamma_c + (\Gamma_l - \Gamma_c)\frac{\varpi - R_c}{R_c - R_l}\Theta(\varpi - R_c)\Theta(R_l - \varpi)\right], \qquad (6.31)$$

where R_l is the outer radius of the jet and Γ_c, Γ_l the values of the Lorentz factor at R_c and R_l respectively. The Doppler factor which exhibits as well a dependance on the ϖ coordinate,

$$D(\varpi) = \frac{1}{\Gamma(\varpi)(1 - \beta(\varpi) cos\theta)}, \qquad (6.32)$$

is a sensitive function of the angle of observation θ. We know that for small angles, $\theta < 1/\Gamma(\varpi)$ it holds that $D(\varpi) \propto \Gamma(\varpi)$, whereas for large angles, $\theta \gg 1/\Gamma(\varpi)$ an almost inverse dependance takes place, $D(\varpi) \propto \Gamma(\varpi)^{-1}$ (see fig. 6.5). This means that in a stratified flow different characteristics may arise as the inner or outer, or even some intermediate layers may be stronger boosted.

The magnetic field $\overrightarrow{B'} = B'_z\hat{z} + B'_\varpi\hat{\varpi} + B'_\phi\hat{\phi}$ is considered to be mainly randomly oriented so that

$$\langle B'_z \rangle = \langle B'_\varpi \rangle = \langle B'_\phi \rangle = \langle B'_z B'_\varpi \rangle = \langle B'_\varpi B'_\phi \rangle = \langle B'_z B'_\phi \rangle = 0. \qquad (6.33)$$

where the brackets refer to mean in respect to spatial coordinates. Nevertheless, the "strength" parametrization of the magnetic field will be assumed to follow the scaling of one of the components. This can be justified if we consider that at the jet formation zone, close to the central engine, the magnetic field components (ordered or disordered) follow a specific scaling which is conserved at the emission zone. This implies that even if the magnetic fields gets randomized, there is still a slight domination of one of the components which is small enough to allow as to work out the radiation profile in the tangled magnetic fields regime.

Many authors discuss the magnetic field structure in the context of MHD studies. For a stationary, axisymmetric jet, in the magnetically dominated flow limit, the toroidal magnetic field at the black whole frame scales as $B_\phi \propto 1/\varpi$ (see eq. 13c in Vlahakis & Königl, 2003) and the poloidal magnetic field as $B_p \propto 1/\varpi^2$. In the fluid

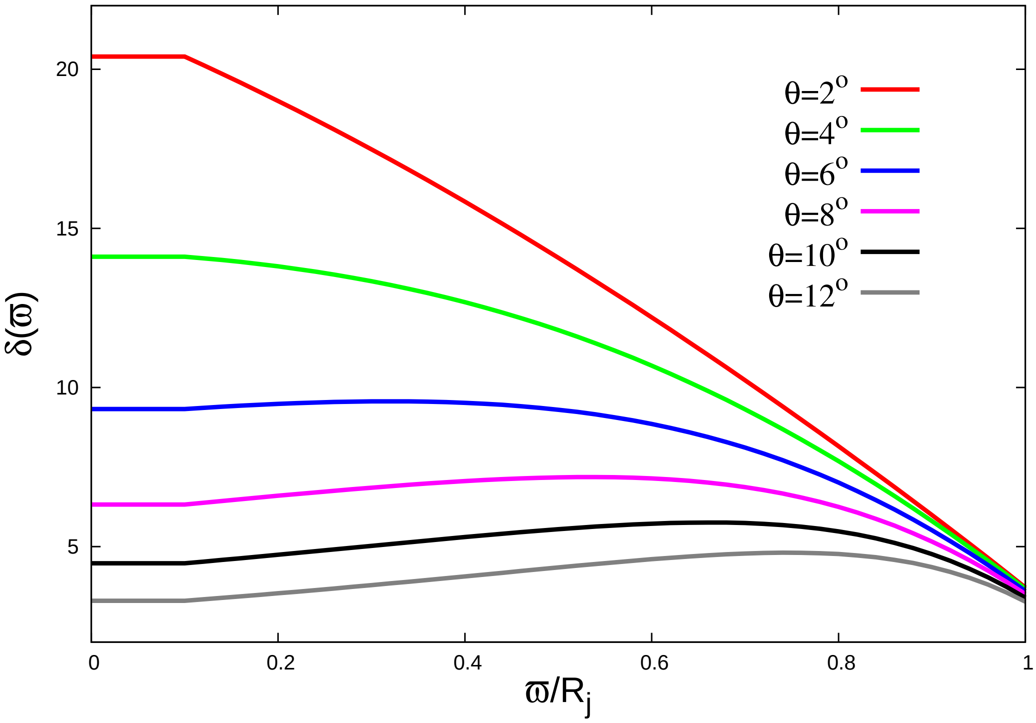

Figure 6.5: Scaling of the Doppler factor with respect to ϖ. The bulk Lorentz factor here drops from $\Gamma = 12$ to $\Gamma = 2$. The size of the inner core of the jet is $R_c = 0.1R_j$. For small angles the Doppler factor decreases following the Lorentz factor whereas for large angles is increases towards the edge of the jet. For example, for $\theta = 7^o$ the dependance on ϖ is complex and there is a slight enhancement of the intermediate layers.

reference frame, for a flow with velocity along the z-axis, the functional dependance on ϖ becomes $B'_\phi \propto 1/\Gamma\varpi$ and $B'_p \propto 1/\varpi^2$ respectively. The same conclusions were drawn earlier in Appl & Camenzind (1993) for force-free relativistic magnetic jets, sufficiently far away from the light cylinder. This picture is consistent with a current along the axis of symmetry of the jet, which creates a toroidal field which in turn sustains the current. These analytical results are supported by simulations for magnetic acceleration of AGN jets (Komissarov et al. 2007) where an initially radial magnetic field is assumed (e.g. the black hole magnetic field which in combination with rotation accelerates and collimates the jet within the Blandford-Znajek process. They are also consistent with magnetic flux conservation according to which

$$\oint \overrightarrow{B'} d\overrightarrow{S'} = 0. \tag{6.34}$$

For example, the element surface which is orthogonal to the toroidal component is $dS' = d\varpi' dz' \propto d\varpi\Gamma dz \propto \varpi\Gamma$ and thus $B'_\phi \propto 1/\Gamma\varpi$[1]. When the total outflow is

---

[1] Note however that for an adiabatically expanding jet the toroidal magnetic field should rather scale as $B'_\phi \propto 1/\varpi\Gamma(\varpi)\beta(\varpi)$, because the line element along the z direction for frozen in magnetic field depends on the velocity of the jet, $dz' \propto \Gamma(\varpi)\beta(\varpi)dt$

examined, from the black horizon to larger scales, the magnetic flux conservation results in a suppression of the longitudinal component until the jet gets collimated and can be approximated by a cylindrical flow, as the transverse surface of the jet grows with the distance from the central black hole. This implies that the magnetic field energy density is dominated by the toroidal component. On the other hand, as discussed in the introduction, the shear "drags" the magnetic field lines and thus the longitudinal component' s energy density becomes larger. Here we will examine the case at which the B_ϕ component dominates the total energy density and thus define the "strength" parametrization of the magnetic field. So in total the magnetic field scales as

$$B'(\varpi) \propto \frac{1}{\varpi \Gamma(\varpi)}. \tag{6.35}$$

The above holds at the boundary layer, in the core the magnetic field is considered, as the Lorentz factor, to be constant.

For the injected electron distribution we consider that the total number density scales according to the plasma density $\rho'(\varpi)$, as particles get accelerated at the shock from the bulk flow and assume that the ratio between the proton and electron number density remains constant (see e.g. Gracia et al. 2009). The kinetic energy density of the jet assuming cold protons, $\rho'(\varpi)\beta(\varpi)^2 c^2/2$ is in equipartition with the magnetic field energy density and thus $\rho'(\varpi) \propto B'(\varpi)^2/\beta(\varpi)^2$. The total injected electron number density $N'_\varpi(\varpi) = \int n'_\varpi(\gamma') d\gamma'$ appears to be

$$N'_\varpi(\varpi) = \frac{k'_{0\varpi}}{s-1}\left(\gamma'^{1-s}_{0,min} - \gamma'^{1-s}_{0,max}\right) \approx \frac{k'_{0\varpi}}{s-1}\gamma'^{1-s}_{0,min}, \tag{6.36}$$

for steep enough power-law ($s > 1$) and $\gamma'_{0,max} \gg \gamma'_{0,min}$. Then, the scaling of the $k'_{0\varpi}$ follows the plasma density scaling and thus

$$k'_{0\varpi} \propto \rho'(\varpi) \propto \frac{B'(\varpi)^2}{\beta(\varpi)^2} \propto \varpi^{-2}\Gamma(\varpi)^{-2}\beta(\varpi)^{-2}, \tag{6.37}$$

Of course if the electron distribution is hard, then any possible dependance of $\gamma'_{0,max}$ must be taken under account. The maximum cutoff of the injected distribution is actually expected to vary with ϖ when one considers acceleration at a standing shock. The energy up to which the particles can accelerated is limited by the energy losses due to radiation. In the simplest case of non-relativistic DSA and dominant synchrotron losses, equalizing the acceleration and cooling timescales results in the following estimation for the maximum cutoff (Rieger et al. 2007)

$$\gamma'_{0,max}(\varpi) \simeq 9\ 10^9 \left(\frac{1G}{B(\varpi)'}\right)\left(\frac{m_e}{m_p}\right)\left(\frac{V_s}{0.1c}\right), \tag{6.38}$$

where V_s the shock velocity. Thus, $\gamma'_{0,max}(\varpi) \propto B(\varpi)'^{-1/2}$.

6.5 Total observed synchrotron spectrum

With the electron distribution integrated over z at hand, we can now calculate the distribution from the whole volume of the jet by integrating over ϖ. This "total" distribution $N'_e(\gamma')$ does not have a direct observational consequence because we "see" the particles through their (synchrotron) radiation and for the calculation of the emitted spectra one has to take into account that the synchrotron power depends on the magnetic field and thus on ϖ, as well as on the Doppler factor which is also different for each layer. In other words, one can not change the order of integration between γ' and ϖ. However, the total electron distribution may prove illustrating for several implication, e.g. which layers dominate the intrinsic emission or whether special features may appear at the energy band around the breaks.

6.5.1 Total, volume integrated, electron distribution

Let as denote with R_j the outer radius of the jet so that

$$N'_e(\gamma') = \int_0^{R_j} n'_\varpi(\gamma') 2\pi\varpi d\varpi. \tag{6.39}$$

For the bulk Lorentz factor we will use the relation (6.31) considering a highly relativistic value for the inner jet, $\Gamma_c \approx 12$, which decreases linearly to substantially lower values, $\Gamma_c \approx 2 - 3$.

For the magnetic field we fix only the value at the core $B_c \approx 1G$, so that across the boundary layer the dependance on ϖ follows

$$B'(\varpi) = \frac{B_c \Gamma_c R_c}{\Gamma(\varpi)\varpi}. \tag{6.40}$$

For $R_c \sim 0.1\ R_j$ the above relation results in a decrease to $B' \sim 0,6G$ at the edge, whereas for $R_c \sim 0.2R_j$ the magnetic field at the edge is larger $B' \sim 1.2G$. Note that the above function is not always monotonically decreasing along the jet (see fig. 6.6). The same holds for the parameter $k'_{0,\varpi}$ which is as well fixed only at the center, so that

$$k'_{0,\varpi} = \frac{k'_{0,c}\Gamma_c^2 R_c^2 \beta_c^2}{\Gamma(\varpi)^2 \varpi^2 \beta(\varpi)^2}. \tag{6.41}$$

For small core radius, the value of $k'_{0,\varpi}$ at the edge of the jet is lower than at the core, whereas for $R_c \gtrsim R_j$ the opposite holds. In both cases, the aforementioned function do not result in large deviations of the values along the jet, neither for the magnetic field nor for the parameter $k'_{0,\varpi}$ of the injected electron distribution. For now, we will keep the maximum cutoff injected electron energy constant. Although a possible scaling of $\gamma'_{0,max}$ may create a modification at the higher energy part of the electron distribution, the radiated spectrum should not be much influenced. The maximum synchrotron energy is

$$\epsilon'_{0,max} \propto B'(\varpi)\gamma'^2_{0,max}, \quad \gamma'_{0,max} \propto 1/\sqrt{B'(\varpi)}, \tag{6.42}$$

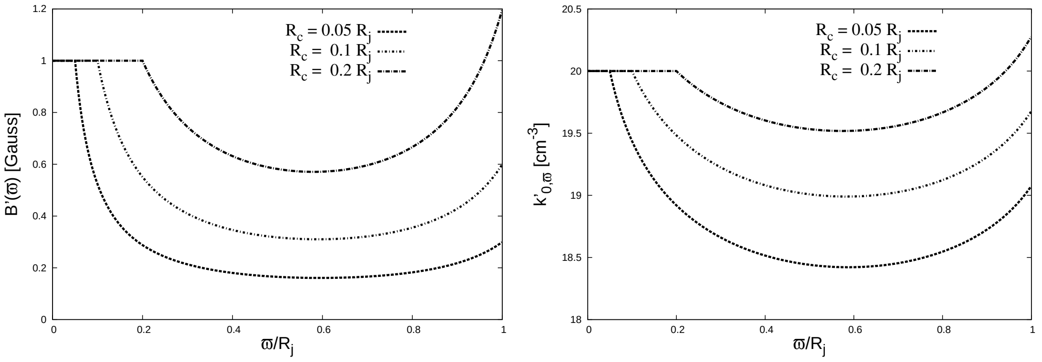

Figure 6.6: (a) Scaling of the magnetic field (left panel) and the number density of the injected electrons (right panel). None of these functions are not monotonic in respect to ϖ. For small core radius the corresponding values in the edge are less than in the center, whereas for $R_c \gtrsim R_j$ the opposite holds. For $R_c = 0.1R_j$ the highest difference for the values of the magnetic field is much less than a order of magnitude and for $k'_{0,\varpi}$ this is almost an order of magnitude.

independent of the magnetic field stratification. The synchrotron maximum cutoff energy "hides" any information for the source magnetic field (in the case of first order Fermi acceleration) and thus it is not expected to have a crucial contribution in any possible deviation from the standard homogeneous, 1-zone models. Only due to the different Doppler boosting of each layer one may expect to see some effect close to the maximum cutoff. However, the synchrotron cutoff exhibits an exponential index which is small (always less than unity, see chapter 4) and normally smooths out any modification at the high energies.

Let us distinguish two cases according to whether the particles follow the solution (6.20) or (6.22). These are shown in fig. 6.7 and 6.8 respectively. In the former case it is difficult to say which layers dominate as the cooling break $\gamma'_{1,max}$

$$\gamma'_{1,max} \sim \frac{1}{C'(\varpi)(z_1 - z_0)} \propto \varpi^2 \Gamma(\varpi)^3 \beta(\varpi), \tag{6.43}$$

is not a monotonous function of ϖ (see fig. 6.7, right panel). It seems though that the outer layers form the total electron distribution, for the value of the central core that we have chosen $R_c = 0.1\ R_j$. For the solution of eq. 6.22, the break at the electron energy distribution is constant, as it corresponds to $\gamma'_{0,min}$. What varies in this case, is the minimum cutoff of the total distribution, which results in a distribution below $\gamma'_{0,min}$ slightly harder than the γ'^{-2} slope that characterizes each layer. As for $\gamma'_{1,max}$, the minimum cutoff does not varies monotonically along the jet. However, it is again the outer layers that define the total energy distribution.

An "intermediate" case at which the electron distribution follows different solution in the inner and outer layers can of course occur, as shown in fig. 6.9. This depends purely on the critical parameter z_* in combination with the size z_1 of the jet. z_* varies however slowly with the ϖ coordinate and thus the range of the parameters that such a total distribution may arise is limited. Moreover, this case does not show much difference from the electron distribution that arises from eq. 6.22 and thus will not be discussed further.

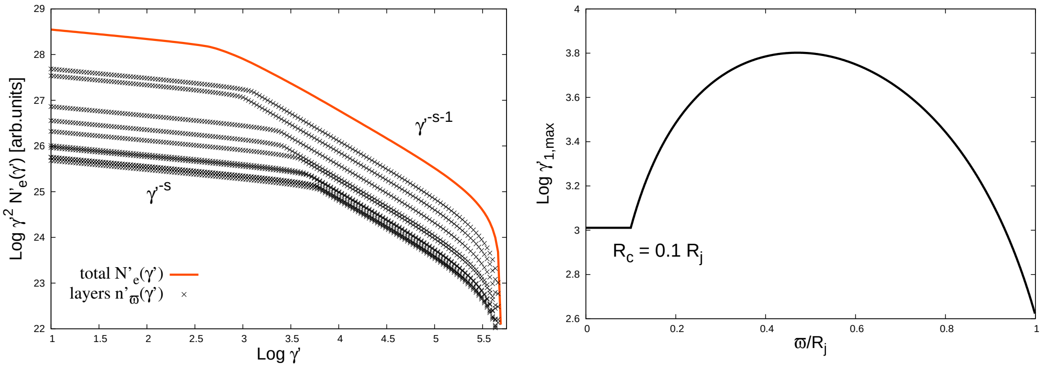

Figure 6.7: (a) Electron energy distribution emerging from the jet. The values of the main parameters are $B = 2\ G$, $R_c = 0.1\ R_j$, $s = 2.2$. The value of the minimum injected cutoff is $\gamma'_{0,min} = 10$ and $z_1 = 10^{17} cm$. The outer layers dominate the resulting total distribution. The electron distribution from each layer follows the solution (6.20). (b) Variation of the cooling break energy $\gamma'_{1,max}$ along the jet.

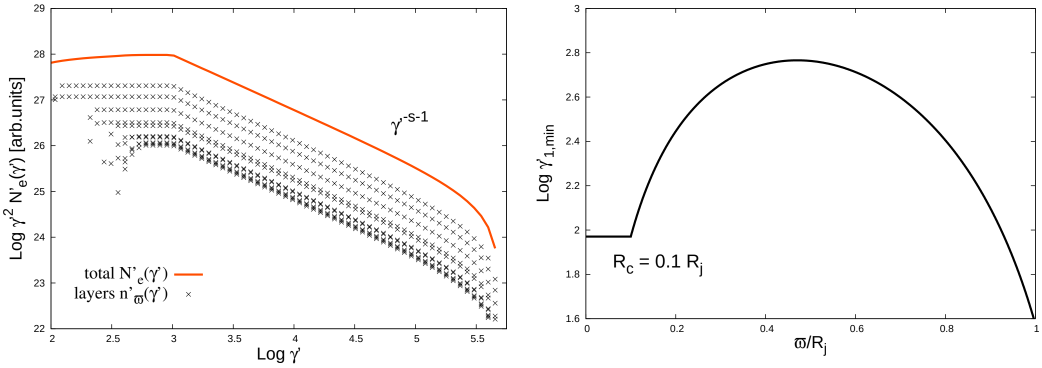

Figure 6.8: (a) Same as in fig. 6.7 but here the electron distribution from each layer follows the solution (6.22). The cooling break is at $\gamma'_{0,min}$ and thus constant in respect to ϖ. The minimum cutoff however is different for each layer and thus the total distribution below $\gamma'_{0,min}$ is slightly harder than the expected γ'^{-2} slope that characterizes each layer. Here we have used a larger value for the injected minimum cutoff, $\gamma'_{0,min} = 10^3$, to demonstrate better the behavior of the total distribution. The total size of the jet is $z_1 = 10^{18} cm$. (b) The minimum cutoff energy dependance on ϖ. As for $\gamma'_{1,max}$, this is not a monotonic function of ϖ along the jet.

Though the total electron distribution is dominated by the outer layers, the synchrotron emission may differ due to the stronger boosting of the core radiation. Apart from this enhancement due to the beaming, one may as well explore different reason for enhancing some of the jet components, e.g. by varying the free parameters of the model like the core size R_c or the boundary values of the Lorentz factor. The main purpose is to examine whether a "mixing" of the radiated components can

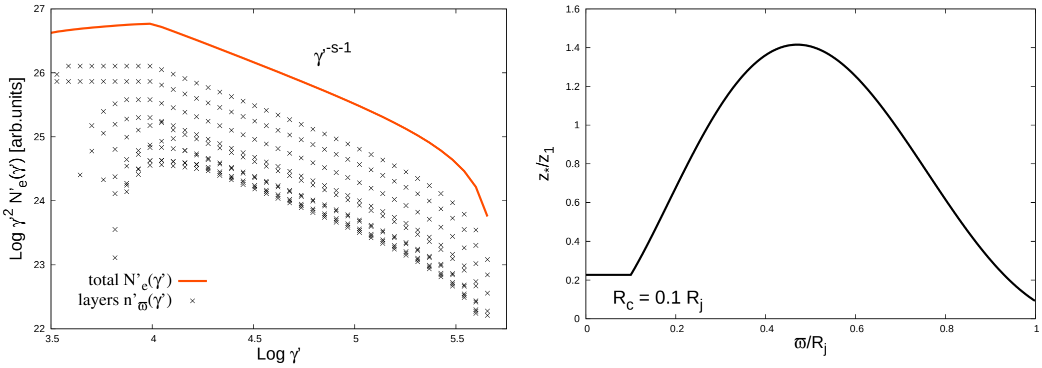

Figure 6.9: Same as figure 6.8 but for $\gamma'_{0,min} = 10^4$ and $z_1 = 4\ 10^{16} cm$ so that the electron distribution follows different solution at the outer and inner layers. At the right panel it is shown how the critical length scale z_* varies in respect to ϖ.

occur and thus lead to spectral signatures of the jet stratification. These special features should be prominent to appear close to the breaks of the distribution, i.e. around $\gamma'_{1,max}$ in the first case and around $\gamma'_{0,min}$ in the second case. Apart from the aforementioned modifications, it is also interesting to examine whether the spectra appear different in shape under different angles of observation or for different values of the free parameters.

The observed synchrotron spectrum that arises from the sum of the distributions plotted in fig. 6.7 (left panel) is shown in fig. 6.10 for $R_c = 0.1\ R_j$ and $R_c = 0.5\ R_j$ respectively. The spectral break should occur at the synchrotron frequency that corresponds to $\gamma'_{1,max}$, namely at

$$\nu_{1,max} \propto D(\varpi)B(\varpi)\gamma'^2_{1,max} \propto D(\varpi)\Gamma(\varpi)^5\varpi^3\beta(\varpi)^2. \tag{6.44}$$

This is as well a non-monotonic function of ϖ for $R_c = 0.1\ R_j$, but for a much larger core size it decreases towards the edge of the jet (see fig. 6.11). When considering a thin inner spine the total spectrum is dominated by the inner layers radiation and the typical break of $\alpha \sim 0.5$ appears. For a larger core, the outer layers start to "appear" at the observed spectrum and the break occurs at smaller energies. Although one may expect the core jet radiation to become stronger as we increase the size of the core, the opposite situation occurs. The reason concerns the magnetic field' s functional dependance on ϖ that we have assumed. As R_c increases, the magnetic field takes larger values close to the edge of the jet, enhancing this way the synchrotron radiation of these components.

This is a special case related to the stratification of the number density of the injected electrons. In principle, we can roughly estimate the synchrotron power by

$$P_{syn} \propto \frac{dE}{dt}_{syn} N_{total}, \tag{6.45}$$

where N_{total} the number of electrons (integrated over energy). In a self-consistent treatment, the steady-state electron distribution is inverse proportional to the energy losses (look e.g. the solutions 6.20 and 6.22) and thus the synchrotron power should not depend strongly on the magnetic field. However, in our case it turns out that $k'_{0,\varpi} \propto B'(\varpi)^2$ and due to this modification the components of the jet with larger magnetic field radiate higher synchrotron flux.

Coming back to the spectrum for a core with $R_C = 0.5R_j$, we can see that there is an energy band for which the contribution of the various components mix and thus the slope is somewhat smaller that $\nu'^{-s/2}$. Actually the spectral slope in this energy band, which ranges from the "minimum" (with respect to ϖ) to the "maximum" $\gamma'_{1,max}$, is gradually decreasing from $\nu'^{-(s-1)/2}$ to $\nu'^{-s/2}$ as we consider larger sizes for the central spine of the jet (see fig. 6.13). This is a direct effect of the stratification of the jet. It does not only show that different jet parameters can lead to different spectra, but it also results in a modification of the spectrum with respect to the homogeneous, 1-zone models. Interestingly, the aforementioned energy band, when this becomes evident, is not small (slightly more than two orders of magnitude for the specific parametrization). It is strongly correlated with the parametrization that we have chosen, but it can appear in other configurations as well, because the only presupposition regards the mixing of the layers radiation. The demand to have different $\nu_{1,max}$ for different layers is satisfied by default in a stratified flow due to the cooling process of the particles. Obviously, the more the values of these frequencies deviate from each other, the more evident is the effect. Note that in the synchrotron self-Compton part of the spectrum (in the Thomson regime), this energy band becomes substantially larger due to the emission mechanism itself, as $\nu^c \propto DB'\gamma'^4$.

Even more interestingly, a similar modification can be attributed to different angles of observation and be linked to purely phenomenological reasons. Larger angles of observation enhance the outer components of the jet and, as shown in fig. 6.13, the spectrum becomes softer with increasing angle θ. This means that if we observe at this energy band a source with stratification, the slope will change with the angle of observation and can take any value between $s/2$ and $(s-1)/2$. Additionally, one can see, as before, that for some values of the angle θ, a second break appears in the spectrum (e.g. for $\theta = 4^o - 5^o$).

When the electron distribution from each layer is given by eq. 6.22, the spectral break does not vary so significantly with the polar radius as it occurs at the frequency that corresponds to the electron energy $\gamma_{0,min}$, which is constant and thus

$$\nu_{0,min} \propto D(\varpi)B(\varpi)'\gamma'_{0,min} \propto \frac{D(\varpi)}{\varpi\Gamma(\varpi)}. \tag{6.46}$$

For this reason any possible modification is expected close to the low energy cutoff $\gamma'_{1,min}$. This concerns however very low frequencies and is not so interesting as in the previous case. Nevertheless, a similar behavior is observed (see fig. 6.13). As we increase the core size or the angle θ, the outer layers start to contribute at the emitted spectrum. The slope at low energies then varies from 1/3 to $-1/2$ and as before it can take any value in between. The energy band at which modification due to the flow stratification occurs concerns all the frequencies below $\gamma'_{0,min}$. Thus, it is distinguishable only for injected electron distribution with relatively high values for the lower cutoff, like $\gamma'_{0,min} \sim 10^3$, as we have used in the fig. 6.12. It can thus be relevant for applications where a high $\gamma'_{0,min}$ is assumed, like in the leptonic modeling of hard spectrum sources that we discussed in chapter 2.

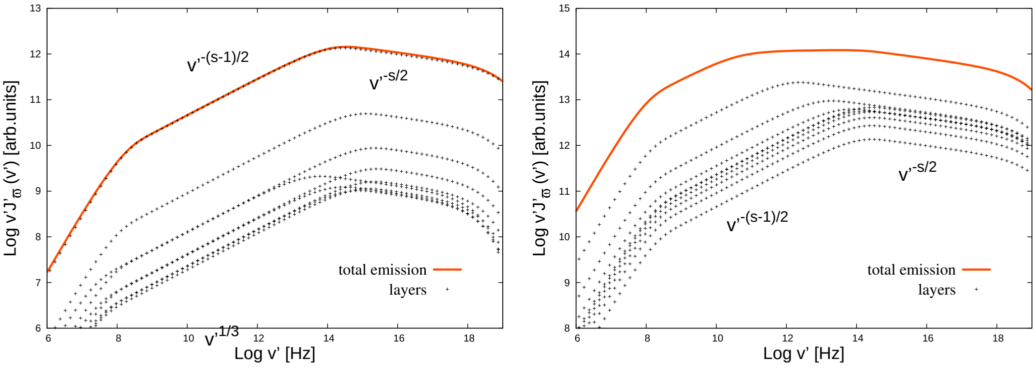

Figure 6.10: Observed synchrotron flux for two different core sizes, $R_c = 0.1\ R_j$ (left panel) and $R_c = 0.5\ R_j$ (right panel) for the electron distribution of eq. 6.20. When the core size is small the inner layers dominate the emission whereas for larger R_c, the outer layers play significant role at the total observed spectrum.

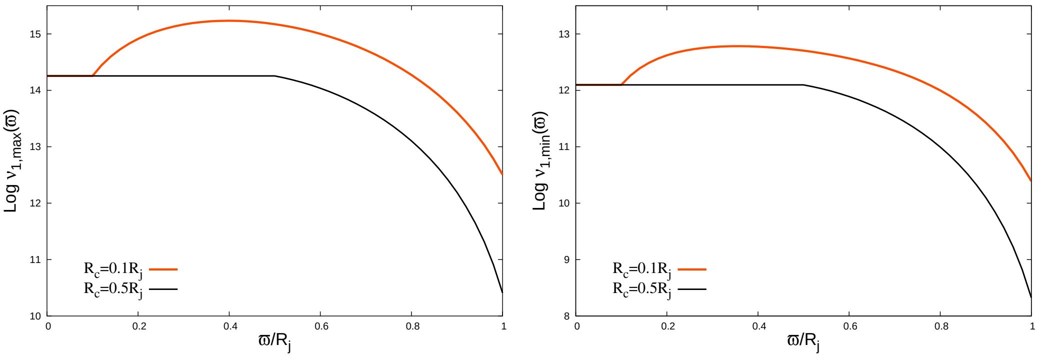

Figure 6.11: Variation of the spectral breaks $\nu_{1,max}$ and $\nu_{1,min}$ along the jet for two different sizes of the core.

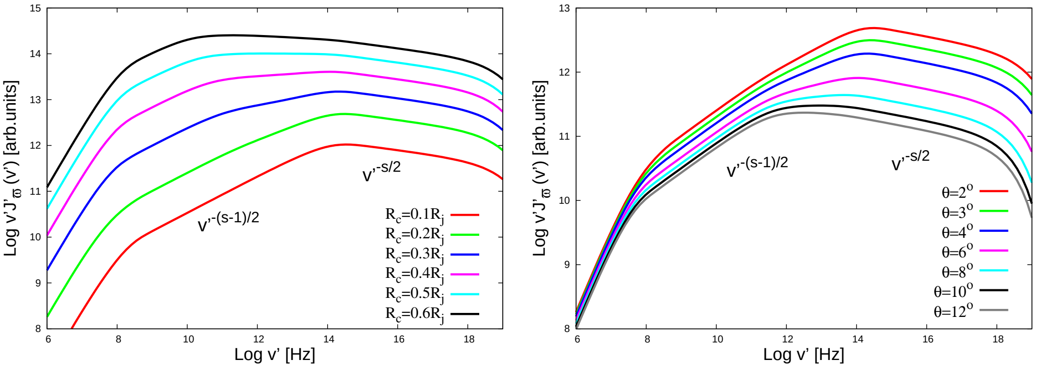

Figure 6.12: Synchrotron spectra for (a) different core sizes but the same angle of observation ($\theta = 2^o$) and (b) different angles but the same core size ($R_c = 0.2\ R_j$). The parent electrons follow the solution of eq. 6.22. For low R_c or θ the inner layers dominate the emission. Increasing these parameters results in a gradual appearance of the outer layers, leading to special features in the spectrum, in the energy band around $\nu_{1,max}$. The spectrum becomes gradually softer with increasing R_c or θ and for some specific values we can see a second break appearing at the "minimum" in respect to ϖ characteristic frequency $\nu_{1,min}(\varpi)$, e.g. for $R_c = 0.3 - 0.5\ R_j$ or $\theta = 4^o - 8^o$

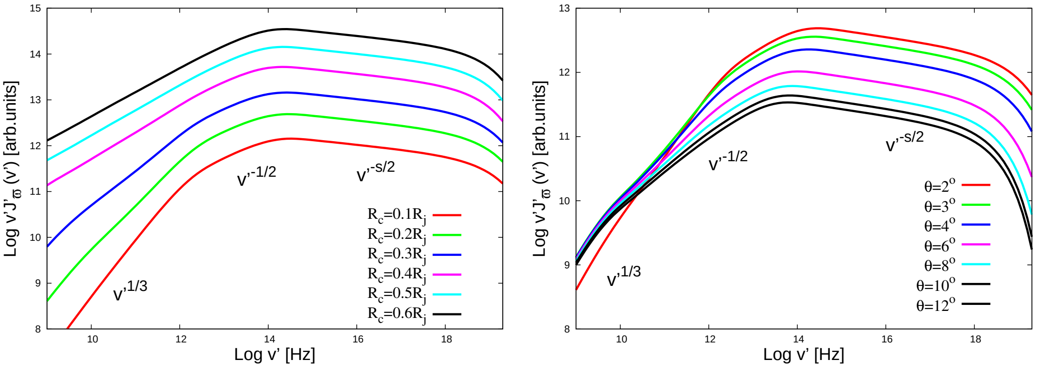

Figure 6.13: Same as in fig. 6.12 but for parent electron distributions of eq. 6.22. The modification in respect to the homogeneous case occurs below the frequency that corresponds to $\gamma'_{0,min}$ and it is relevant only at low energies.

6.6 Effects of the maximum energy of the injected electron distribution

One point that has not been discussed yet, is whether a transverse scaling of the maximum injected electron energy $\gamma'_{0,max}$ may result in further modification of the observed spectrum. As discussed earlier, even if the total electron distribution exhibits some features at high energies, the synchrotron spectrum does not strongly reflect these differences. This is true only if the variation of the $\gamma'_{0,max}$ along the jet comes from the magnetic field stratification. Of course the observed maximum cutoff will be different for each layer due to the Doppler boosting, but the smooth synchrotron cutoff does not allow for any important modification appear. Nevertheless, if we consider that an additional scaling comes into play e.g. through the shock velocity, the possibility for some alteration of the emitted flux is higher. In any case, varying more of the physical parameters and/or in more ways of the bulk flow or the relativistic particles is the next step.

Let as examine e.g. the aforementioned case at which the shock velocity scales as the bulk flow, a parametrization justified by the fact that the velocity of the standing shock that is created is not arbitrary but it is formulated by the velocities in the upstream and downstream region. Thus if $V_s = V_s(\varpi) \propto \beta(\varpi)$, the maximum cutoff given in eq. 6.38 reads

$$\gamma'_{0,max} \propto \frac{\Gamma(\varpi)}{\sqrt{B'(\varpi)}} \propto \varpi\Gamma(\varpi)^2. \tag{6.47}$$

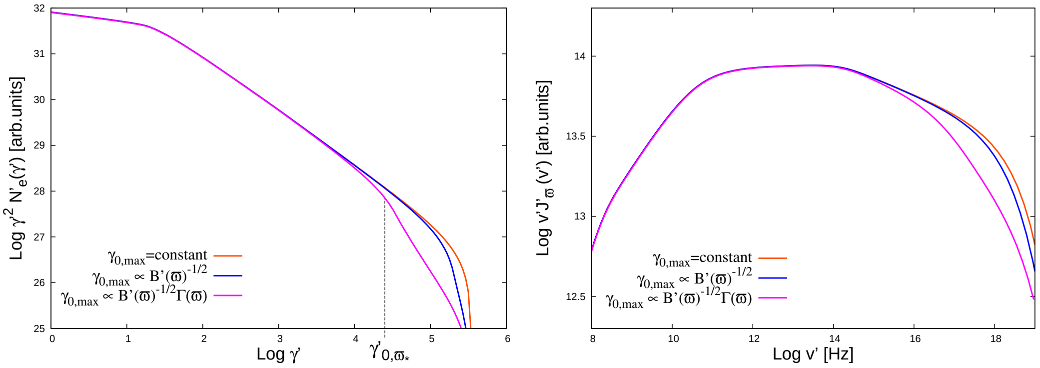

Figure 6.14: Parent electron distributions for different dependance of $\gamma'_{0,max}$ on ϖ. When the maximum cutoff energy depends on the magnetic field little difference manifests at the total energy distribution, whereas an additional dependance on ϖ is assumed (due to e.g. a non-constant along the jet shock velocity) the total energy distribution at high energies exhibits a steepening. This results in a -smother than exponential- tail at the high energy part of the spectrum. This is why the spectrum at these energies does not exhibit a clear power-law behavior but is rather curved. Note that this holds for $R_c = 0.5R_j$, a case where the total emission comes from a mixing of the layers.

Again, the values for the free parameters are to define whether some features will appear at the spectrum due to the mixing of the inner and outer layers of the jet. At fig. 6.14 the total electron energy distribution and the observed synchrotron spectrum is shown for $R_c = 0.5R_j$. Three cases are plotted. A constant $\gamma'_{0,max}$, a dependance only on the magnetic field according to eq. (6.38) and additional dependance on ϖ due to the stratification of the shock velocity (eq. 6.47). When the maximum injected energy depends only on the magnetic field little modification is observed in respect to the $\gamma'_{0,max} = constant$ case. On the other hand, for eq. 6.47 both electrons and synchrotron radiation are altered at high energies. The resulting particle distribution becomes steeper, around the minimum -in respect to ϖ- injected energy $\gamma'_{0,\varpi *}$. The observed spectrum is steeper as well, but smoother than the exponential cutoff. In total it looks rather curved and does not have a clear power-law behavior.

6.7 Summary and future work on stratified outflows

In this last chapter we have developed a non-homogeneous model for radiation from relativistic outflows. We discussed only the synchrotron radiation component of the spectrum, neglecting the ICS component and the corresponding energy losses. Such a scheme allows as to examine in detail the effects of stratification, as we can develop an analytic solution for the electron distribution in each layer. We have shown that even in this simplified picture, important deviation from the one zone models may appear. Two effects exhibit the underlying stratification. First, the observed synchrotron spectrum appears different for different values (of some) of the free parameters of the model, e.g. the size of the central core or the angle of observation. The main reason concerns the dominance of different layers each time. As far as the viewing angles is concerned, this means that intrinsically identical jets appear different for different angles, an effect that has been previously discussed in more simplified cases like the spine-layer model of Ghisellini et al. (2005).

Secondly, we have shown that a mixing of the emission of the layers may occur, leading to interesting features of the spectrum. Within an energy band which (for the parameters chosen here) extends for ~ 2 orders of magnitude, the slope of the spectrum can take any value between $-s/2$ and $-(s+1)/2$ and it depends purely on the stratification of the physical parameters. Furthermore, the observed spectrum may show a second break which is an observational evidence for a stratified flow, as it is not expected for homogeneous models. This happens when the injected electron distribution has a relatively low minimum cutoff ($\gamma'_{0,min} \sim 10$) and the particles do not completely cool before they escape at the edge of the jet. When the injected cutoff is higher so that the local electron distribution from each layer exhibit the characteristic $\propto \gamma'^{-2}$ behavior, modification analog to the aforementioned is observed at the low energy part of the spectrum. The slope takes arbitrary values among 1/3 and -0.5, but no break shows up.

One may then conclude that even within this simplified scheme, a modification of the spectrum is expected and may potentially explain spectral features that the homogeneous models fail to interpret. Thus, further development by including the ICS component is desired, as these modification may either be enhanced or smoothed out. In both cases evidence for stratification is strong as normally the two components of the spectrum are assumed to be similar, i.e. exhibit roughly the same power-law slope. Deviation from the standard assumptions usually made, homogeneity and/or isotropy can be proved significant for explaining peculiar features of the radiated spectra within leptonic models and without extreme phenomenological assumptions. Additionally, the possible stratification of a relativistic outflow is closely related to the MHD processes that take place and thus its manifestation through the emission mechanisms provides an interesting tool for testing or comparing current theoretical models.

Chapter 7

Conclusions

In this thesis we have investigated the leptonic radiation processes that take place in the relativistic outflows of AGN. We have developed a self-consistent approach shedding light on a number of unsolved problems regarding the interpretation of the observed spectra, and we have expanded current models in order to examine more complex, non-homogeneous configurations. Furthermore, we have analyzed in detail issues related to the spectral shape of the emitted radiation.

One major topic in AGN physics that has attracted attention over the last years is the interpretation of the hard VHE Blazar spectra. After correction for EBL interaction of the emitted TeV photons, the intrinsic spectra of some sources appear particularly hard, possessing challenges to standard leptonic models. In *chapter 2* we have discussed the capability of narrow electron distributions to explain such hard spectra. We have shown that these distributions within a self-consistent, time dependent treatment, can lead to the formation of hard spectra. A power-law with a large value of the low-energy cutoff can be maintained in the presence of energy losses if adiabatic losses due to the expansion of the source control the evolution of electrons at low energies. Furthermore, stochastic acceleration of particles in combination with radiation losses, naturally leads to the formation of relativistic Maxwell-type distributions which can successfully explain even extremely hard VHE Blazar spectra.

Interestingly, narrow particle distributions such as Maxwellian type distributions can account for broader spectra as well, once they are embedded in a non-homogeneous, multi-zone scenario. In *chapter 3* we have developed a phenomenological model in which the emitted Blazar spectra originates from several regions (blobs), where electrons are stochastically accelerated to relativistic energies. The resultant emission can lead to power-law like spectra, with index simply controlled by the energetics of the blobs. In this scheme, if one (or few) of the blobs become more energetic (due to either an increase of the injected energy or an enhancement of the Doppler boosting), hard flaring events can be satisfactorily interpreted. In particular, such "leading blob" scenario can account for the characteristic Mkn 501 flare in 2009 during which a strong spectral hardening was observed.

The radiated spectra in the aforementioned cases (and in general in the literature) are calculated numerically. The kernel functions of the synchrotron and

Compton processes are complex and the full convolution with the particle distribution can not be handled analytically. However, analytical approximations are very important, as they give a helpful insight into the underlying physics, especially the acceleration of the particles. In *chapter 4* we develop analytical approximations that describe the shape of the Compton spectrum close to the high-energy cutoff. The high-energy cutoff of the electron distribution carries crucial information of the acceleration process and can be used to distinguish among current theories. Our calculations provide a direct link between the parent electrons and the emitted spectrum. Additionally, we can draw some general conclusions. For example, we show that the shape of the two components of the observed spectrum (the low energy, synchrotron bump and the high energy Compton bump) are not always identical. In particular, in the Thomson regime the cutoff shape depends strongly on the target photon field, and is rather broad, which is not the case in the Klein-Nishina regime where the spectral cutoff resembles the shape of the electron distribution and is more sharp.

The calculation of the observed Blazar spectra are essentially related to the Doppler boosting of the emitted radiation. Blazars are known to exhibit relativistic jets and the relativistic motion can lead to an important enhancement of the intrinsic luminosity. Interestingly, the beaming pattern depends on the emission process, e.g. it is different for the synchrotron/SSC and EC model. In *chapter 5* we solve the photon transfer equation in order to obtain the formulas that describe the Doppler boosting for general electron distributions, non-homogeneous, anisotropic and stationary. These calculations generalize the results previously obtained in the literature. Furthermore, they allow us to examine the interesting case of anisotropic particle distributions that are often predicted in acceleration theories. We show that the anisotropy of the radiating particles may lead to a possible mis-estimation of the Doppler factor, as the luminosity peaks at viewing angles different than in the case of isotropic models. Under the natural assumption that the degree of anisotropy depends on the energy of the particles, we show that the emitted synchrotron spectrum may appear harder. This effect is even more evident in the EC component and in total anisotropy can introduce modification of these two components.

In principle, relaxing standard assumptions, i.e. anisotropy or homogeneity of the emitting source, has important consequences for understanding peculiar features of the observed spectra. We have seen in *chapter 3* that within a phenomenological non-homogeneous model, hard flaring events can be interpreted under certain assumption. We have also shown in *chapter 5* that the emitted spectral shape can differ substantially from the case of isotropic particles and thus it can account for spectra that the same power-law distributions can not explain in the isotropic case. In *chapter 6* we examine a non-homogeneous model in which the parameters of the source vary continuously, as inferred from MHD simulations. In particular, we develop a self-consistent approach for the synchrotron radiation that emerges from a stratified jet. The stratification arises in the transverse (to the fluid velocity) direction and it concerns several physical parameters, such as the bulk Lorentz factor, the magnetic field, the energy density of the parent electrons as well as the value of the maximum cutoff of the particle distribution. In our scheme, the relativistic electrons are assumed to be injected in the radiation zone at the base of the jet. We show that such a stratification may lead to interesting differences with respect to homogeneous models. First of all, as discussed before in more simplified inhomogeneous models, the spectrum may appear different for different viewing angles. Secondly, the observed spectrum can exhibit special features related to the stratification. For example, an additional break in the SED, which is related to the cooling break that the particle distribution exhibits in each layer. The stratification may be as well revealed through the spectral slope of a part of the spectrum, which is not related to the acceleration process, but depends on the assumed relations that describe the parameters' stratification.

The noted time-dependent approaches, as well as the deviation from standard assumptions, such as isotropy and homogeneity, offer important insight for the non-thermal emission from AGN jets and allow to successfully address a number of unsolved problems. Leptonic models have more to reveal for the AGN physics than often assumed.

Bibliography

Abdo, A.A. et al. 2011, ApJ, 727, 129

Aharonian, F.A. 2000, NewA, 5, 377

Aharonian, F., Akhperjanian, A. G., Barres de Almeida, U., et al. 2007, A&A, 473, L25

Aharonian, F., Akhperjanian, A. G., Bazer-Bachi, A. R., et al. 2007, ApJL, 664, L71

Aharonian, F. A., & Ambartsumyan, A. S. 1985, Astrophysics, 23, 650

Aharonian F. A. & Atoyan, A. M. 1981, Ap&SS, 79, 321

Aharonian, F.A., Atoyan, A. M., & Nahapetian, A. 1986, A&A, 162, L1

Aharonian, F. A., Kelner, S. R. & Prosekin, A. Yu. 2010, PhRvD, 82d 3002A

Aharonian, F.A., Khangulyan, D., & Costamante, L. 2008, MNRAS, 387, 1206

Aharonian, F.A., Timokhin, A.N., & Plyasheshnikov, A.V. 2002, A&A, 384, 834

Aharonian, F., et al. 2006, Nature, 440, 1081

Aharonian, F., et al. 2007, A&A, 475, L9

Aharonian, F., Akhperjanian, A. G., Bazer-Bachi, A. R., et al. 2007, ApJL, 664, L71

Aharonian, F., et al., 2007a, A&A, 470, 475

Aharonian, F., et al., 2007b, A&A, 475, L9

Albert, J., Aliu, E., Anderhub, H., et al. 2007, ApJ, 669, 862

Aleksić, J., Antonelli, L. A., Antoranz, P., et al. 2011, A&A, 530, A4

Alfvén, H., & Herlofson, N. 1950, Physical Review, 78, 616

Aloy, M.-A., Gomez, J.-L., Ibanez, J.-M., Marti, J.-M., Muller, E. 2000, ApJL, 528, L85

Aloy, M. A., & Mimica, P. 2008, ApJ, 681, 84

Antonucci, R. 1993, ARA & A, 31, 473

Appl, S., & Camenzind, M. 1993, A&A, 274, 699

Atoyan A. M., & Aharonian F. A. 1999, MNRAS, 302, 253

Attridge, J. M., Roberts, D. H., & Wardle, J. F. C. 1999, ApJL, 518, L87

Axford, W. I., Leer, E., & Skadron, G. 1978, Cosmophysics, 125

Becker, P. A., Das, S., & Le, T. 2008, ApJL, 677, L93

Bednarek, W., Kirk, J. G., & Mastichiadis, A. 1996, A&A, 307, L17

Begelman, M.C., Blandford, R.D., & Rees, M.J. 1984, Reviews of Modern Physics, 56, 255

Bell, A. R. 1978, MNRAS, 182, 443

Blandford, R. D., & Levinson, A. 1995, ApJ, 441, 79

Blandford, R. D., & Ostriker, J. P. 1978, ApJL, 221, L29

Blandford, R. D., & Payne, D. G. 1982, MNRAS, 199, 883

Blandford, R. D., & Rees, M. J. 1974, MNRAS, 169, 395

Blandford, R. D., & Znajek, R. L. 1977, MNRAS, 179, 433

Bloom, S.D. & Marscher A.P. 1996, ApJ, 461, 657

Blumenthal, G. R. 1971, Phys. Rev. D, 3, 2308.

Blumenthal, G. R., & Gould, R. J. 1970, Reviews of Modern Physics, 42, 237

Boettcher, M. 2012, arXiv:1205.0539

Böttcher, M., Dermer, C.D., & Finke, J.D. 2008, ApJ, 679, L9

Brunetti, G. 2000, Astropart. Phys., 13, 107

Celotti, A., & Blandford, R. D. 2001, Black Holes in Binaries and Galactic Nuclei, 206

Cerutti, B., Werner, G. R., Uzdensky, D. A., & Begelman, M. C. 2012, arXiv:1205.3210

Chiaberge, M., Celotti, A., Capetti, A., & Ghisellini, G. 2000, A& A, 358, 104

Coppi, P. S. & Blandford, R. D. 1990, MNRAS., 245, 453

Costamante, L. 2012, IAU Symposium, 284, 420

Crusius, A., & Schlickeiser, R. 1986, A&A, 164, L16

De Angelis, A., Mansutti, O., Persic, M., & Roncadelli, M. 2009, MNRAS, 394, L21

Derishev, E. V. 2007, Ap&SS, 309, 157

Derishev, E.V., Aharonian, F.A., Kocharovsky, V.V., Kocharovsky, Vl. V. 2003, Phys. Rev. D, 68, 043003

Derishev, E. V., Aharonian, F. A., & Kocharovsky, V. V. 2007, ApJ, 655, 980

Dermer, C. D. 1995, ApJL, 446, L63

Dermer, C. D., & Atoyan, A. M. 2002, ApJ, 568, L81

Dermer, C. D., Schlickeiser, R., & Mastichiadis, A. 1992, A&A, 256, L27

Dermer, C. D., & Schlickeiser, R. 1993, ApJ, 416, 458

Dempsey, P., & Duffy, P. 2007, MNRAS, 378, 625

Dominguez, A., Primack, J. R., Rosario, D. J., et al. 2010, MNRAS, 410, 2556

Domínguez, A., Primack, J. R., Rosario, D. J., et al. 2011, MNRAS, 410, 2556

Eilek, J. A., & Arendt, P. N. 1996, ApJ, 457, 150

Eilek, J. A., Melrose, D. B., & Walker, M. A. 1997, ApJ, 483, 282

Epstein, R. I. 1973, ApJ, 183, 593

Epstein, R. I., & Petrosian, V. 1973, ApJ, 183, 611

Essey, W., & Kusenko, A. 2012, ApJL, 751, L11

Essey, W., & Kusenko, A. 2010, Astroparticle Physics, 33, 81

Essey, W., Kalashev, O. E., Kusenko, A., & Beacom, J. F. 2010, Physical Review Letters, 104, 141102

Essey, W., Kalashev, O., Kusenko, A., & Beacom, J. F. 2011 ApJ, 731 51E

Fermi, E. 1949, Physical Review, 75, 1169

Fermi, E. 1954, ApJ, 119, 1

Franceschini, A., Rodigliero, G., & Vaccari, M. 2008, A&A, 487, 837

Frank J., King A., Raine D., 1995, Accretion Power in Astrophysics, (second edition), Cambridge Univ. Press: Cambridge

Fritz, K.D. 1989, A&A, 214, 14

Georganopoulos, M., & Kazanas, D. 2003, ApJL, 594, L27

Georganopoulos, M., Kirk, J.G., & Mastichiadis, A. 2001, ApJ, 561, 111

Ghisellini, G., Tavecchio, F., & Chiaberge, M. 2005, A&A, 432, 401

Giebels, B., Dubus, G., & Khélifi, B. 2007, A&A, 462, 29

Gilmore, R. C., Somerville, R. S., Primack, J. R., & Domínguez, A. 2012, MNRAS, 422, 3189

Giovannini, G., Cotton, W. D., Feretti, L., Lara, L., & Venturi, T. 1998, arXiv:astro-ph/9808261

Giovannini, G., Cotton, W. D., Feretti, L., Lara, L., & Venturi, T. 1999, MmSAI, 70, 161

Giovannini, G., Cotton, W. D., Feretti, L., Lara, L., & Venturi, T. 2001, ApJ, 552, 508

Gomez, J. L., Marti, J. M. A., Marscher, A. P., Ibanez, J. M. A., & Marcaide, J. M. 1995, ApJL, 449, L19

Gould, R.J., & Schreder, G.P. 1967, Physical Review, 155, 1408

Gracia, J., Vlahakis, N., Agudo, I., Tsinganos, K., & Bogovalov, S. V. 2009, ApJ, 695, 503

Hardcastle, M. J., Alexander, P., Pooley, G. G., & Riley, J. M. 1997, MNRAS, 288, L1

Hauser, M. G., & Dwek, E. 2001, ARA&A, 39, 249

Henri, G., & Pelletier, G. 1991, ApJL, 383, L7

Hooper, D., & Serpico, P. D. 2007, Physical Review Letters, 99, 231102

Jackson, J. D. 1975, 92/12/31, New York: Wiley, 1975, 2nd ed.,

Jones, F.C. 1968, Phys.Rev., 167, 1159

Jones, T. W., O'dell, S. L., & Stein, W. A. 1974, ApJ, 188, 353

Kahn, F. D. 1983, MNRAS, 202, 553

Katz-Stone, D. M., & Rudnick, L. 1994, ApJ, 426, 116

Kardashev, N. S. 1962, SvA, 6, 317

Katarzyński, K., Ghisellini, G., Tavecchio, F., Gracia, J., & Maraschi, L. 2006, MNRAS, 368, L52

Khangulyan, D. & Aharonian, F. 2005, AIPC 745, 359K

Kifune, T. 1999, ApJL, 518, L21

King, A. 2012, arXiv:1201.2060

Kneiske, T. M., Bretz, T., Mannheim, K., & Hartmann, D. H. 2004, A&A, 413, 807

Krawczynski, H., Coppi, C.S., & Aharonian, F. 2002, MNRAS, 336, 721

Komissarov, S. S. 1990, Soviet Astronomy Letters, 16, 284

Komissarov, S. S., Barkov, M. V., Vlahakis, N., Königl, A. 2007, MNRAS, 380, 51

Krymskii G.F., 1977, Akademiia Nauk SSSR, Doklady 234, 1306

Kusunose, M., & Takahara, F. 2005, ApJ, 621, 285

Laing, R. A. 1996, Energy Transport in Radio Galaxies and Quasars, 100, 241

Laing, R. A., Canvin, J. R., Cotton, W. D., & Bridle, A. H. 2006, MNRAS, 368, 48

Laing, R. A., Canvin, J. R., Bridle, A. H., & Hardcastle, M. J. 2006, MNRAS, 372, 510

Laing, R. A., Parma, P., de Ruiter, H. R., & Fanti, R. 1999, MNRAS, 306, 513

Laing, R. A., & Bridle, A. H. 2002, MNRAS, 336, 328

Laing, R. A., Canvin, J. R., & Bridle, A. H. 2006, Astronomische Nachrichten, 327, 523

Lazarian, A., Kowal, G., Pino, B. G. d., & Vishniac, E. T. 2012, Multi-scale Dynamical Processes in Space and Astrophysical Plasmas, 11

Lefa, E., Rieger, F. M., & Aharonian, F. 2011, ApJ, 740, 64

Lefa, E., Aharonian, F. A., & Rieger, F. M. 2011, ApJL, 743, L19

Lefa, E., Kelner, S. R., & Aharonian, F. A. 2012, ApJ, 753, 176

Lenain, J.-P., Boisson, C., Sol, H. & Katarzyński, K., 2008, A&A 478, 111

Li, H.-Q., Wang, J.-C., & Xue, L. 2004, ChJaa, 4, 311

Li, H., & Wang, J. 2004, ApJ, 617, 162

Lind, K. R., & Blandford, R. D. 1985, ApJ, 295, 358

Longair, M. S. 2010, High Energy Astrophysics by Malcolm S. Longair. Cambridge University Press, 2010. ISBN: 9780521756181,

Lovelace, R. V. E. 1976, Nature, 262, 649

Lynden-Bell, D. 1978, *Phys. Scripta*, 17, 185

Madejski, G. M. 1999, arXiv:astro-ph/9903141

Mannheim, K. 1993, A&A, 269, 67

Mannheim, K., & Biermann, P. L. 1992, A&A, 253, L21

Mandal, S., & Chakrabarti, S. K. 2008, ApJL, 689, L17

Massaro, E., Tramacere, A., Perri, M., Giommi, P., & Tosti, G. 2006, A&A, 448, 861

Maraschi, L., Ghisellini, G., & Celotti, A. 1992, ApJL, 397, L5

Medvedev, M. V. 2006, ApJ, 637, 869

Melrose, D. B. 1980, Plasma astrophysics: Nonthermal processes in diffuse magnetized plasmas, Astrophysical applications (New York, Gordon and Breach Science Publishers), 2, 430

Moderski, R., Sikora, M., Coppi, P. S., & Aharonian, F. 2005, MNRAS 363, 954

Morrison, P., Sadun, A., & Roberts, D. 1984, ApJ, 280, 483

Narginen D. I. & Putanen, J. 1993, A&A, 275, 325

Neronov, A., Semikoz, D., & Taylor, A. M. 2012, A&A, 541, A31

Owen, F. N., Hardee, P. E., & Cornwell, T. J. 1989, ApJ, 340, 698

Padovani, P. 1999, Vulcano Workshop 1998: Frontier Objects in Astrophysics and Particle Physics, 159

Perlman, E. S., Biretta, J. A., Zhou, F., Sparks, W. B., & Macchetto, F. D. 1999, AJ, 117, 2185

Petrosian, V. 2012, Space Sci. Rev., 49

Phinney, E. S. 1982, MNRAS, 198, 1109

Primack, J. R. et al. 2011, Proc. of the 25th Texas Symposium (eds. F.A. Aharonian, W. Hofmann, F.M. Rieger), AIP Conf. Proc. 1381, in press (arXiv:1107.2566)

Protheroe, R. J. 1997, IAU Colloq. 163: Accretion Phenomena and Related Outflows, 121, 585

Perucho, M., & Martí, J. M. 2007, MNRAS, 382, 526

Piran, T. 1982, ApJL, 257, L23

Poutanen, J., & Vurm, I. 2010, ApJS, 189, 286

Prosekin, A., Essey, W., Kusenko, A., & Aharonian, F. 2012, arXiv:1203.3787

Rees, M. J. 1966, Nature, 211, 468

Reid, M. J., Biretta, J. A., Junor, W., Muxlow, T. W. B., Spencer, R. E. 1989ApJ, 336, 112R

Reville, B., & Kirk, J. G. 2010, ApJ, 724, 1283

Rieger, F.M. 2004, ApJ, 615, L5

Rieger, F.M., Bosch-Ramon, V., & Duffy, P. 2007, Ap&SS, 309, 119

Rieger, F. M., & Duffy, P. 2004, ApJ, 617, 155

Ruffini, R., & Wilson, J. R. 1975, Phys. Rev. D, 12, 2959

Rybicki, G. B., & Lightman, A. P. 1979, Radiative Processes in Astrophysics (New York: Wiley)

Salpeter, E. E. 1964, ApJ, 140, 796

Saugé, L., & Henri, G. 2006, A&A, 454, L1

Sauty, C., Tsinganos, K., & Trussoni, E. 2002, Relativistic Flows in Astrophysics, 589, 41

Sazonov S. Y. & Sunyaev, R. A. 2000, ApJ, 543, 28

Schlickeiser, R. 1985, A&A, 143, 431

Schmidt M., 1963, Nature 197, 1040

Shakura, N. I., & Sunyaev, R. A. 1973, A&A, 24, 337

Sikora, M., Begelman, M. C., & Rees, M. J. 1994, ApJ, 421, 153

Sikora, M., Blazejowski, M., Moderski, R., & Madejski, G. M. 2002, ApJ, 577, 78

Sikora, M., Madejski, G., Moderski, R., & Poutanen, J. 1997, ApJ, 484, 108

Sikora, M., Sol, H., Begelman, M. C., & Madejski, G. M. 1996, MNRAS, 280, 781

Skilling, J. 1975, MNRAS, 172, 557

Stawarz, Ł., & Ostrowski, M. 2002, ApJ, 578, 763

Stawarz, L., Aharonian, F., Wagner, S., & Ostrowski, M. 2006, MNRAS, 371, 1705

Stawarz, L., & Petrosian, V. 2008, ApJ, 681, 1725

Stawarz, L., Petrosian, V., & Blandford, R. D. 2010, ApJ, 710, 236

Stecker, F.W., Baring, M. G. & Summerlin, E. J. 2007, ApJL, 667, L29.

Stecker, F.W., & Glashow, S.L. 2001, Astropart. Phys. 16, 97

Stecker, F. W., & Scully, S. T. 2008, A&A, 478, L1

Sturrock, P. A. 1966, Physical Review, 141, 186

Syrovatskii, S. I. 1959, SvA, 3, 22

Tavecchio, F., & Ghisellini, G. 2008, MNRAS, 385, L98

Tavecchio, F., Ghisellini, G., Ghirlanda, G., Costamante, L., & Franceschini, A. 2009, MNRAS, 399, L59

Tavecchio, F., Maraschi, L., & Ghisellini, G. 1998, ApJ, 509, 608

Urry, C.M., & Padovani, P. 1995, PASP, 107, 803

Vannoni, G., Gabici, S., & Aharonian, F. A. 2009, A&A 497, 17V

Vlahakis, N., Königl, A. 2003, ApJ, 596, 1080

Webb, G. M., Drury L. O'C., Biermann, P. 1984, A&A, 137, 185

Yang, J., Wang, J., Dai, B., & Gao, X. 2009, PASJ, 61, 1153

Zacharopoulou, O., Khangulyan, D., Aharonian, F., & Costamante, L. 2011, ApJ in press

Zeldovich, Y., & Novikov, I. 1964, Sov. Phys. Dokl., 158, 811

Zirakashvili, V.N., & Aharonian, F. 2007, A&A, 465, 695

Zdziarski, A. A. 1989, ApJ, 342, 1108

Acknowledgements

First of all I would like to thank my supervisors, Dr. Frank Rieger and prof. Felix Aharonian, without whom this thesis would not be possible. I deeply thank Frank Rieger who has greatly motivated me for several astrophysical research themes, he has imparted to me his fascination and enthusiasm for astrophysics through many inspiring discussions, and he has introduced me to the art of scientific writing. His advising but also his kindness, support and patience have been invaluable. I am also extremely grateful to Felix Aharonian, the guidance of whom helped me to transform from an ignorant student to a young researcher. The critical sight into several research topics and the deep understanding of them are among the priceless things I learned from him. For sure, I could not hope for better supervisors. I would also like to sincerely thank prof. Stanislav Kelner who has kindly taught me analytical and mathematical technics. Learning from him has proven to be among the most valuable skills I obtained during these years. I would like also to thank prof. Werner Hofmann for his kindness to be the referee of this thesis and for his patience. I also thank prof. Matthias Bartelmann and prof. Eva Grebel for accepting to be my exam committee. I am indebted to Christian Fendt who accepted to be part of my thesis committee and has always offered his help, whenever I needed it.

I am very grateful to many people associated to the High Energy Astrophysics group in MPI-K, who helped me a lot with my research and made my everyday life in the institute so enjoyable. My sincere gratitude to Emma De Ona Wihelmi for her help and advices on the observational part and for being such a wonderful friend. My thanks also to Maxim Barkov for issues related to MHD, Valenti Bosch-Ramon and Mytia Khangulian for their help on radiation processes. I want also to very much thank Sabrina Casanova for her cheerfulness, Roland Crocker for the help with Mathematica, Victor Zabaltza for the interesting discussions, those who have left already, David Jones Andrew Taylor, but also Luigi Costamante for many nice discussions, and profs. Heinz Völk, John Kirk and Stefan Wagner, and of course my phd fellows, Ervin Kafexhiou for all the help with the computer, Anton Prosenkin and Ruizhi Yang for their support and all of them for the kikker fun.

I would like to deeply thank the wonderful friends in Heidelberg, that made my stay here an experience of life. Emma once again for everything, Vivi for being like a sister to me, my great flatmates Claudia, Paula, Romanski for all the fun and most important for all the sharing, Nikos for becoming such close friend, Marta for all the laugh, the British Toby, Adam and Matt for their wonderful company, Andy of course, Michael for many many things and Christian. I would also like to specially thank my close family, my mother Popi and my sister Ismini for their support and unconditional love that proved so important. And my step-father Marios, without whom I would not be what I am. And Tzesi for taking care of them. And I own a lot to my beloved friends back home, Tzo kirofaki, Pagio and Gaki, Hara, Evi, Niko Skivalo, Michali and Marianthi, George Pappas, Mitso, my cousin Giota and Giorgo

and my sweet Artemis, little Helen and all my big family; all of them supported in their own special way this phd. I also want to deeply thank my Alex for his love, which has been a home to me. Last, I own a gratitude to my first teacher, Manolis Kapetanakis, who motivated and supported me so much for studying physics.

This thesis is dedicated to my father, Chris, and to my step-father, Marios, who taught me the most important of all; life.

List of publications

Refereed Journals

1. Lefa, E., Rieger, F. M., & Aharonian, F. 2011, ApJ, 740, 64
"Formation of Very Hard Gamma-Ray Spectra of Blazars in Leptonic Models"

2. Lefa, E., Aharonian, F. A., & Rieger, F. M. 2011, ApJL, 743, L19
"Leading Blob Model in a Stochastic Acceleration Scenario: The Case of the 2009 Flare of Mkn 501"

3. Lefa, E., Kelner, S. R., & Aharonian, F. A. 2012, ApJ, 753, 176
"On the Spectral Shape of Radiation due to Inverse Compton Scattering Close to the Maximum Cutoff"

Conference proceedings

1. Lefa, E., Rieger, F. M., & Aharonian, F. 2010,
25th Texas Symposium on Relativistic Astrophysics,
"The formation of hard TeV gamma-ray spectra in Blazars" (poster)

2. Lefa, E., Rieger, F., & Aharonian, F. 2011,
AGN Physics in the CTA Era (AGN 2011),
"Hard VHE γ-ray spectra in Blazars" (talk)

3. Lefa, E., Rieger, F. M., & Aharonian, F. A. 2012,
International Journal of Modern Physics Conference Series, 8, 31 "Hard Gamma-Ray Source Spectra in TeV Blazars" (talk)